UNIVERSITÀ DEGLI STUDI DI PADOVA

DIPARTIMENTO DI INGEGNERIA CIVILE, EDILE E AMBIENTALE

Department Of Civil, Environmental and Architectural Engineering

Master's Degree in Environmental Engineering

MASTER THESIS

3D geomechanical modelling of sinkholes formation: investigating geomechanical consequences associated with mining areas in the Silesian Coal Basin, Poland

Supervisor:
Prof. Eng. PIETRO TEATINI
Co-supervisors:
Dr. ANDREA FRANCESCHINI
Dr. ARTUR GUZY

Candidate: RICCARDO MARTELLO
2061726

ACADEMIC YEAR 2023/2024

ABSTRACT

This Master's thesis aims to investigate the occurrence of sinkholes, which are unpredictable geological phenomena posing a significant danger worldwide. Historically, hard coal has been a primary source of energy production. However, with the ongoing energy transition toward more sustainable and renewable resources, mining activities are gradually ceasing. In Poland, hard coal extraction has been practiced for centuries, resulting in growing concerns for local authorities due to the identification of numerous sinkholes above coal mines.

Land subsidence following hard coal mining is caused by several processes. First, groundwater lowering since mining activities must be carried out in dry conditions. Second, the extraction of hard coal from underground deposits, causing an unbalance distribution of the geostatic load. Despite efforts to backfill working areas after mining closure, voids often persist, contributing to land subsidence and potentially leading to sinkhole formation. Additionally, a third factor exacerbates this phenomenon: the natural groundwater rebound following the end of pumping activities, resulting in water entrance into the mine and the subsequent rewetting of dry soils, which weakens them further. Therefore, it is crucial to conduct geomechanical simulations to understand the soil response to the variations caused by these factors.

This thesis aims at evaluating, through 3D geomechanical modelling, the land subsidence caused by the second factor, i.e. the removal of hard coal at depth, with an estimate of the consequences associated to the lowering of groundwater level. The research is conducted in the "Siersza" coal mine in the Upper Silesian Coal Basin, Poland. The model implementation has been carried out with GEPS3D, a three-dimensional continuous/discontinuous geomechanical simulator developed by the Numerical Analysis group of the ICEA Department at the University of Padova.

Initially, hydrogeological and geomechanical data provided by the Polish Geological Institute were processed under the supervision of AGH University of Krakow. This dataset was then utilized to create a 3D mesh representing the Siersza mine. This mesh served as an input for GEPS3D to compute land subsidence resulting from mining operations. The simulations employed a continuous mechanics approach, lacking the capability to reproduce the discontinuous processes associated with sinkhole formation. Additionally, a one-dimensional approach was used to estimate land subsidence resulting from the significant lowering of the water table necessary for mines development. Measurements conducted by the Polish mining authority facilitated model calibration. Furthermore, the results of the numerical model were compared with those obtained from the Knothe-Budryk analytical model, commonly used in Poland to quantify land subsidence induced by mining activities. Following proper

adjustment of soil stiffness parameters, a maximum subsidence of approximately 0.04 m was obtained.

This work represents an initial step towards enhancing our understanding of both continuous and discontinuous soil deformations resulting from shallow mining activities. By shedding light on this phenomenon, it lays the groundwork for developing future strategies aimed at risk management to mitigate sinkhole formation and to provide useful information to land-use planning activities in regions impacted by hard coal mining extraction.

TABLE OF CONTENTS

List of Figures

List of Tables

Chapter 1

Introduction

This thesis aims to improve our understanding of continuous (i.e., land subsidence) and discontinuous processes (i.e. sinkholes), associated to coal mining. These geological phenomena are unfortunately notorious worldwide (Gongyu & Wanfang, 1999; Soldo et al., 2020; Tihansky, 1999; Witkowski et al., 2024). Awareness of this kind of hazard is crucial for the development of monitoring, mitigation, and remediation strategies. The environmental consequences related to the exploitation of non-renewable energy resources are widely recognized globally. Indeed, recent decades have been marked, from both energy and environmental perspective, by the implementation of various treaties, among which the Paris Agreement and the Tokyo Protocol, aimed at compelling state parties to reduce greenhouse gases emissions (GHGs) to prevent the rise of global temperature. Consequently, European countries such as Germany, The Netherland, Italy, and Poland have had to adhere to these regulations by limiting and occasionally halting activities involving the exploitation of non-renewable resources. However, despite the numerous positive impacts of the energy transition, the reduction or cessation of polluting activities also brings about negative counter-effects. For instance, following the closure of hard coal mines in the Upper Silesian Coal Basin in Poland, the occurrence of sinkholes has become evident, prompting researchers to investigate potential cause-effect relationships. Since then, Polish academic scholars have expanded their studies to investigate similar events worldwide (Gongyu & Wanfang, 1999; Singh & Dhar, 1997), focusing on three major topics: the detection and monitoring of sinkholes precursors (Kim et al., 2021; A. A. Malinowska et al., 2019), analytical modelling of continuous land deformation using the Knothe-Budryk method, (Guzy & Witkowski, 2021; A. Malinowska et al., 2020), and the analysis of the water rebound in abandoned mines (Banks et al., 2010; Witkowski et al., 2024).

With the present thesis, a fourth topic has been considered, consisting in the simulation by numerical modelling of the soil response to hard coal removal at shallow depth. This process plays a major role in sinkholes occurrence. The use of a proper geomechanical model based on the Finite Element method allows to solve partial differential equations governing the soil equilibrium in a three-dimensional setting. The simulator used in this modelling study has

already been applied in other researches related to land subsidence (Bonì et al., 2020; Gambolati et al., 1986; Ochoa-González et al., 2018; Teatini et al., 2011; Ye et al., 2018; Zhu et al., 2020). In this thesis, the GEPS3D geomechanical simulator was applied do investigate the displacement and stress fields caused by the development of the hard coal mine "Siersza", located under the Trzebinia locality, in southern Poland. This is an urbanized area where thousands of people live and where railway lines and roads of regional importance converge. An in-depth analysis of hydrogeological and geomechanical data from the Polish Geological Institute was initially carried out. During this phase, several boreholes were investigated, in order to collect their coordinates, depths, and stratigraphy. Subsequently, it was possible to process these data to build-up, initially, a two-dimensional mesh, and, with further data manipulation, the final three-dimensional mesh incorporating the mine geometry and the geological setting. Then, the calculation of geological stresses and nodal forces was implemented and applied on the nodes representing the top and the bottom of the hard coal panels removed from the subsurface. At last, the computation of land subsidence and the model calibration were carried out.

The thesis structure is the following. In Chapter 2, a general overview about sinkholes is provided. Here, the main causing factors, the monitoring, mitigation, and remediation procedures are investigated. Moreover, a global perspective of sinkholes occurrence is given. In Chapter 3, a description of history and energy framing in the Silesia region is presented, while the main geographical and geological information about the case study area are introduced in Chapter 4. Then, Chapter 5 provides an overview of the geomechanical simulator used in the study, exploring the equations that govern the geomechanical problem. Then, Chapter 6 describes the model set-up, with a brief discussion on input data, whereas Chapter 7 reports the modelling results. Finally, a conclusion section summarises the main outcomes of this research work and drafts future prospects for similar scientific applications.

Chapter 2

Overview of sinkholes phenomena

Sinkholes are significant and often unpredictable geological phenomena, manifesting as soil depressions, subsidence, or voids. They can arise naturally or be triggered by various human activities such as construction, water drainage, or mining.

The Glossary of Geology defines a sinkhole as *"a circular depression in a karstic area, characterized by underground drainage and dimensions ranging from meters to tens of meters, typically assuming a funnel shape"* (Bates & Jackson, 1987). Despite the apparent simplicity of this definition, sinkholes can be further classified based on their collapse processes, occurrence velocities, and formation mechanisms.

2.1 Mechanism of sinkholes formation

There are two primary types of sinkhole formation mechanisms: naturally induced and man-made induced.

Naturally occurring sinkholes typically form through a uniform mechanism, predominantly in karstic environments, which are widespread globally. This mechanism involves the continuous dissolution of soluble rocks, such as limestone and gypsum, by groundwater flow, as stated by Ferentinou et al. (2020). The chemical dissolution process in these rocks is described by the following chemical reactions (Kaufmann et al., 2016):

For limestone:

$$CaCO_3 + CO_2 + H_2O \leftrightarrow Ca^{2+} + 2HCO_3^- \tag{2.1}$$

For gypsum:

$$\mathrm{CaSO_4 \cdot 2H_2O} \leftrightarrow \mathrm{Ca^{2+}} + \mathrm{SO_4^{2-}} + \mathrm{2H_2O} \tag{2.2}$$

Central to these reactions is the formation of carbonic acid (H_2CO_3), resulting from the dissolution of carbon dioxide in rainwater, a process occurring both in the atmosphere and the soil (Equation 2.3):

$$H_2O + CO_2 \rightarrow H_2CO_3 \tag{2.3}$$

Carbonic acid plays a substantial role in dissolving calcium carbonate ($CaCO_3$), the primary component of carbonate rocks. However, the composition of rocks is not the only factor in sinkhole formation. Intrieri et al. (2015) identify the dissolution process as a primary factor, followed by existing man-made underground cavities, poor geomechanical properties of bedrock, and acidic groundwater circulation, which intensifies rock erosion. For these phenomena to occur, certain triggers are necessary, such as earthquakes, anthropogenic vibrations, or changes in the hydraulic gradient. Typically, sinkholes begin forming in the lower stratum where a cavity is created, gradually advancing towards the surface.

Man-made induced sinkholes can form in various contexts, including urban development, groundwater drainage, and mining operations. Notable examples include sinkholes in urban areas resulting from water main breaks or sewer collapses, which can lead to sudden ground subsidence. Additionally, the overextraction of groundwater for agriculture or industry can lead to the formation of sinkholes, as the depletion of groundwater causes underground voids to collapse and trigger mechanical and chemical suffusion.

However, this thesis specifically focuses on sinkholes induced by mining activities, primarily resulting from the collapse of underground mine voids. Furthermore, changes in the groundwater head during mining exploitation, namely groundwater decline during the active state of mining and groundwater rebound associated with mine closure, may further contribute to the weakening of rock layer structures and the formation of sinkholes. These occurrences can be attributed to several factors:

- Shallow depth: The depth of mining operations is a critical factor influencing the occurrence of sinkholes. Several studies in different coal fields worldwide have shown that sinkhole formation is more likely when the depth of workings varies between approximately 25 m and 100 m in (Table 2.1). A key indicator is the overburden thickness to mining height ratio (h/m). Sinkholes are highly probable when the h/m ratio is below 6, with the likelihood decreasing significantly as the ratio ranges between 5

and 11. Singh and Dhar (1997) reported that 90% of sinkholes occurred when the h/m ratio was less than 6.

- Weak overburden: The stability of an underground excavation is dependent on the stress balance and the strength of the roof rock. Once the underground opening is made, the strata immediately above the opening become de-stressed. The opening will remain stable as long as the stresses do not exceed the strength of the roof rock. Over time, changes in stress and strength, often due to groundwater inflow and creep deformations, can compromise roof stability. Moreover, fluctuations in groundwater levels affect the effective stresses by altering hydraulic head and pore pressure within the rock mass.
- Geological discontinuities: The presence of closely spaced joints and faults is a significant factor in the formation of sinkholes, as these discontinuities can weaken the structural integrity of the overburden and facilitate collapse.
- Rainfall: Seasonal recharge of the overburden during rainy periods can increase pore pressure, potentially triggering roof falls. This correlation is supported by observations in the Chikuho district, Japan, where the frequency of sinkholes was found to increase substantially during the rainy period (Esaki et al. 1989).

Table 1 Mining depth for sinkhole subsidence cases. Source: Singh & Dhar (1997)

Sl. No.	Location	Reference	Maximum depth (m)
1	Western Pennsylvania	Gray *et al.* (1978)	47.7
2	Hanna Area, Wyoming	Berg (1980)	73.2
3	Sheridan Area, Wyoming	Dunrud and Osterwald (1980)	77.0
4	Beulan Area, North Dakota	Dunrod and Osterwald (1980)	24.4
5	Illinois Coal Basin	Hunt (1980)	50.3
6	St David Area, Illinois	Wildanger *et al.* (1980)	50.3
7	Colorado Springs Area	Matheson and Pearson (1985)	45.7
8	Superior, Wyoming	Brown (1986)	30.5
9	Rock Springs, Wyoming	Colaizzi (1986)	101.5
10	Glenrock, Wyoming	Gormley (1986)	30.5
11	Handidhua and Deulbera mines	Singh (1986)	40.0
12	Humberside & Lincolnshire	Whittaker and Reddish (1989)	90.0
13	Mithapur Colliery, India	Anon. (1994)	25.0
14	Jamuna and Kotma Area, India	Singh and Dhar (1996)	43.0

2.2 Types of sinkholes

Understanding the diverse types of sinkholes is crucial for geologists and engineers. Waltham et al. (2005) offer one of the most comprehensive classifications, categorizing sinkholes into six types: Solution, Collapse, Caprock, Dropout, Suffosion, and Buried. However, given current

climate changes and their correlation with sinkhole formation, one can consider the expansion of this classification to include climate-change-related sinkholes. This addition would reflect the evolving nature of sinkhole formation influenced by extreme weather events, altered precipitation patterns, and other climate change impacts, thereby providing a more holistic understanding of the phenomenon.

To define solution sinkholes, the United States Geological Survey (USGS) provides a useful description: *"a ground area lacking natural external surface drainage, allowing rainwater to be drained solely through the subsurface"* (What Is a Sinkhole? | U.S. Geological Survey). This type of sinkhole occurs when rainwater directly contacts exposed rock surfaces such as limestone, dolomites, and gypsum (Figure 2.1). The resulting chemical dissolution process can lead to the formation of ponding water and wetlands. Since the formation of solution sinkholes is an extremely slow process, they generally do not pose significant concerns for anthropogenic environments.

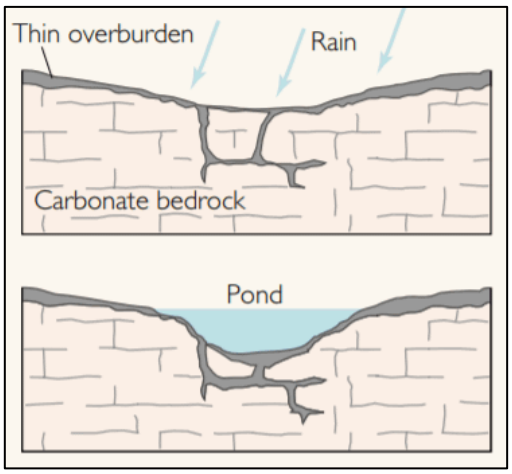

Figure 2.1 Dissolution sinkhole.
Source: (Sinkholes | U.S. Geological Survey)

Dropout and suffusion sinkholes (Waltham et al., 2005) develop gradually, often in areas where the ground layer is predominantly sandy (Figure 2.2). Due to their small size, they can remain undetected for extended periods. The formation of these sinkholes occurs in four distinct stages (Sinkholes | U.S. Geological Survey):

1. Formation of fractures in underlying bedrock:
   The initial stage involves the development of fractures in the underlying bedrock. These fractures set the foundation for subsequent processes.

2. Sediments filling the fractures (piping process):
   Following the formation of fractures, sediments begin to fill these openings through a process known as 'piping.' This stage is marked by a gradual buildup within the subsurface, setting the stage for further developments.
3. Continued dissolution forming a larger depression:
   The dissolution process persists, leading to the enlargement of the depression. This stage sees ongoing chemical reactions with the bedrock, further altering the subsurface structure.
4. Formation of small surface depressions due to erosion:
   In the final stage, surface erosion leads to the creation of small depressions on the surface, contributing to the overall subsidence of the terrain.

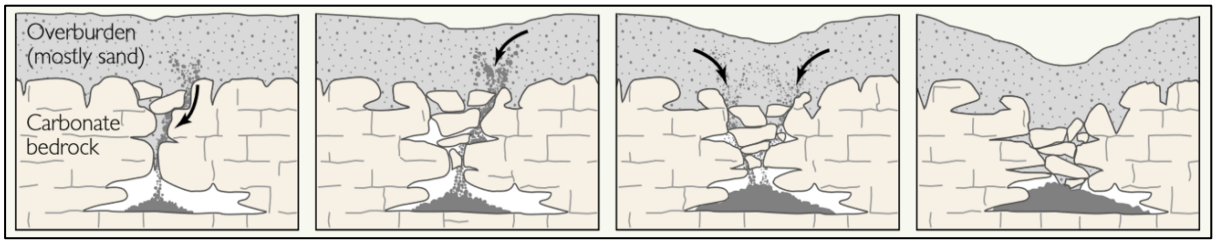

Figure 2.2 Cover-subsidence sinkhole. Source: (Sinkholes | U.S. Geological Survey)

The study of collapse and caprock sinkholes reveals a closely interconnected formation process. Both types involve the fracturing, breakdown, and eventual collapse of unsupported bedrock structures such as slabs, beams, and arches, as described by (Waltham et al., 2005). These phenomena typically occur in soil sediments containing a significant amount of clay (Figure 2.3). Over time, a process called “spalling” occurs, where sediments gradually peel away in the underlying rock fractures. This continuous spalling, combined with the resilient nature of clay, results in the formation of arch-like structures within the soil. When these arches reach a critical thickness, they collapse, creating a cavern below (Sinkholes | U.S. Geological Survey).

The distinction between collapse and caprock sinkholes lies in the composition of the soil overlying the cavity. In caprock sinkholes, this soil is made of insoluble rocks, varying in thickness from a few meters to several tens of meters. When collapse occurs, a distinctive circular hole rapidly forms in the terrain, evolving quickly from minutes to hours until it reaches its final shape. While the sinkhole

stabilizes at this stage, the surrounding sediments continue to settle, a process that may take around a day to complete. Rainfall significantly influences this stabilization period, as it can prolong the overall duration of the settling process. In some cases, the stabilization and settling process can extend over years, highlighting the dynamic nature of these geological formations.

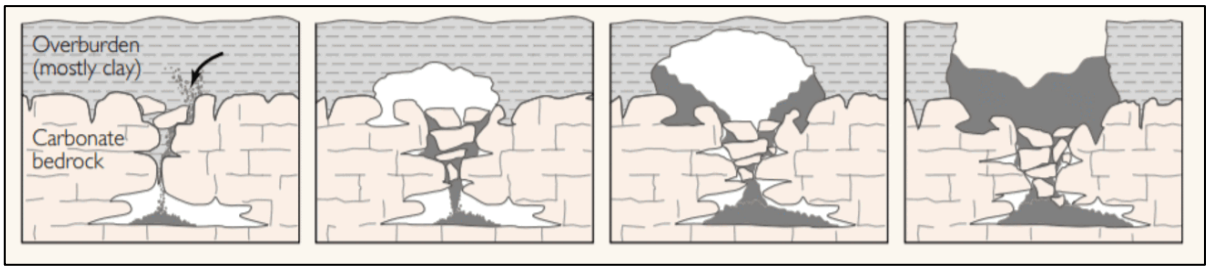

Figure 2.3 Cover-collapse sinkhole. Source: (Sinkholes | U.S. Geological Survey)

In a karstic environment, any depression, regardless of its size, shape, or morphology, and whether it is fully or partially filled, buried or exposed at the surface, falls under the classification of a buried sinkhole. Many of these formations start as solution sinkholes, and, over time, become filled due to sedimentation driven by climatic or environmental changes. The presence of buried sinkholes poses a significant geohazard in engineering. This is due to the risk of the filling material being lost through suffusion into underlying voids, which can lead to the development of new subsidence sinkholes, as noted by (Waltham et al., 2005).

The most critical geohazard in this context is represented by human-induced sinkholes. These sinkholes are directly related to various anthropogenic activities that alter the landscape, such as: drilling, water pumping, excessive irrigation, and mining. Unlike natural sinkholes, human-induced ones have substantial impacts on the environment. They lead to challenges like destabilizing the earth, causing soil erosion, and altering hydrogeological and local topographical features.

A specific concern in mining operations is mine subsidence, which is a significant cause of human-induced sinkholes. In general, mining-induced sinkholes can be defined as in the Article XXXVIIIA of the Illinois Insurance Code: "*lateral or vertical ground movement caused by a failure initiated at the mine level, of man-made underground mines, including, but not limited to coal mines, clay mines, limestone mines, and fluorspar mines that directly damages residences or commercial buildings"* (What Is Mine Subsidence? - About Mine Subsidence - Illinois Mine Subsidence Insurance Fund). During mining, materials are extracted from underground deposits, typically through galleries or underground cavities. This process

involves excavating the mine in a grid pattern, leaving pillars of unmined material to support the overhead space, as illustrated in figure 2.4. However, these pillars may eventually collapse due to pressures and tensions caused by the removal of material underneath, leading to the formation of sinkholes.

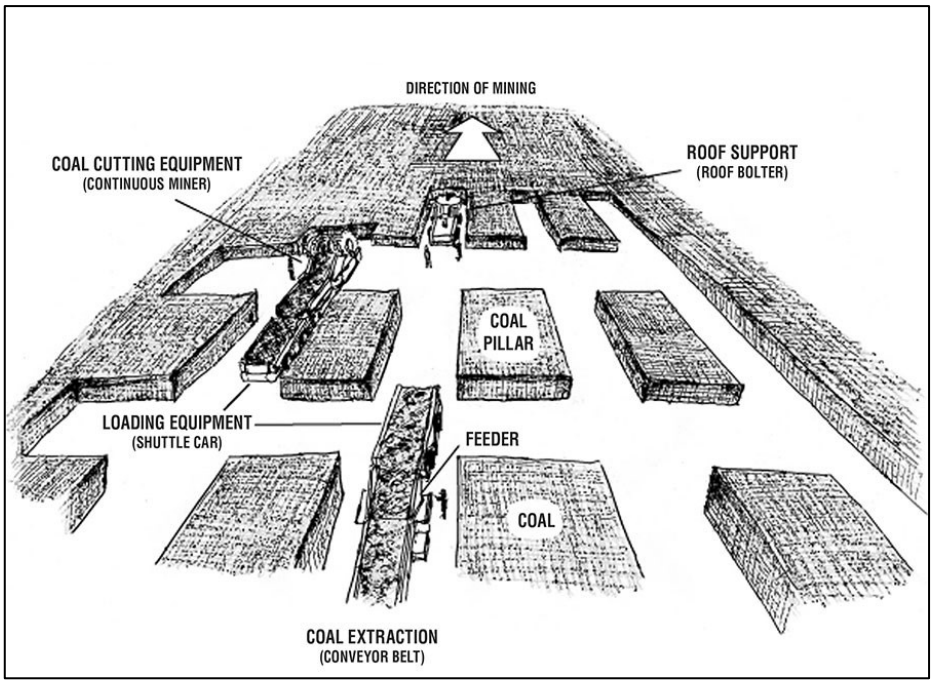

Figure 2.4 Mine grid pattern. Source: (What Is Mine Subsidence? - About Mine Subsidence - Illinois Mine Subsidence Insurance Fund)

In the last decades, several studies have assessed the pivot role of climate changing in the formation of sinkholes (Delle Rose, 2022; Linares et al., 2017; Panno et al., 2012). The most relevant climate factor is the worldwide temperature increase. Indeed, this can lead to periods of drought mixed with heavy precipitations, involving changes in the groundwater system, thus enhancing ground instability. Moreover, higher temperatures entail the thaw of ice in the arctic regions, releasing methane in the atmosphere. Hence, this gas increases the greenhouse effect, by effect of which the global temperature will rise again, creating a climate-changing loop.

2.3 Sinkholes: a worldwide perspective

Sinkholes are widespread geological phenomena that have a significant impact on people around the world. The specific types and mechanism of formation, as described in Section 2.2., vary across different regions, influenced by the terrain, regional hydrology and land use practices.

Scientific interest in sinkholes has grown exponentially since the 1980s, as illustrated in Figure 2.5. Furthermore, the enormous variety of countries contributing to scientific articles (Figure 2.6) highlights the presence of these phenomenon all over the world.

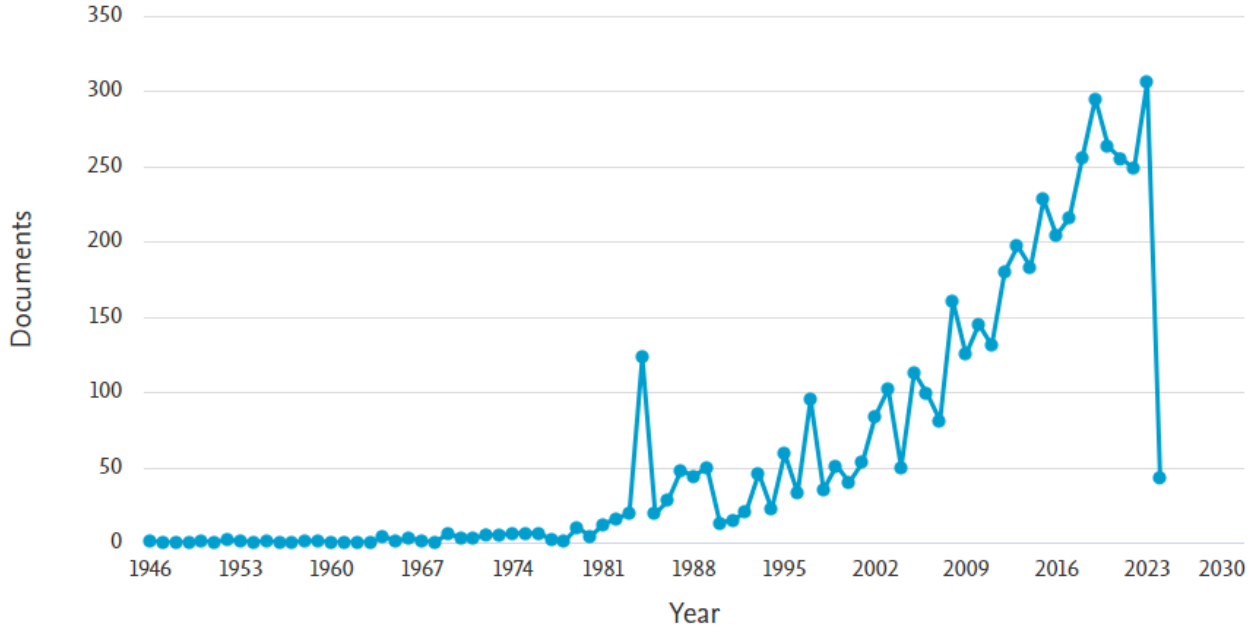

Figure 2.5 A bibliometric analysis of sinkhole-related research highlights the increased interest in the physical phenomenon of sinkholes. Source: (Scopus)

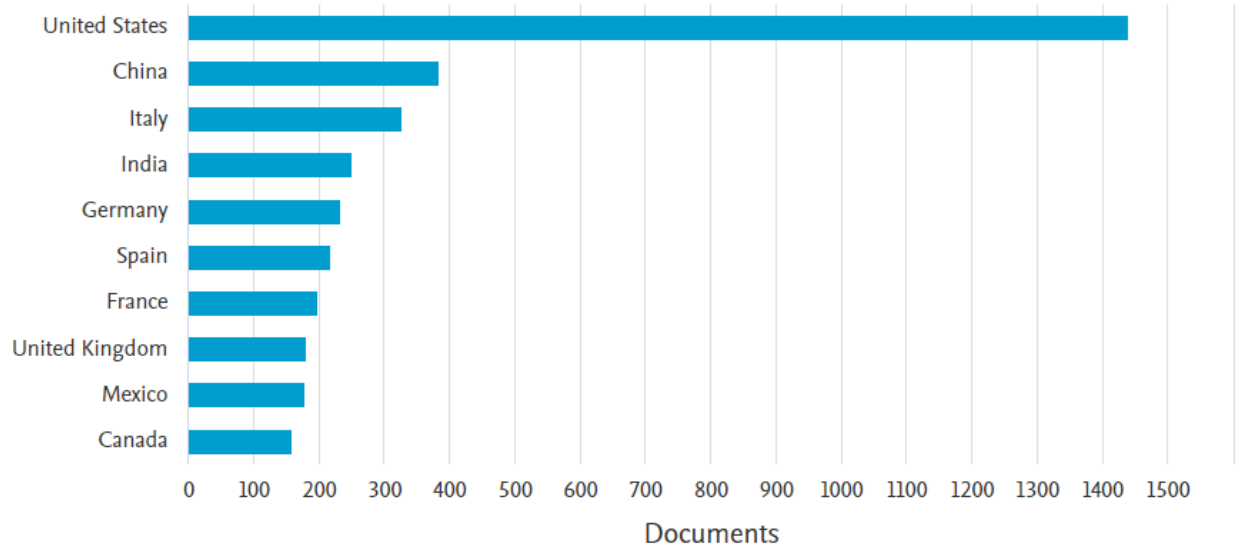

Figure 2.6 A bibliometric analysis of sinkhole-related research highlights the global interest in the physical phenomenon of sinkholes. Source: (Scopus)

In this thesis, a selection of sinkhole examples will be analysed to illustrate this diversity: two naturally occurring solution sinkholes from Florida and South Africa, a man-made sinkhole in Guatemala resulting from urban infrastructure collapse, sinkholes in Canada and Russia that are emerging due to climate change effects and sinkholes in Poland related to mining activity. These examples will demonstrate the broad range of sinkhole causes and characteristics, reflecting their global prevalence and the varying factors that contribute to their development.

2.3.1 Florida

Florida's environment is characterised by a vast carbonate platform, a part of a much larger geological structure (Figure 2.7). The state's warm, humid climate, combined with regular rainfall and occasional hurricanes, facilitates the action of rainwater on underlying soluble rocks, making it highly susceptible to cover-collapse and cover-subsidence sinkholes (Devin et al., 1999).

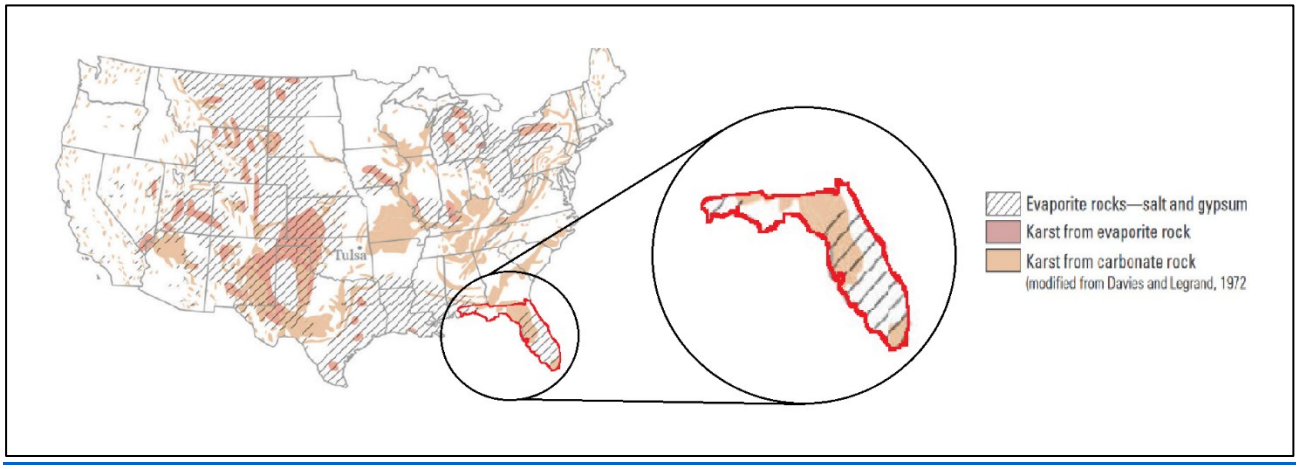

Figure 2.7 U.S. map, Florida's highlighted. Source: (Sinkholes | U.S. Geological Survey)

One notable instance is the largest sinkhole ever registered in Florida, formed in May 1981. Measuring circa 106.7 m in width and 22.8 m in depth, it was large enough to swallow an Olympic-sized pool and two streets (Florida's Most Famous Sinkhole | Sinkholes | The Guardian). This event underscores the significant impact of sinkholes in the region.

Over the past decades, numerous extensive studies have been conducted to enhance the comprehension of the processes driving sinkhole formation (Brinkmann et al., 2008), (Talib et al., 2022).

(Atkinson, 1977) conducted a study on the hydrology of limestone terrain in the Mendip Hills of Great Britain, which provided insights into the mechanisms of diffuse and conduit flow in

karst landscapes. This research has been instrumental in understanding the hydrogeology of west-central Florida, which shares similar geological features.

Moreover, (Tihansky, 1999) highlights the significant influence of groundwater pumping on sinkhole formation in Florida. In the early 1930s, widespread pumping along the west coast of Florida caused a decline in hydraulic head in freshwater aquifers and the upconing of saline water. This led to pumping activities shifting inland, north of Tampa city, and the development of four pumping fields: Cosme, Eldridge-Wilde, Section 21, and South Pasco (Figure 2.8). Sinkholes began appearing immediately after the initiation of pumping. Figure 2.9 portrays the behaviour of the Section 21 field, which, after starting in 1963, saw a near tripling of its pumping rate within a year. This led to a groundwater level drop of more than 10 feet (approximately 3 m) and the formation of 64 sinkholes in a single month.

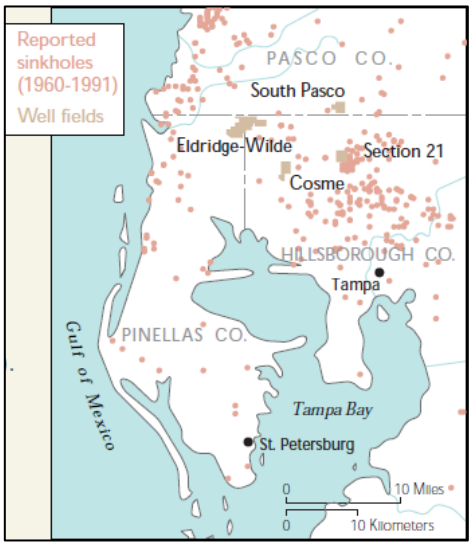

Figure 2.8 Cosme, Eldridge-Wilde, Section 21, South Pasco pumping wells. Source (Tihansky, 1999)

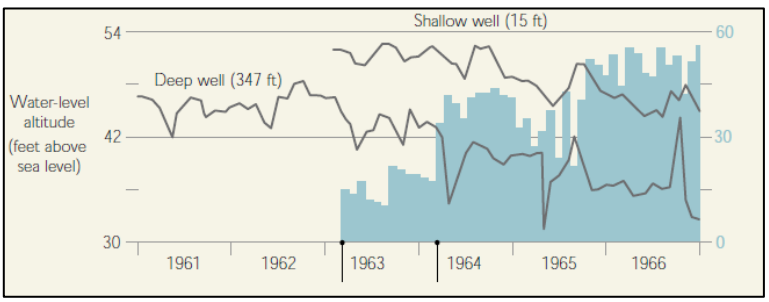

Figure 2.9 The effects of pumping on sinkhole development near the Section 21 well field. Source: (Tihansky, 1999)

Agriculture, a vital economic activity in Florida, also contributes to sinkhole formation. To prevent freeze damage to crops during winter, farmers irrigate fields with warm water. Extended freezing periods necessitate prolonged water withdrawal, leading to an increase in sinkholes, as shown in Figure 2.10 (Tihansky, 1999).

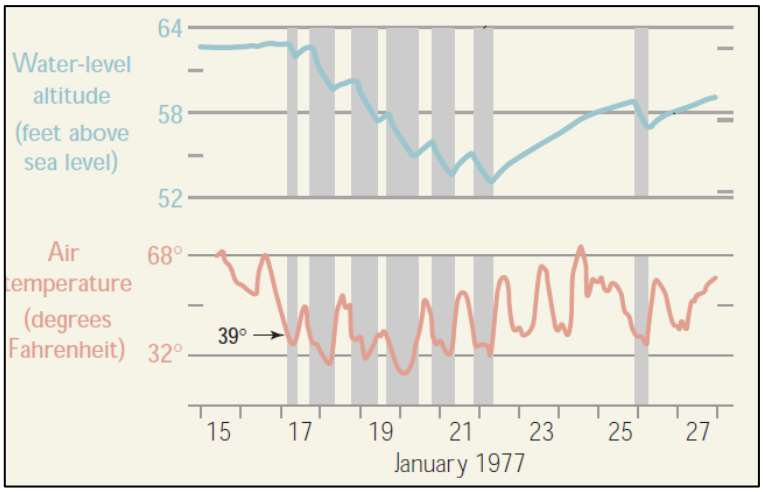

Figure 2.10 The relationship between sinkholes formation, and groundwater level. The thickness of the grey columns indicates how many sinkholes complains were raised by the citizens. Source:(Tihansky, 1999)

2.3.2 South Africa

In South Africa, particularly in the Gauteng province (Figure 2.11), the geology is primarily characterized by carbonate rocks. These rocks have undergone complex geomorphological transformations over almost 3 billion years. This includes three periods of karstification after deposition and before the current cycle of karst development. The region's geological history is marked by prolonged weathering, erosion, and various continental uplifts, contributing to the unique karst landscape we observe today (Oosthuizen & Heath, 2008).

Figure 2.11 South Africa geological frame, Gauteng province. Source: (Wikipedia, Gauteng)

The geological landscape is further affected by the negative impacts of anthropogenic activities. These activities, which are becoming progressively more intense and deeper underground, include leakage from water pipes and sewage systems, as well as extensive groundwater extraction. Over time, these conditions have led to increased water infiltration, creating ideal conditions for the formation of sinkholes (Buttrick & Van Schalkwyk, 1998).

A striking example of the consequences can be seen in the Far West Rand region, where sinkholes caused by extensive dewatering have led to 38 deaths. In the municipality of Tshwane, the situation is particularly alarming. Here, more than 40 million litres of drinking water are extracted daily from the dolomite aquifer, as reported by (Ferentinou et al., 2020). This excessive extraction has not only heightened the risk of sinkholes (Figure 2.12) but also led to significant water resource challenges.

To mitigate these risks, extensive and costly measures have been undertaken. In a notable effort, about 30,000 households were relocated from a vulnerable dolomite area west of Johannesburg. This massive relocation effort, necessitated by the threat of sinkholes, cost over USD 600 million. Such measures underscore the severity of the sinkhole problem in South Africa and the significant economic and social impacts they can have.

Figure 2.12 Sinkholes in Eeufeed Roas area, Tshwane. Source: (Oosthuizen & Heath, 2008)

2.3.3 Guatemala

Guatemala, located in Central America, is in a region with active seismic activity, including the presence of active volcanoes, transform faults and extensive karst topography. These geological characteristics result from a complex history of subduction, plate collisions and, more generally, the evolution of plate tectonics in the Caribbean region (Field Guide to Guatemalan Geology: Stanford Alpine Project).

In 2005, residents of Guatemala City began to express concerns about noise and tremors in their homes. Unfortunately, these early warnings were not taken seriously until two sinkholes appeared. In 2007, a massive sinkhole measuring 30 m in width and 60 m in deep (Figure 2.13), swallowing five houses and leading to three fatalities. Despite extensive investigations by authorities and scientists from various disciplines, the precise cause of this collapse remained elusive.

Figure 2.13 Sinkhole that occurred in zone 6. Source: (Hermosilla, 2012)

The community faced a similar crisis in May 2010 when another sinkhole emerged in Zone 2 (Figure 2.14). After thorough studies, the collapse mechanism was identified: the city's inadequately designed sewage system. Originally planned to have two separate lines with substantial diameters for different city sections, economic constraints led to significantly smaller pipes being installed. The Atlantic section's pipe was reduced to a diameter of 4.5 m, and the Pacific section's pipe to 3.75 m, with both narrowing further to just 0.25 m at their ends. This flawed design eventually led to the collapse of the sewer system and the formation of the sinkhole.

Figure 2.14 Lateral view of sinkhole in zone 2. Source: (Guatemala City Hit by Second Sinkhole | New Civil Engineer)

In response, authorities undertook remediation actions, filling the sinkholes with “mudcrete”, a mixture of cement, limestone, and water (Hermosilla, 2012). This approach aimed to stabilize the ground and prevent further collapses, highlighting the critical need for effective urban planning and infrastructure maintenance in areas prone to geological hazards (Hermosilla, 2012).

2.3.4 Arctic regions

Sinkholes in the Arctic region illustrate the direct impact of climate change on geological phenomena. In 2014, an enormous sinkhole, measuring 45 m in depth, appeared on the Yamal Peninsula in Siberia (Figure 2.15), baffling scientists with its size and formation mechanism. Initial investigations revealed unique characteristics: the sinkhole's rim was elevated above the surrounding ground level, suggesting an explosive force from below rather than a traditional inward collapse. Debris from the earth was found scattered hundreds of meters away, indicating the intensity of the explosion. Subsequent research linked this explosion to high concentrations of methane gas in the subsurface. Eight more sinkholes were discovered in or near the same region, raising concerns about these particular events. The year of 2014 was exceptionally warm in Siberia, with temperatures reaching 46 degrees above average in the city of Khatanga (Freedman & Khurshudyan, 2020). This trend of rising temperatures has been consistent over the years.

At the same time, in Kotzebue, on the opposite side of Siberia, a separate research team discovered a lake emitting over 10 million tonnes of methane daily. Methane is not the only common factor between these phenomena; both are found on the same frozen ground: permafrost.

Permafrost, defined as soil that remains at or below 0°C for at least two years (Osterkamp & Burn, 2003), can stay frozen for millennia. It contains a significant amount of organic matter, which, when thawed due to climate change, restarts the carbon cycle and releases methane. Further investigations on Lake Kotzebue revealed that the methane originated from a reservoir millions of years ago. This gas rose through the permafrost layer via seismic faults, a characteristic of the Siberian region, and once the permafrost began to thaw, the methane reached the surface of the lake.

Scientists estimate that over 1.3 trillion tonnes of methane are stored beneath the Arctic region, a quantity 250 times greater than the total methane content in the Earth's atmosphere. The release of this methane due to permafrost thawing not only contributes to sinkhole formation but also poses broader environmental challenges, as highlighted in the documentary (Arctic Sinkholes I Full Documentary I NOVA I PBS - YouTube).

Figure 2.15 Sinkhole in Yamal peninsula. Source: (Scientists Climb to Bottom of Siberian Sinkhole - in Pictures | World News | The Guardian)

2.3.5 Poland

Sinkholes are among the types of geological hazards present in Poland, causing damage to infrastructure as well as agricultural and forestry economies. They contribute to significant degradation of affected areas and pose a threat to people and their property.

The history of Poland is marked by centuries of hard coal exploitation. This country, along with the Czech Republic, is home to the Upper Silesian Coal Basin (USCB), the largest hard coal basin in the EU (Witkowski et al., 2023). For over a century, intensive mining activities in this area have led to irreversible changes to the Earth's surface, including phenomena such as subsidence and sinkholes, as highlighted by (Przyłucka et al., 2022). Currently, with the energy transition underway, some mines are being closed. The closure of these mines is observed to be accompanied by a rise in groundwater heads, which contributes to the reactivation of old mine workings and the formation of sinkholes.

Sinkholes in the USCB area have been present in the past, before World War II, and in the 1950s and 60s. Damage to buildings and environmental changes due to mining exploitation have only intensified over time. Among the most troublesome effects are changes in water conditions, subsidence troughs, secondary faults, pits, and sinkholes. This is because rocks forming the roofs of old workings, which lack plastic properties (such as sandstone), crack and fill the void below. More pliable rocks (such as shale) bend and crack. The sands and other loose deposits above them settle and move laterally, causing surface stability loss.

Buildings and other structures are quite resistant to compression, but ground extension mainly causes damage to walls and roads. In contrast, in areas without significant lateral stress (compression and extension), there is a risk of sinkholes caused by flooding. Mines in the USCB region have been battling water inflows from the beginning and had to drain the workings. During operation, this led to the formation of a depression cone and the drying up of some watercourses. For decades, the areas were regularly drained, but after the mine closure, the water level gradually returns to its original level. The result of groundwater activity flowing into abandoned workings is the drainage of the rock mass and suffosion sinkholes (often accompanying shallowly located workings, into which sands from the surface are mechanically washed).

Reports of sudden sinkhole formations in the Polish USCB region began in early 2021, in the area of former "Siersza" underground hard coal exploitation, close to the city of Trzebinia. By the end of 2023, 32 sinkholes had formed, with the largest measuring approximately 20 m in diameter and 10 m deep. Some sinkholes formed in urbanized areas, including a cemetery and a football field, posing a direct threat to the inhabitants. Figure 2.16 shows the impact of decades

of mining activities: a sinkhole formed in the middle of a football field in the city of Trzebinia. In general, the risk of sinkholes exists in areas where hard coal mining was conducted within a depth zone of 0-100 m below the ground level. The Polish Geological Institute has identified 500 sites in the Trzebinia region that are at risk of sinkhole occurrence (Residents Assured of State Support as Sinkhole Threat Looms in Trzebinia - PolandDaily24.Com) (Figure 2.17).
As this region and man-made induced sinkholes are the subjects of this thesis, a more detailed description of the area is provided in Section 4.

Figure 2.16 Sinkhole appeared in a football field, Trzebinia. Source: (Sinkholes in Trzebinia. There Are Test Results of the SRK Recovery Plan and Plan)

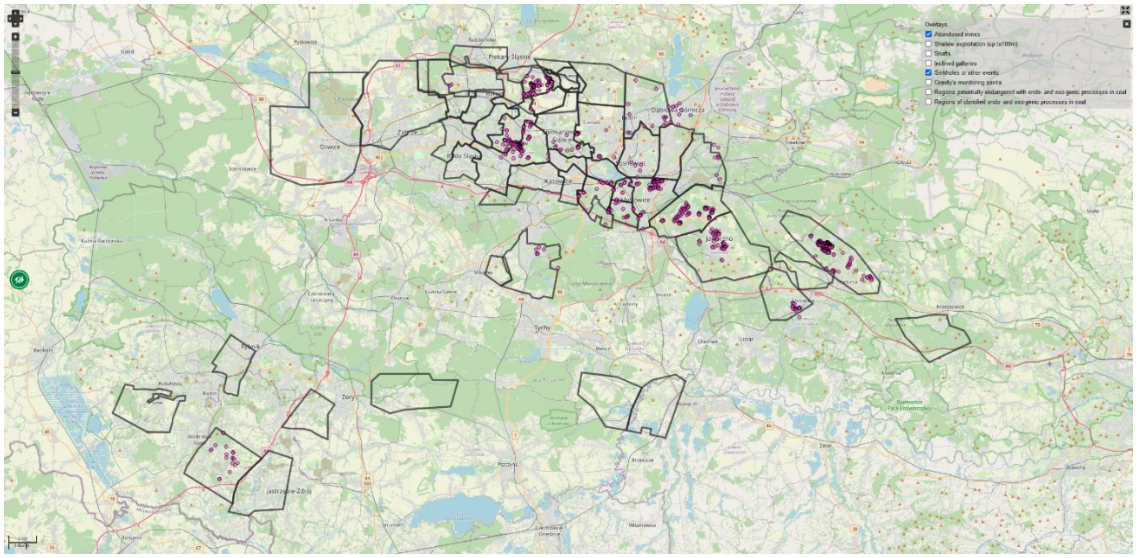

Figure 2.17 Map showing all the sinkholes recorded in the USCB by the Polish Geological Institute. Source: https://zapadliska.gig.eu/en/content/map

2.4 Detection, monitoring, mitigation, and remediation activities

Mitigating the hazards and unpredictability associated with sinkholes is critical and might by partly addressed through a comprehensive "prevention and safety process". This process includes detection, monitoring, risk assessment, and remediation measures.

Although sinkholes appear with little warning, the appearance of tension cracks, cracks in infrastructure and surface subsidence are often early warning signs of sinkhole development. Such surface deformation might occur weeks to months before sinkhole formation as the erosion of the roof material causes upward migration of the cavity. Sinkhole formation is by nature abrupt, and the location of underground cavities is frequently unknown. It is therefore challenging to identify and analyse the associated small-scale precursory deformation. Furthermore, in situ monitoring of large areas is not feasible (Theron et al., 2017).

Sinkholes are more challenging to detect than larger scale deformation features due to their small size, unpredictable nature, and non-linear deformation rate. Recent research has indicated that precursory surface subsidence can occur and that differential interferometry techniques (DInSAR) can accurately detect it months to years before the event (Nof et al., 2013). It has, however, been found that some collapse sinkholes did not exhibit precursory subsidence and not all deformation events lead to collapse events (Rucker et al., 2013).

Various measurement methods, such as Global Navigation Satellite System (GNSS), tachymetry, laser scanning and photogrammetry, prove to be crucial for monitoring existing sinkholes. For instance, aerial laser scanning generates a georeferenced map by recording a point cloud from a drone. The global navigation satellite system (GNSS), which uses light pulses and measures their travel time, is particularly useful for determining singular point's coordinates and has a significant advantage in forested regions.

High-precision levelling, another fundamental technique, involves the construction of topographic profiles by measuring the difference in elevation between successive points using digital levels and electronic bar-coded stick readings. (Kersten et al., 2017) exemplified the application of this method in subsidence monitoring in Bad Frankenhausen, Germany, as documented by Gutiérrez et al. (2019). Collectively, these monitoring techniques contribute to the early detection and understanding of sinkhole-related subsidence, enabling early intervention and remediation efforts.

Satellite techniques, in particular Interferometric Synthetic Aperture Radar (InSAR), have emerged as the most widely adopted method for mapping sinkholes and monitoring long-term deformations (A. A. Malinowska et al., 2019). This approach provides a comprehensive and efficient means of analysing and monitoring ground deformation, offering valuable insights into

the dynamic nature of sinkholes and facilitating a more informed understanding of geological changes over time.

SAR makes it possible to obtain images with high resolution by observing, along its orbit, the same portion of the terrain under different viewing angles and combining different contributions related to the same cell. SAR-type radar systems enable high-resolution imaging of the Earth's surface. For this purpose, they measure the sensor-target distance by recording the elapsed time between the emission of an electromagnetic wave from the satellite-mounted radar sensor to the Earth's surface and the reception of the backscattered signal from the target on the ground (Pigorini et al., 2010).

Radar waves, unlike infrared light, offer two significant advantages: the ability to penetrate meteorological clouds and an effective activity in the dark. However, interferograms, a key element of radar imaging, can be susceptible to alterations caused by topographical and atmospheric effects. To address this challenge, various techniques, such as PSInSAR or SBAS InSAR were introduced. According to (Vaccari et al., 2013), under specific conditions, these approaches have demonstrated the ability to provide deformation measurements with an accuracy of less than 1 cm. PSInSAR and SBAS InSAR thus present itself as a valuable tool to overcome limitations associated with topographic and atmospheric influences, improving the accuracy and reliability of deformation measurements.

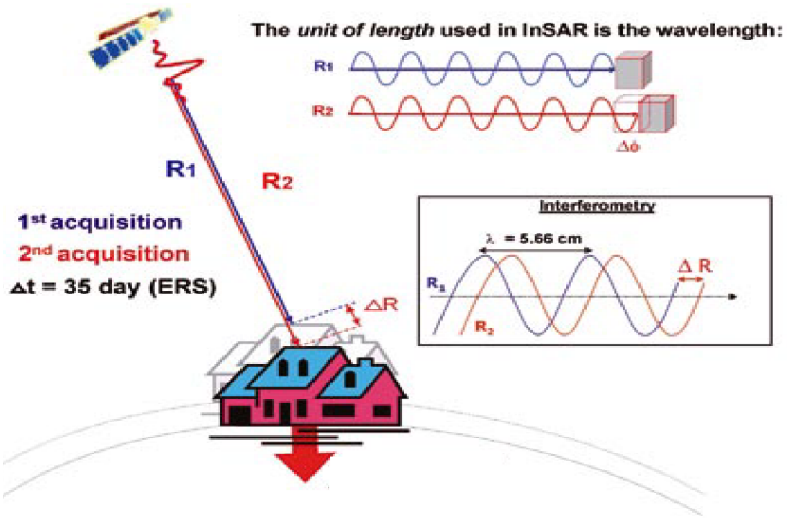

Figure 2.18 Basic refiguration of how PSInSAR works. Source: (Oštir & Komac, 2007)

The second key step in the "prevention and safety process" is risk assessment. In order to obtain a complete assessment, a detailed geotechnical investigation must be conducted to accurately

identify and describe the site. A thorough investigation should include information about previously collapsed sinkholes, including the date of occurrence, potential causes and types, and measures implemented. Moreover, it should cover geological aspects through boreholes and geological profiles, hydrogeological factors (aquifer details, piezometers, and hydrological parameters), and details on mining activities, such as the method of exploitation and start-end dates (A. A. Malinowska et al., 2019). Common techniques used in on-site investigations for zoning and description include aerial photographic studies, surface geological mapping, geophysical surveys (mainly gravity studies), and percussive drilling.

Inherent risk associated with sinkholes, generally depends on the mobility of the overburden and future land use. Since it is difficult to predict the safety of future land use, it must be assumed that the site may be improperly developed or treated (abused).

The frequency of sinkholes might increase over time, particularly with ageing and the development of leaks in essential infrastructure such as sewer systems and aqueducts.

Therefore, a risk assessment approach must take into account the cumulative impact over a specific period, thus helping to develop strategies for effective risk management and mitigation. The development risk is a comprehensive assessment that considers both the inherent risk and the type of future development of the chosen land. For instance, if a high-density residential building is planned on the land, there may be concern about seepage from leaking hydraulic systems, as described above. It is critical to note that precautionary measures should be implemented before the construction begins to minimise ground disturbance. Given the impetuousness and inherent hazards associated with sinkholes, the associated risk cannot be easily classified only as low, medium, or high, indeed, it must be characterised as acceptable or not. This determination requires professional judgments based on site-specific investigations. The assessment involves a thorough consideration of multiple factors, such as soil properties, the type of development anticipated, and potential impacts on ground stability. This nuanced approach ensures that the risk assessment is tailored to site-specific conditions, enabling informed decisions and effective risk management strategies. (Buttrick & Van Schalkwyk, 1998).

Geotechnical investigations play a key role not only in risk assessment but also in determining the most suitable rehabilitation methodology. The chosen rehabilitation method is influenced by several factors, including available funding, existing and future land use, geological considerations, groundwater levels, site accessibility, and the amount of available information. A critical parameter in this decision-making process is the depth of impact caused by a sinkhole. For shallow depths, typically up to a maximum of 10 m, excavators or backhoes are commonly

used to reach the core of the subsidence. This versatile equipment is effective for dealing with sinkholes that have less impact on the ground. For deeper sinkholes, instead, alternative methods such as augers are more suitable. These facilities are equipped to address the challenges posed by deeper sinkholes, allowing for a more comprehensive and focused rehabilitation approach. Choosing the appropriate rehabilitation method is a nuanced decision that takes into account the specific characteristics of the sinkhole, ensuring an effective and tailored response to the geotechnical challenges presented by each case (Zhou & Beck, 2008). Several critical parameters are considered when choosing the best rehabilitation method for sinkholes at different depths:

- Cause of sinkhole or subsidence formation: this can depend on the entrance of water (i.e., pipes leaking) or groundwater level variation (i.e., dewatering due to mining or agricultural activities);
- Complexity of the geological model: this depends on many different factors such as the overburden layer (i.e., the presence of faults or fractured zones, the geotechnical properties of the material which the overburden layer is composed of), the dolomite bedrock (i.e., depth and morphology), the depth of the groundwater level (i.e., if it is located above material with high mobilisation potential);
- Vertical and lateral extent of instability features, triggering mechanisms and impact on existing infrastructures (i.e., buildings, roads, gas pipes, water pipes, electrical cables);
- Future use of the land after the rehabilitation.

A widely adopted rehabilitation method is the inverted filter method. This approach involves filling the sinkhole with filling material and a material called “soilcrete” (a mixture of sandy gravel with 3 per cent to 5 per cent cement and water) or self-compacting concrete. The filling process is completed with progressively finer materials that are compacted to create an impermeable cover. This method is particularly suitable for dealing with small to medium-sized sinkholes, such as those depicted in Figure 2.19. The choice of this method highlights its effectiveness in providing stability and preventing further subsidence in those areas where it is applied (Kleinhans & Van Rooy, 2016) .

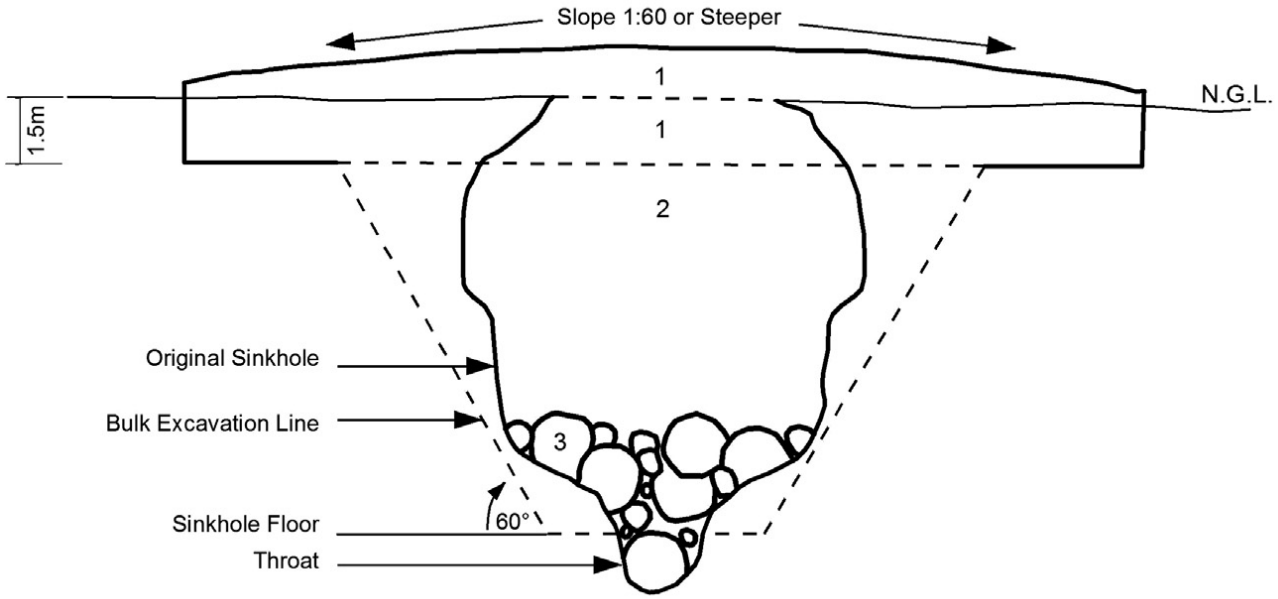

Figure 2.19 Scheme of the inverted filter method. Source: (Kleinhans & Van Rooy, 2016)

Unfortunately, the appearance of sinkholes causes a cascade of consequences with environmental (Soldo et al., 2020), social (Japan: Repaired Fukuoka Sinkhole Sinks Again - BBC News), and economic ramifications (Rome: Sinkhole Opens up in Front of Pantheon - Wanted in Rome).

The environmental repercussions manifest themselves as a direct impact on water surfaces: lakes, streams, and entire aquatic ecosystems suffer the consequences, struggling against soil erosion and sedimentation. The consequences extend further, as sinkholes contribute to habitat alteration, leading to the loss of flora and fauna, reshaping of the natural landscape, and influencing the water availability for human and agricultural purposes (Soldo et al., 2020).

Sinkholes could also represent a way to pollute groundwater by transporting contaminants, such as insecticides, herbicides and fungicides.

(Mir et al., 2023) document the sinkhole formed on February 11, 2022, in the Brengi stream, one of the major tributaries of Upper Jhelum River in Kashmir Himalaya. This phenomenon swallowed the entire stream flow causing mass mortality of fish and other aquatic species.

On the social side, the threat of sinkholes extends to the area of human health and safety, especially when these geological phenomena affect urban or residential areas. Buildings, roads, and critical infrastructure are vulnerable to damage and compromise daily routines that rely on the continuity of transport and business activities. The psychological toll is no less significant:

living or working in areas prone to sinkholes occurrence can cause psychological stress and anxiety (Figure 2.20).

Figure 2.20 Sinkhole occurred in Fukuoka, Japan. Source: (Japan: Repaired Fukuoka Sinkhole Sinks Again - BBC News)

From an economical perspective, sinkholes result in substantial property damage and losses, with repercussions for individuals, businesses, and communities. Property values and insurance rates may be affected, and the costs of infrastructure maintenance and repair can increase. Moreover, sinkholes can affect tourism and those industries that rely on natural resources and scenic landscapes.

Figure 2.21 shows a sinkhole appeared in front of the Pantheon, Rome, in April 2020. Due to the quarantine of Covid-19 pandemic, nobody was harmed by this event. Further studies assess the indirect importance of that sinkhole because of the discovery of ancient ruins.

Figure 2.21 Sinkhole appeared in front of the Pantheon, Rome. Source: (Rome: Sinkhole Opens up in Front of Pantheon - Wanted in Rome)

2.5 Land subsidence

Land subsidence is a sudden or gradual settling of the land surface caused by changes in the stress regime of the structure of subsurface (Gambolati & Teatini, 2021).

These changing is provided by anthropogenic activities, such as mining excavations and, most of the time, groundwater extraction.

Sinkholes are strictly related to land subsidence since the only way to predict them is to monitor the land vertical displacement with the technologies already explained. Once the subsidence reaches a maximum value, the soil starts to collapse, and, with the adequate conditions, sinkholes occur.

2.5.1 Land subsidence due to groundwater extraction

Before starting the mining activities, the area must be drained by pumping out water through wells. Eventually, the pumps are switched off and the water is allowed to flood the mine.

When an aquifer is pumped, pore water pressure can no longer support as large a percentage of the load from overlying formations. Therefore, more of this load must be borne by the grain-to-grain contacts (effective stress) of the geological material itself, with a stress transfer from the fluid to the solid phase. This increase in effective stress develops in both the pumped units

and the adjacent formations that compact. The amount of compaction is primarily related to the compressibility (sub-chapter 5.1.3) of the compacting layers.

The introduction of a pumping well into a naturally flowing fluid system produces a perturbation that impacts the geological medium. Near the well, a fluid head cone of depression develops and expands both horizontally and, to a lesser extent, vertically (Figure 2.22) (Gambolati & Teatini, 2021).

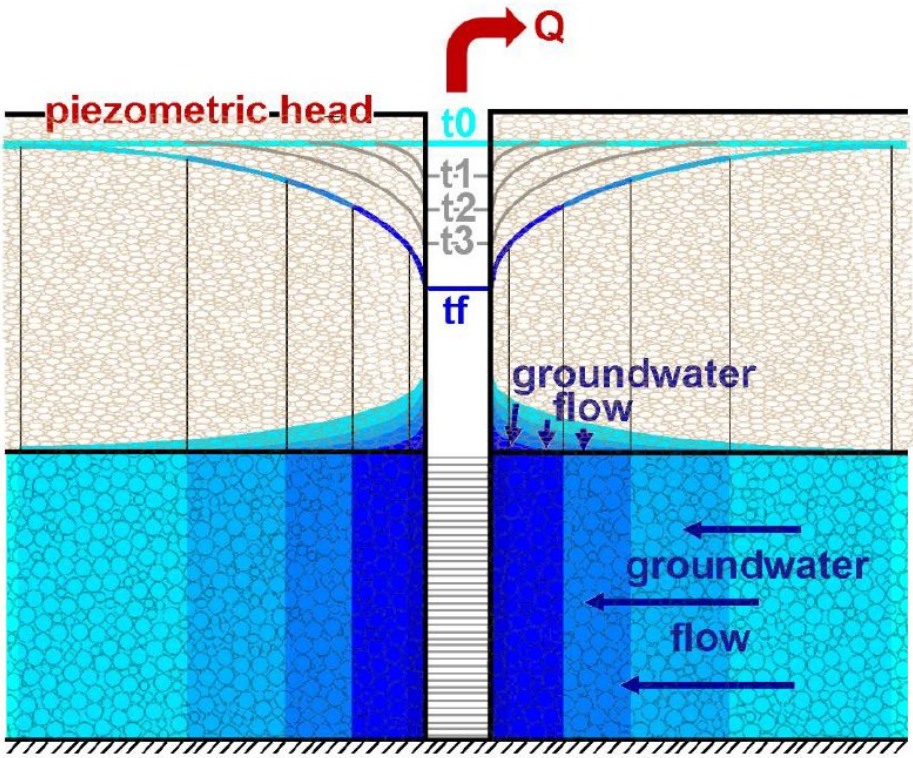

Figure 2.22 Groundwater withdrawal from a well causes piezometric head decline in the pumped aquifer. The piezometric head declines over time from the initial time (t0) level to the final time (tf). Source: (Gambolati & Teatini, 2021)

2.5.2 Land subsidence due to mining deposits extraction

Nowadays, hard coal mines can exceed depths of 1,200 in some European countries, and of 3,000 m for gold mines South America and South Africa (He, 2006). The performance of the deformation mechanism of rock varies with the depth: in general, the deeper the depth, the strongest the rock strength. In deep hard coal deposits, due to the properties of soft rock and high stresses, large deformations can occur in the rock mass (Ribeiro e Sousa et al., 2012).

Land subsidence due to mining is mainly caused by removing a deposit from a rock mass and forming a post-mining void. The major factors for assessing the land subsidence's spatial extent and value are the depth of exploitation, seam thickness, panel dimensions, overlying rock mass

geomechanical conditions, surface topography, production methods and post-mining void reclamation method (Guzy & Witkowski, 2021). According to research paper (Blachowski et al., 2019; Cai et al., 2020; Milczarek et al., 2021) the spatial extent of the phenomenon can range from several km^2 to tens of km^2, while its values can range from a few mm/year to several cm/day. Guzy & Witkowski (2021) show that the land movement due to groundwater extraction is small if compared to the one caused by mining deposit exploitation.

Areas above former mining workings lie in a subsidence basin zone. The extent of this subsidence depends on the thickness of the extracted seams and the method of void space closure. Particularly noticeable subsidence occurs in uninhabited areas where seams were mined by caving (the hard coal seam was extracted, the space was not filled, and the roof collapsed). In such areas the ground locally subsided by 14 m. In built-up areas, where backfilling was used, the subsidence is up to 2 m.

For above-ground structures, the effects of shallow mining (i.e., the oldest, 19th-century mines) are much more severe because the most significant ground movement occurs just above the exploited seam. The deeper the mine, the more likely it is that the overlying rocks will arrange themselves in a way that supports the roof.

Chapter 3

The Silesia region: history, mines, and green energy transition

3.1 History framing of the Upper Silesia Coal Region

Upper Silesia is located in the southeastern part of the larger historical and geographical region of Silesia, situated in Central Europe (Figure 3.1). Today, it is predominantly within Poland, with minor areas extending into the Czech Republic. The region spans approximately 13,230 km^2. Historically, Opole served as the capital of Upper Silesia. However, the current major urban centers are Katowice in Poland and Ostrava in the Czech Republic, both with a population of approximately 280,000 inhabitants. As of 2022, the total population of Upper Silesia is around 2,500,000.

Figure 3.1 Location of the USCB against the backdrop of European country borders in 1939 and 2024. Major cities of the region. Basemap: OpenStreetMap.

Geographically and historically, Upper Silesia has always been at the junction of three areas that have, over centuries, been part of Poland, Germany, and the Czech lands. The region's history is characterized by numerous border changes, dating back to the early centuries.

Following World War I, a significant portion of the Silesia region became a contested area between Poland and Germany. Between 1919 and 1921, the Polish-speaking population of Upper Silesia initiated three uprisings. A 1921 referendum led to the region being almost equally divided between Poland and Germany, with the final border determined by the Polish-German Accord on East Silesia, signed in Geneva on May 15, 1922.

The German invasion of Poland in September 1939, marking the onset of World War II, saw numerous massacres of Polish civilians in Upper Silesia by German forces. Subsequently, the region was annexed to Nazi Germany, and the Polish population faced extensive persecution and atrocities. Notably, several subcamps of the Auschwitz concentration camp were established in Upper Silesia.

After 1945, nearly all of Upper Silesia, not previously ceded to Poland in 1922, was placed under Polish administration. The majority of the German-speaking population that had not fled was expelled, a measure in line with the decisions made by the victorious Allied powers at the 1945 Potsdam Conference. These German expellees were relocated to present-day Germany, while Polish migrants, many of whom were expellees from former Polish territories annexed by the USSR, resettled in Upper Silesia. A considerable number of German-speaking Upper Silesians found new homes in Bavaria. A smaller portion of Upper Silesia remained part of Czechoslovakia, known as Czech Silesia.

Currently, the Polish portion of Silesia is administratively divided into three voivodeships: Silesian, Lesser Poland, and Opole. The Czech portion is integrated with the northern Moravian region, forming the Moravian-Silesian region.

Given the complex history, it is important to note that many valuable documents, including mining and geological maps containing information on hard coal exploitation, as well as details on the adverse environmental impact of mining, were destroyed during World War II.

3.2 Importance of hard coal mining for Poland: an historical overview

Poland has a rich history of abundant mineral and natural resources, with significant mining activities tracing back to the 15th century, particularly in the Lower and Upper Silesia regions. This period initiated the extraction of precious minerals such as silver, gold, and salt, alongside building stones used in the construction of castles, defensive structures, towers, and sacred edifices. The partition of Polish territories in 1772 among Prussia, Russia, and Austria led to

the segmentation of mineral resource extraction sites and the emergence of distinct raw material and mining policies. This era was notable for considerable scientific and technological advancements that laid the groundwork for the forthcoming industrial revolution. Consequently, hard coal mining in Lower and Upper Silesia saw significant expansion, with production escalating from 3.6 thousand tonnes in 1769 to nearly 200 thousand tonnes at the onset of the 19th century. The invention of the paraffin lamp further stimulated subsoil exploitation, catalysing the development of the oil mining industry both within Polish territories and worldwide.

By around 1880, natural gas began being utilized in heating and petrol distillation. Concurrently, steam pumps were introduced to drain water from mines, thereby prolonging the lifespan of Upper Silesian mining operations. The disruptions caused by the First and Second World Wars devastated the Polish economy, necessitating a post-war resurgence with new territories and a reformed economic and social framework. Reactivated in 1945, the Polish Geological Institute has been responsible for monitoring the geological structure of these new lands and evaluating their natural resource potential.

Hard coal has become a pivotal resource in Poland, significantly contributing to the nation's development (Piwocki & Przeniosło, 2004). Between 1900 and 1984, Poland consistently ranked among the top five global hard coal producers, alongside the US, USSR, UK, and Germany (Szpor & Ziółkowska, 2018). Despite its historical significance, the coal sector encountered challenges in the 1970s, hindered by inefficiencies and restricted access to international markets.

In light of Poland's democratic transition in 1989, initiatives were undertaken to rejuvenate the coal sector, aiming to reinstate its prominence in the Polish economy through enhanced productivity and profitability. This restructuring involved a substantial redundancy program and the shutdown of unprofitable mines. As a result, hard coal production declined dramatically, dropping from 300 million tonnes in the 1980s to merely 73 million tonnes in 2014. Nevertheless, Poland retained its position as the leading coal producer among EU member states, accounting for 1.2% of global hard coal production.

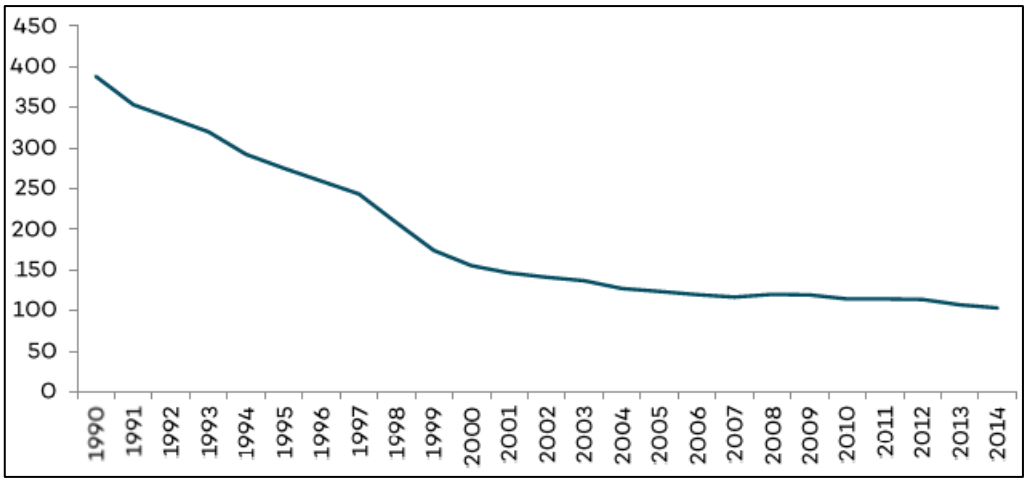

Figure 3.2 Employment in the coal mining sector (the vertical axis represents hundreds of thousands of workers). Source: (Szpor & Ziółkowska, 2018)

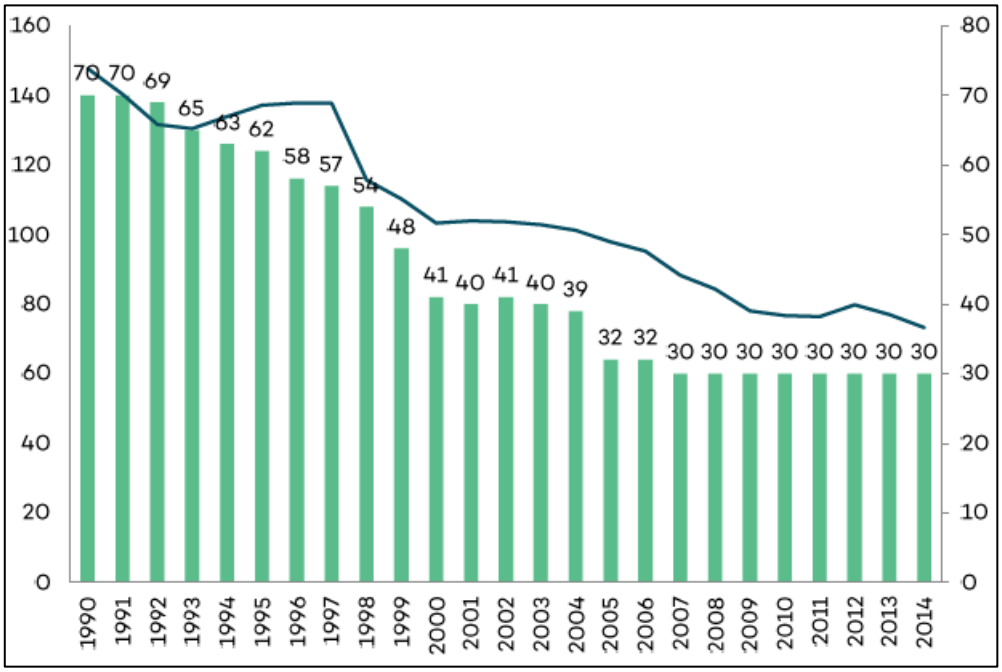

Figure 3.3 Decrease of production of hard coal (blue line) and number of collieries (green columns). Source: (Szpor & Ziółkowska, 2018)

Hard coal continues to play a fundamental role as a primary energy source in Poland, influenced not only by historical considerations but also by the scarcity of alternative energy sources domestically. However, there has been a marked reduction in hard coal usage, decreasing from 76% to 60% between 1990 and 2000 (Szpor and Ziółkowska, 2018).

In 1990, hard coal was the predominant source of electricity, contributing to almost 95% of the total annual electricity generation. Nevertheless, the ensuing decade witnessed a significant shift in response to evolving EU environmental policies. The proportion of alternative fuels,

especially those from renewable sources, increased in the 2000s, aligning with the objectives of EU environmental directives.

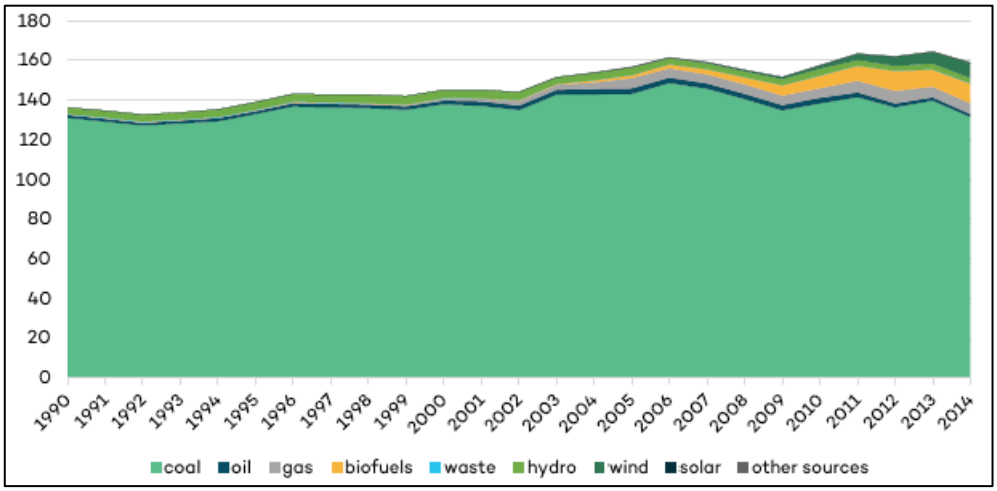

Figure 3.4 Electricity generation for each fuel (TWh). Source: (Szpor & Ziółkowska, 2018)

3.3 The energy transition: the closure of mines for a green development

The scientific consensus acknowledges that human activities are likely the primary cause of the global temperature rise, commonly referred to as global warming, since the mid-20th century. This trend of human-induced warming is expected to continue throughout the 21st century and beyond. In response to these concerns, the United Nations Framework Convention on Climate Change (UNFCCC) has facilitated several agreements aimed at preventing further increases in global temperatures and mitigating climate change. A key international agreement is the Kyoto Protocol, adopted on December 11, 1997, which mandates specific emission reduction targets for developed countries. These countries are required to collectively reduce their greenhouse gas emissions by 5% (relative to 1990 levels) by the end of the first commitment period (2008-2012).

A significant update to the Kyoto Protocol occurred on December 8, 2012, during the 18th Conference of the Parties in Doha. The Doha Amendment introduced a second commitment period (2013-2020), during which parties committed to reducing greenhouse gas emissions by 18% below 1990 levels (What Is the Kyoto Protocol? | UNFCCC). On December 12, 2015, 196 Parties at the United Nations Climate Change Conference (COP21) adopted the Paris Agreement. The primary goal of this agreement is to limit the global average temperature increase to less than 2°C above pre-industrial levels (The Paris Agreement | UNFCCC).

Currently, there is a global trend of moving away from fossil fuels towards clean energy. One of the main aspects of the energy transition is moving away from hard coal. In accordance with these agreements, Poland must find a way to transition from coal-fired electricity to more environmentally friendly alternatives. A crucial step in this process is the cessation of mining operations and the abandonment of mining sites.

The rapid pace of decarbonization in the Polish energy sector is necessary to meet the commitments of international agreements, especially the Paris Agreement. To fulfil its provisions, all European Union countries, including Poland, must move away from coal combustion by 2030 at the latest.

According to the current energy strategy of Poland, adopted by the previous government in 2022, Poland is set to move away from hard coal in energy production by 2049 (Energy Policy of Poland until 2040 (EPP2040) - Ministry of Climate and Environment). However, the current government, established at the end of 2023, is working on updating the country's energy strategy. The main goal is to set 2035 as the final date for using hard coal in Polish energy production. This date allows for a relatively rapid reduction in the cost pressure associated with coal energy exploitation in Poland on the prices of electricity and heat. At the same time, it is a sufficiently distant date to create new production capacities and ensure energy supply security. Any delay in this date should only be permissible in the event of a threat to Poland's energy supply security. In such cases, an extension of the coal phase-out date should be allowed, up to a maximum of 2040.

The necessity to set a coal phase-out target is indicated by both external and internal conditions. Among the most important aspects are:

The deteriorating condition of hard coal-fired power units, many of which are nearly 50 years old. The availability of these units is decreasing, and the reserve power levels are getting lower.

The high cost of electricity production from hard coal poses a significant burden on the economy. Subsidizing mining, coal generation, and consumers to afford expensive electricity is a waste of public funds.

The current pace of new unit construction, financial mechanisms, and administrative procedures enabling their establishment are insufficient and not adapted to the scale of the challenges. Setting a specific coal phase-out date will mobilize the necessary investment processes and supporting regulations.

The current situation in the hard coal mining segment is economically disastrous. The decline in mining levels combined with rising costs leads to the complete uncompetitiveness of the

Polish mining sector. Despite high domestic coal prices, the coal sector still demands support from public funds. Most of the extraction of energy coal in Poland is permanently unprofitable. Maintaining coal energy in Poland longer than absolutely necessary means, among other things, increasingly higher prices for electricity and heat (due to expensive raw materials and expensive CO2 emission rights) and worsening the situation of Polish exporters and making it difficult to place foreign investments in Poland due to the high carbon footprint.

Achieving the goal of phasing out coal by 2035 requires coordinated actions and cooperation in several areas. The most important are:

Planning to supplement the power balance and implement market and financial mechanisms. A coherent vision of quantitative goals for various system supplements alongside the diminishing coal power and ensuring its safe and uninterrupted operation in conditions of high renewable energy sources (RES) share is necessary.

Organizational transformations: separation of coal assets or another form of restructuring, preceded by an audit of the state of work on the current concept of the National Energy Security Agency (NABE).

Introduction of a compensation mechanism for producers for the early decommissioning of coal capacities within the so-called Early Decommissioning Mechanism (EDM).

Establishment of the Coal Commission along with expert support and broad authorization. This will allow for the development of a detailed plan to close hard coal-based energy in Poland and appropriately adjust the mining potential of Polish mines to this plan.

The planned closure of underground hard coal mines in the coming years will cause a large-scale environmental impact, which is difficult to estimate and define its consequences. When a mine ceases its operations, the pumps, used to lower the aquifer pressure in the working area, are turned off, allowing water to re-enter. At closure, when the pumps are switched off, water enters the mine, increasing the pore pressure within the rock mass and causing ground uplift. Additionally, piezometric rebound can lead to an unfavourable stress distribution, compressing the rock mass and causing sinkholes to form. Therefore, water rebound plays a crucial role in soil weakening and the subsequent formation of sinkholes, as briefly discussed in Chapter 2. Unfortunately, these phenomena are expected to increase over time in all territories characterized by extensive mining abandonment. There is a considerable gap in general knowledge about the mechanics of sinkhole formation due to piezometric rebound in post-mining regions.

Chapter 4

Case study: the Siersza mine

4.1 Study area

The research for this thesis was carried out in the area of the abandoned underground hard coal mine “Siersza” situated in Poland, specifically between Katowice and Kraków, directly in the Trzebinia locality, on the northeastern slope of the USCB (Figure 3.1).

The study area is located at an average altitude of about 340 m.a.s.l., with terrain undulations not exceeding a few dozen meters. It is an urbanized area, inhabited by several tens of thousands of people, and is traversed by roads and railway lines of regional significance.

The research was conducted within the region shown in figure 4.1, which includes two distinct sub-areas. The smaller sub-area corresponds to the area of the Siersza mine. This sub-area spans 3 km by 13 km, covering a total area of approximately 40 km^2. The larger outer buffer area is elliptically shaped, stretching 23 km in a northwest-southeast direction, linking the towns of Olkusz and Libiąż. It also extends 33 km in a northeast-southwest direction, covering a total area of 653 km^2.

Over the years, several mines were established in this area, including Izabella in 1808, Artur in 1880, and Zybszek in 1920. Each operated independently until 1947 when they were interconnected through the construction of a horizontal underground tunnel linking the Artur and Zybszek mines (Figure 4.2). This consolidation resulted in the adoption of the current name “Siersza” mine.

Mining activities in the “Siersza” mine continued until the 1990s, leading to the closure of the Artur, Walter, and Paula auxiliary shafts. Ultimately, the mine was completely abandoned in 2001 (Banks et al., 2010). Since that time, a continuous groundwater rebound and associated land uplift are observed.

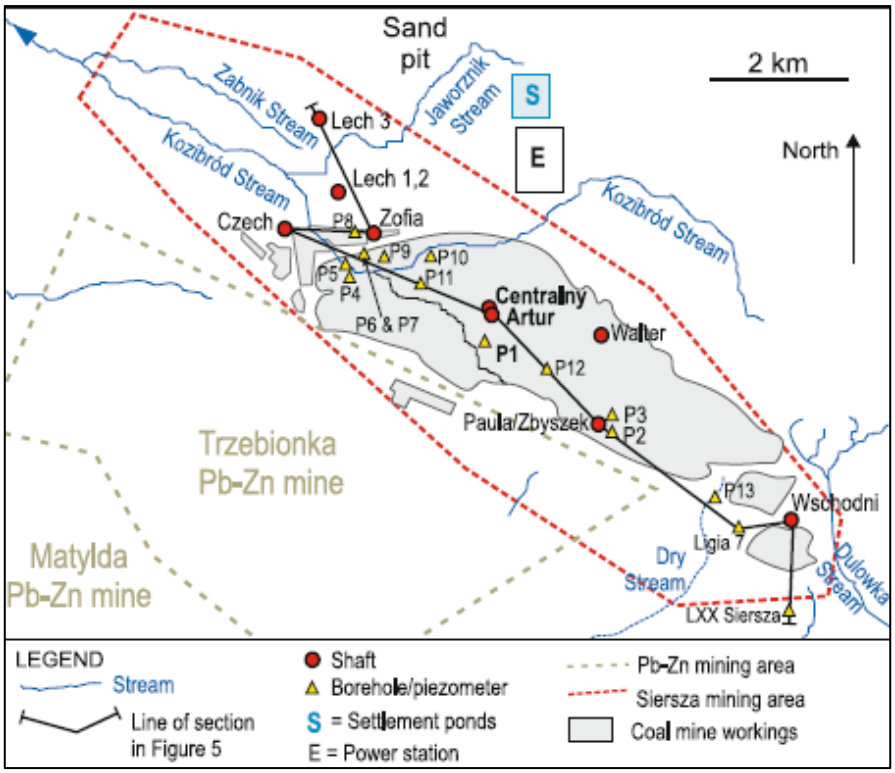

Figure 4.1 Map of Siersza mining complex. Source: (Banks et al., 2010)

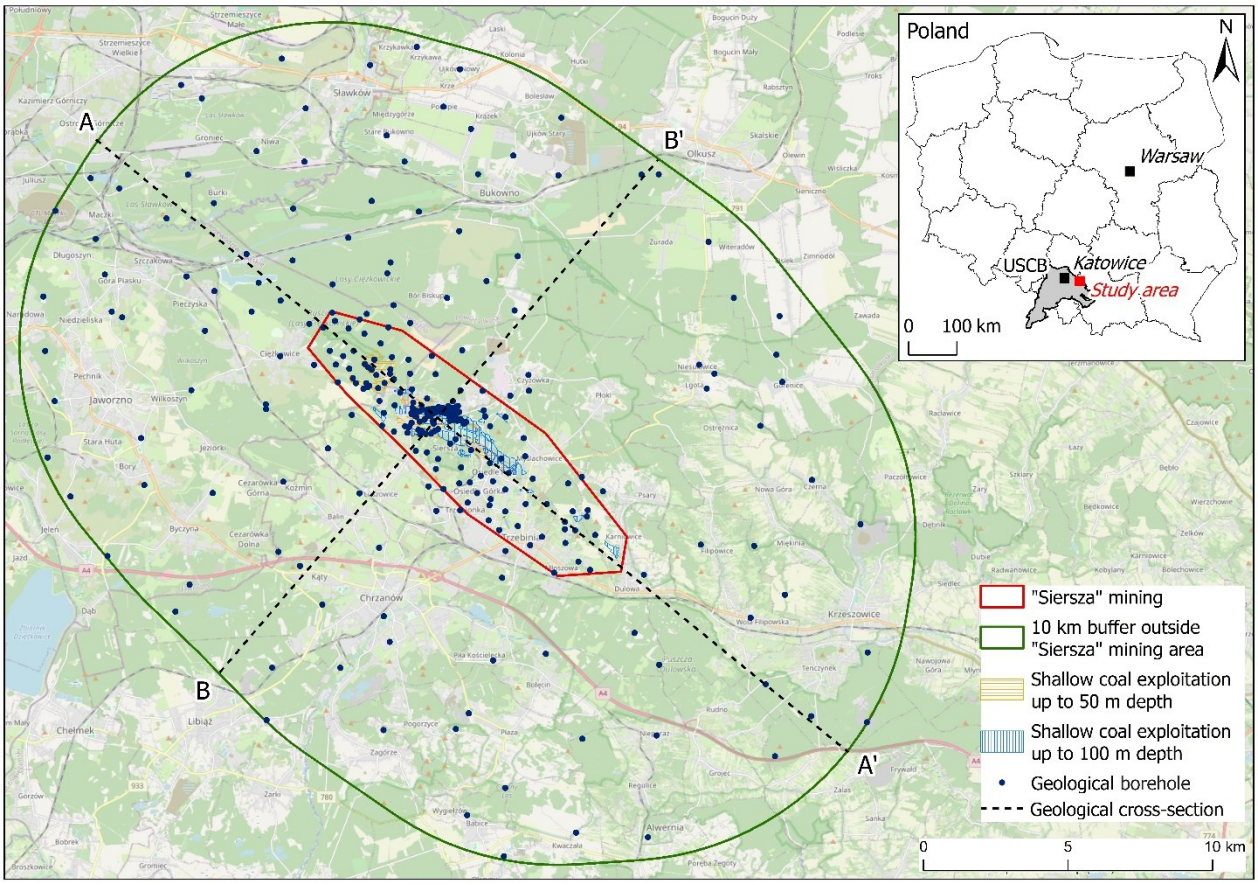

Figure 4.2 Whole study area

4.2 Geological structure of the deposit

4.2.1 Lithology and stratigraphy

The geological structure of the Siersza ore deposit, reported to reach a depth of 1,000 m, comprises six strata, listed from top to bottom: Quaternary, Neogene, Jurassic, Triassic, Permian and Carboniferous. The Carboniferous layer is characterised by four main lithostratigraphic series: the Cracow Sandstone, the Mudstone Series, the Upper Silesian Sandstone and the Paralic Series.

In the area of the Siersza mine, the carboniferous material is relatively shallow and extends to a depth of about a dozen metres, particularly in the central and partially northern parts. Triassic, Permian and Quaternary overburden layers are respectively present in the south-western, south-eastern and northern parts of the deposit (Figure 4.3). In particular, the figure highlights the significant presence of the Quaternary layer above the Carboniferous layer.

It is important to highlight the substantial variation in the thickness of the carboniferous layer, ranging from 0.2 to 54.6 m.

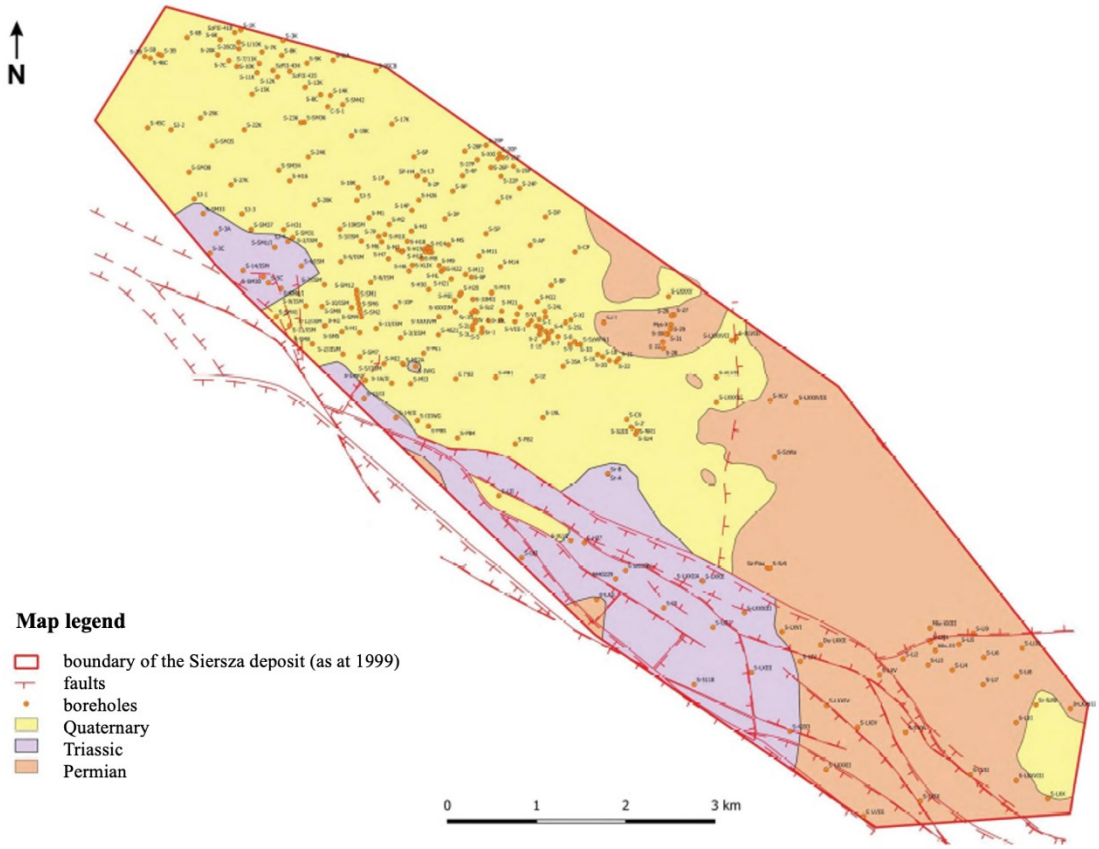

Figure 4.3 Map of overburden deposits on the Carbon roof. Source: (Report on Analytical Work on Terrain Deformations in Trzebinia, Polish Geological Institute, 2023)

In terms of lithology, the Quaternary sediments of the Siersza ore deposit present various compositions, including:

- Eroded limestone, dolomitic rocks and Carboniferous rocks, comprising rock debris of different size;
- Fine- to medium-grained quartz sands, typically yellow or light grey, occasionally containing iron;
- Yellow brown, slightly sandy clays containing small fragments of Triassic, Jurassic or Permian rocks;
- Loessic clays, locally present in the south-eastern part of the deposit area;
- Silt and Holocene clays of limited thickness, sporadically occurring in river valleys.

The Neogene formations are limited to the southern part of the town of Trzebinia, located on the southern edge of the Siersza deposit. These formations can reach a thickness of 51 m and are mainly composed of various types of clay.

The Jurassic sediments are concentrated in a small area in the south-eastern part of the deposit, with thickness of up to 158 m. The Upper Jurassic comprises marls and marly limestones, with thickness between 55 and 145 m, while the Middle Jurassic is characterised by sandstones, conglomerates and oolitic limestones, with thickness between 1 and 15 m.

Triassic formations are prevalent in the southern and western parts of the Siersza deposit, with thickness of up to 158 m. The Upper Triassic consists of clays and mudstones, with thickness ranging from 0 to 120 m, while the Lower Triassic consists of the Rhaetic and Świerklaniec strata, which lie at depths of 20 to 30 m.

The Permian sediments in the eastern part of the deposit are characterised by red-bed sediments, with thickness ranging from 20 to 172.5 m (Report on Analytical Work on Terrain Deformations in Trzebinia, Polish Geological Institute, 2023).

To provide an overview of the thickness of these cover layers, figure 4.4 is given as a reference.

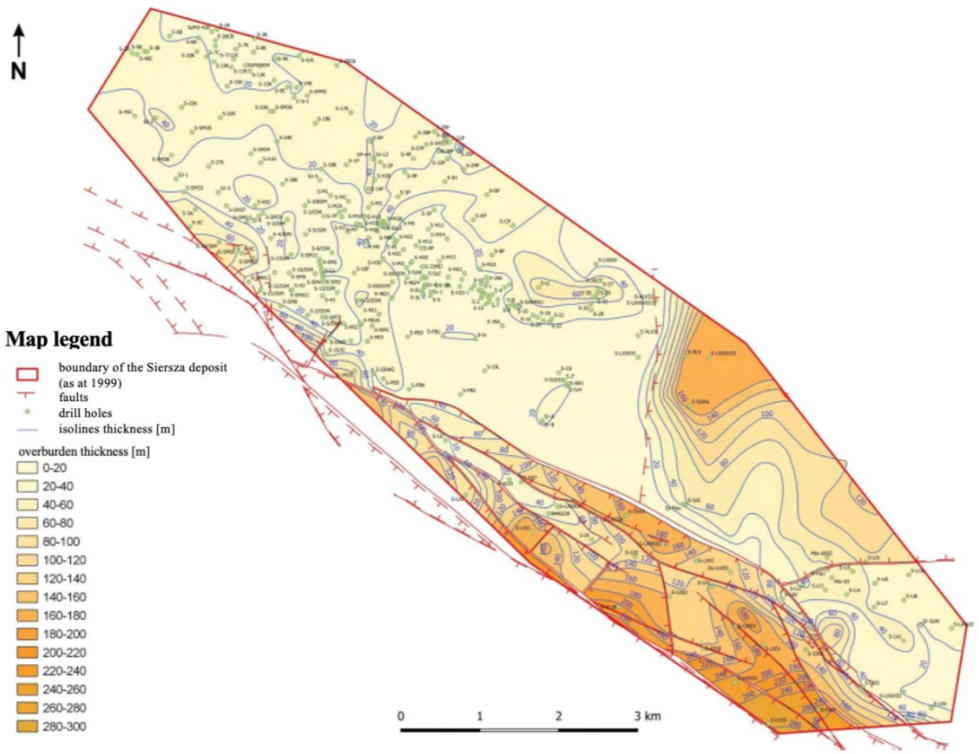

Figure 4.4 Carbon overburden thickness map. Source: (Report on Analytical Work on Terrain Deformations in Trzebinia, Polish Geological Institute, 2023)

The section of the Siersza mine deposit is shown in figure 4.5, in which the great presence of Quaternary layer can be assessed.

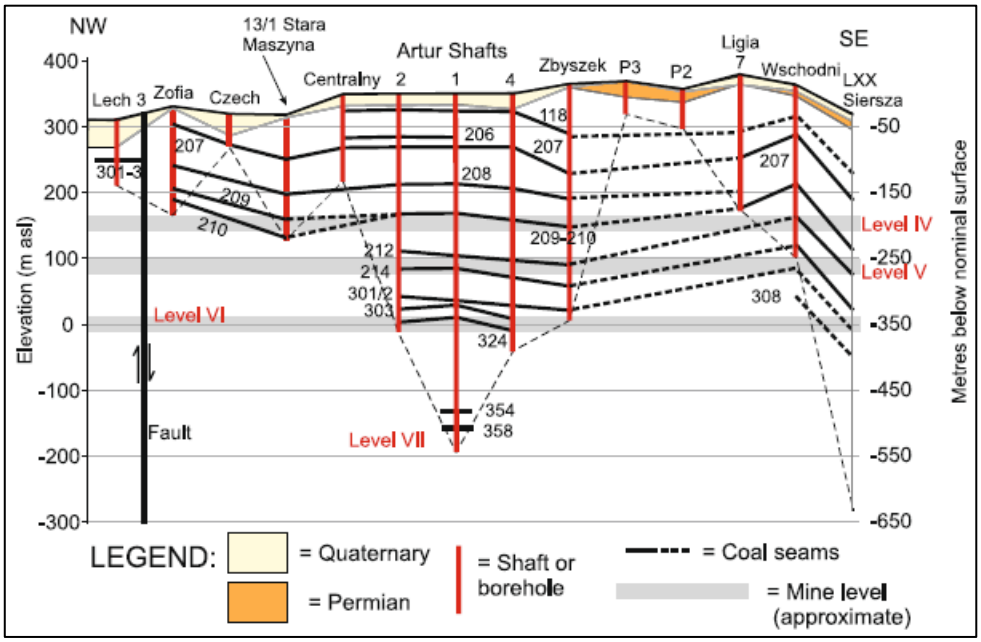

Figure 4.5 Cross section along strike of Carboniferous strata. Source: (Banks et al., 2010)

4.2.2 Tectonics

The Siersza mining unit is located in the eastern part of the Wieliczka Basin, which is characterised by a complex system of faults, amply depicted in figure 4.6. The basin is characterised by the presence of significant fault lines that predominantly follow two directions. The youngest faults have an east-west orientation and strike both the Carboniferous and the younger layers. In contrast, the older and larger faults run mainly in a north-south direction and are limited to the Carboniferous layer.

Within the Siersza mine, the most important faults generally have a northwest-southeast orientation. These faults include the Sierszański I, Sierszański II, Południowy, Baliński, Trzebiński, Młoszowski and Karniowicki faults.

Despite the generally modest inclination, with layers plunging at angles of no more than 15 degrees, there is considerable variability in the depth of the hard coal seams. For instance, seam 301 in the northern part of the deposit is at a depth of +310 m.a.s.l. In the southern axis of the basin it is at -80 m.a.s.l., in the displaced wing of the southern fault at -160 m.a.s.l., and further south at +170 m.a.s.l. (Report on Analytical Work on Terrain Deformations in Trzebinia, Polish Geological Institute, 2023).

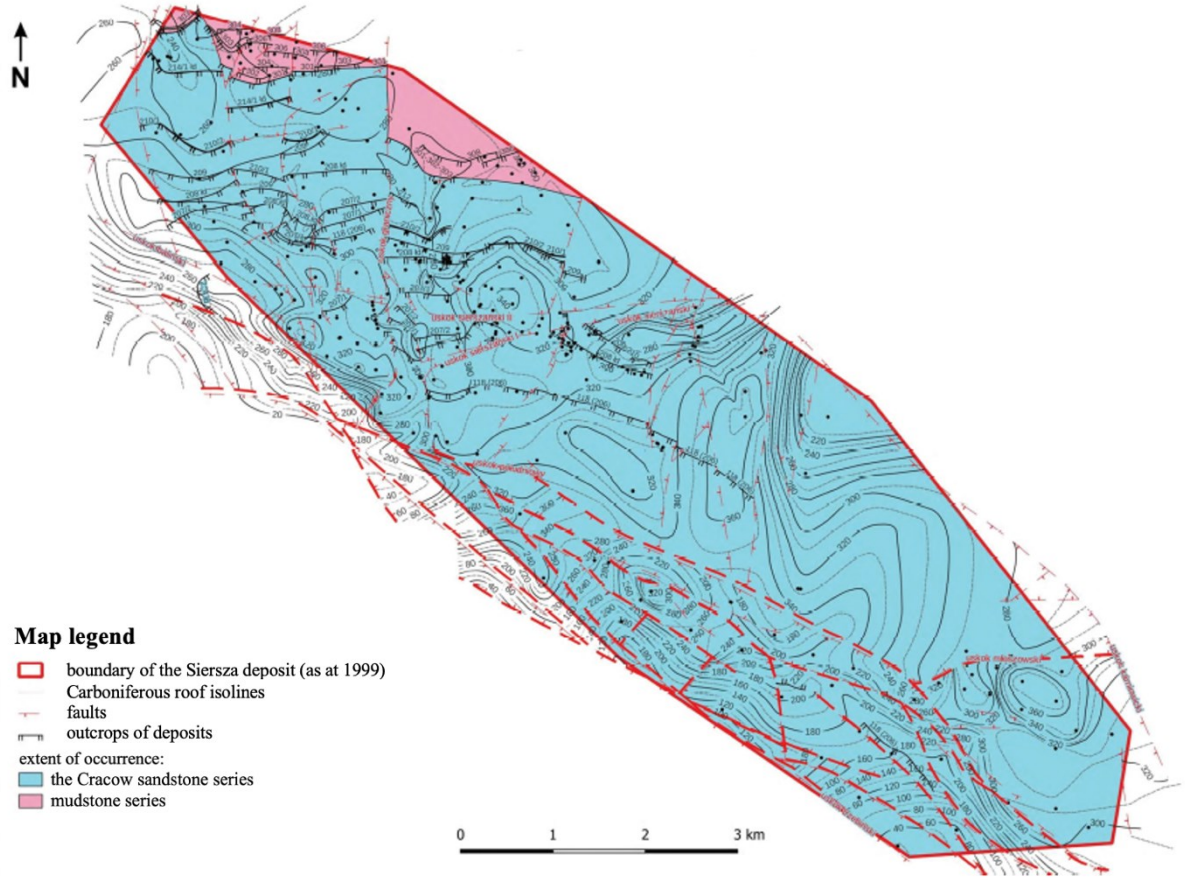

Figure 4.6 Geological map of faults and of the Carbon roof. Source: (Report on Analytical Work on Terrain Deformations in Trzebinia, Polish Geological Institute, 2023)

4.3 Hydrogeological conditions of hard coal deposits

In the case study area, there are five hydrogeological complexes comprising permeable strata: Quaternary, Jurassic, Triassic, Permian and Carboniferous formations. The Neogene formations, due to their lithological characteristics and limited extent, act as an impermeable layer.

In general, Carboniferous formations consist of fine- to coarse-grained sandstones, mudstones, siltstones and hard coal seams. When these sediments are near the surface or are covered by a thin Quaternary layer, they become highly fractured and exposed to weathering, thus facilitating water drainage regardless of their lithological condition. At greater depths, the aquifers are associated with sandstone layers, varying in thickness from a few to several tens of metres.

The synclinal structure of the deposit created favourable conditions for aquifer recharge, especially within the sandstone packages. However, the presence of faults in these packages complicates, or even prevents, the flow of water. Despite the absence of impermeable layers

(with the exception of the Neogene formations) and the limited thickness of the overburden, rainwater infiltration reached a rate of 12.5 m3/min. It is important to highlight that the discharged water did not pose a specific threat to mining operations.

As a natural consequence of the shutdown of the dewatering pumps, a gradual self-flooding of the underground mining environment occurred. However, it was observed that mining operations had a dewatering effect on the aquifers of the hard coal formations, creating a cone of depression. This observation was validated through measurements of water levels in boreholes and piezometers in several shafts (Report on Analytical Work on Terrain Deformations in Trzebinia, Polish Geological Institute, 2023).

Figure 4.7 is useful to understand the hydrogeological section of Siersza mine, with a focus on Siersza, Trzebionka, and Matylda mines.

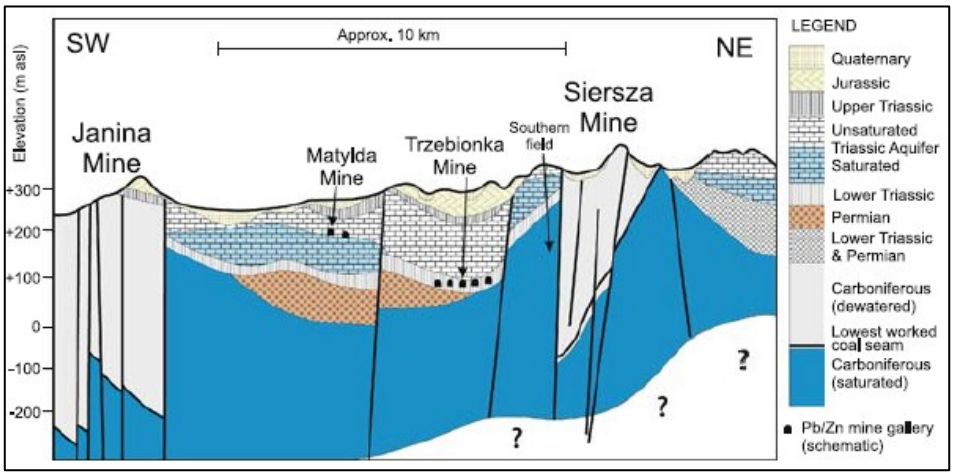

Figure 4.7 Hydrogeological cross section of Siersza mine. Source: (Banks et al., 2010)

4.4 Exploitation of hard coal deposits

The Siersza ore deposit was mainly exploited for hard coal seams within the Łaziska Formations, including seams 206, 207/1, 208, 209, 210, 210/2, 209-210 and 214. Moreover, lodes 301 and 303 in the upper part of the Orzeskie Formations were also mined (Figure 4.8).

In the northern part of the deposit, hard coal seams were found up to 100 m below the coal cover. In the eastern part, hard coal seams were found at depths ranging from tens to 200 m. In the western and central part, hard coal seams were discovered at depths ranging from a few to several tens of metres. Mining at depths of 80 or 100 m is considered shallow, and the main seams involved were 206, 207/1, 208, followed by 209, 210, 214 and 301, with progressively lesser extent. The total area of shallow mining covered a surface of 2.92 km^2 and was concentrated in the central part of the deposit (Figure 4.8).

The hard coal seams were typically mined using the chamber and pillar method, with different extraction heights: 5.4 m for seam 207, between 3.0 and 6.5 m for seam 208, and between 3.3 and 7.1 m for seam 209-210. Unfortunately, no precise data on these heights are currently available.

Ground surface deformation is closely linked to mining operations. Underground mining activities induce subsidence of the ground surface, resulting in permanent rock and soil changes and the redirection of groundwater to active working areas. This process contributes to a significant subsidence of the soil. The long-term impact of mining activities on the topography of the Siersza mine environment has led to a subsidence of almost 10 m over 200 years. However, it is important to highlight that this value is not about the entire area, since areas with protective pillars have experienced a cumulative subsidence of between 1 and 2 m.

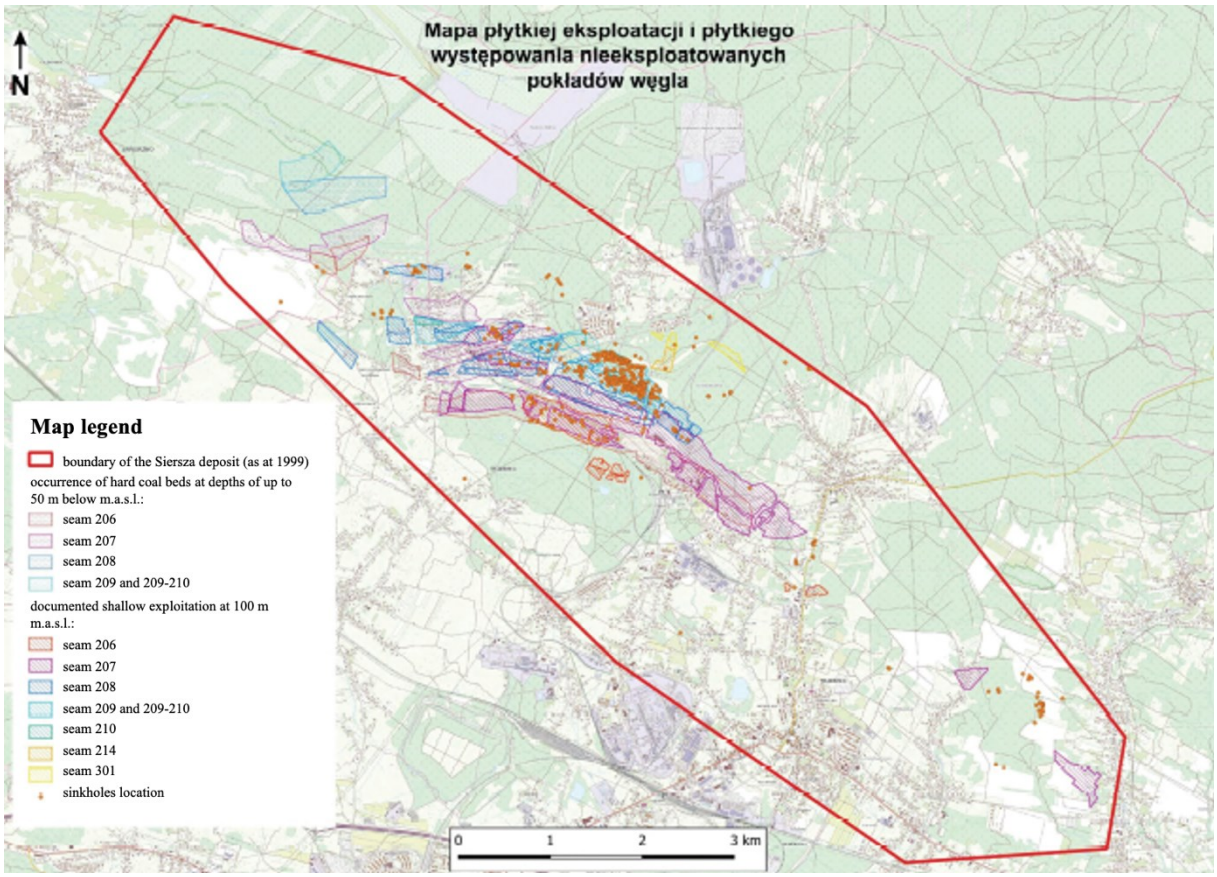

Figure 4.8 Map representing areas of shallow mining. Source: (Report on Analytical Work on Terrain Deformations in Trzebinia, Polish Geological Institute, 2023)

4.5 Sinkholes occurrence in Siersza mine area

Most of the sinkholes that occurred in the Siersza mine area are gathered in shallow mining regions. According to the Report on the Analysis of Ground Deformation in Trzebinia (2023),

a total of 527 sinkholes has been documented in the Siersza mine influence area. Out of these ones, 453 (or 86 per cent) are directly related to the shallow mining activities documented in strands 206, 207, 208, 209-210, 214 and 301, up to a depth of 100 m (Figure 4.9).

The remaining 14 per cent of the total sinkholes are distributed as follows: 10 per cent are located in areas where hard coal mining took place at greater depths, while the last 4 per cent lie outside the area of documented coal mining.

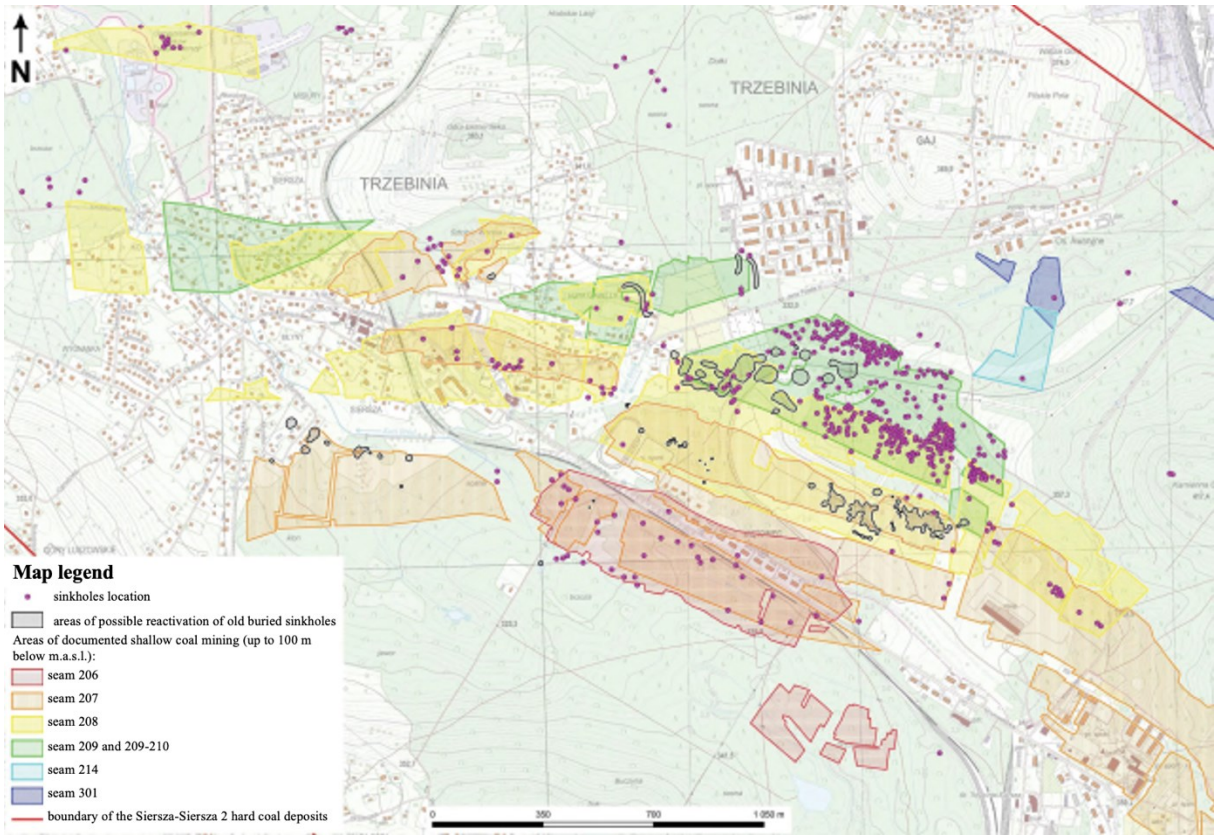

Figure 4.9 Area of highest concentration of sinkholes. Source: (Report on Analytical Work on Terrain Deformations in Trzebinia, Polish Geological Institute, 2023)

Analysing the relationship between sinkholes and the exploitation of the mining system is crucial to prevent future occurrences. As already mentioned, wooden pillars were created to facilitate the exploitation of the mine. Over time, the degradation of these pillars leads to the collapse of the mining chamber. It is interesting to highlight that no sinkholes were recorder in those areas where the cambers were filled up. Figures 4.10 and 4.11 illustrate the distribution of the maximum diameters and depths of the sinkholes recorded in the database system. Out of these ones, 447 do not exceed 20 m in diameter and 368 do not exceed 3 m in depth. These

figures provide valuable insights into the characteristics of the sinkholes observed in the Siersza mine area.

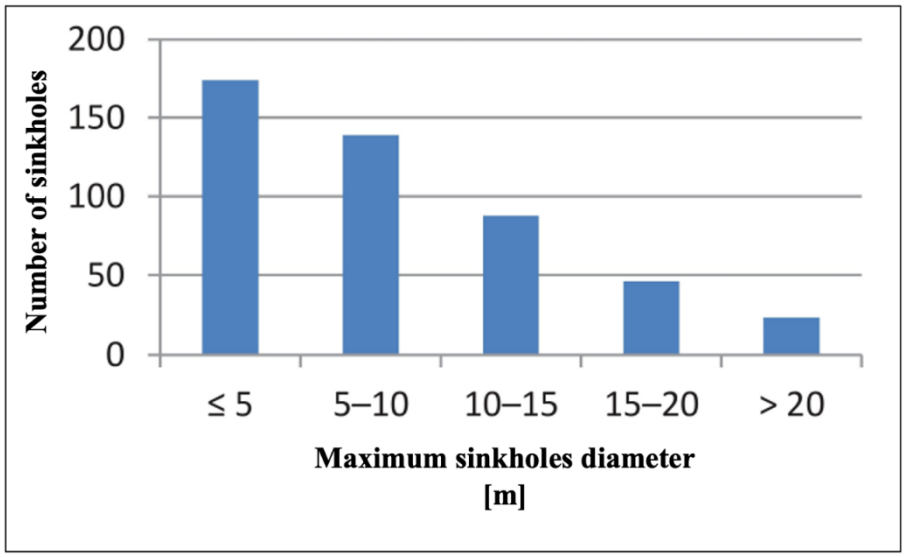

Figure 4.10 Distribution of maximum diameters of sinkholes. Source: (Report on Analytical Work on Terrain Deformations in Trzebinia, Polish Geological Institute, 2023)

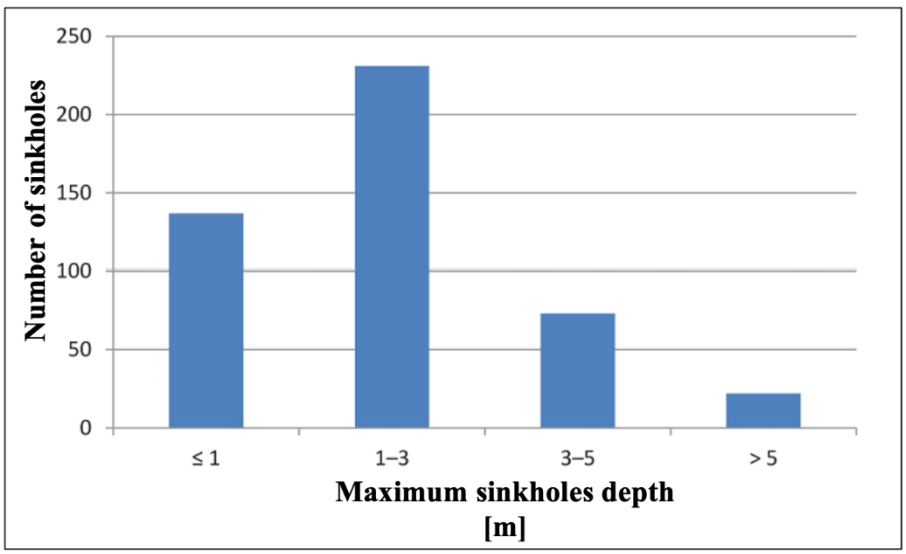

Figure 4.11 Distribution of maximum depths of sinkholes. Source: (Report on Analytical Work on Terrain Deformations in Trzebinia, Polish Geological Institute, 2023)

Chapter 5

Methodology

5.1 Poroelasticity theory

Poroelasticity is the field of materials science and mechanics that studies the interaction between fluid flow and solids deformation within a linear porous medium combining elasticity and porous medium flow. The two physics are coupled, as the deformation of the medium influences the flow and the pore pressure acts as a load on the soil skeleton. The theory was proposed by Biot (1941).

Soil can be considered as a porous medium, which is a material consisting of a solid granular matrix immersed in a fluid. The fundamental concept of poroelasticity is to study a particulate medium as the superposition of two continua: a solid continuum, governed by solid mechanics, and a fluid continuum, ruled by fluid dynamics. The distribution of the stress state between the two components is obtained applying Terzaghi's Principle:

$$\boldsymbol{\sigma}' = \boldsymbol{\sigma} - \alpha \boldsymbol{i} p \tag{5. 1}$$

where:

- $\boldsymbol{\sigma}' = \left[\sigma'_x, \sigma'_y, \sigma'_z, \tau'_{xy}, \tau'_{yz}, \tau'_{xz}\right]^T$ is the vectorial form of the total stress tensor;
- $\boldsymbol{\sigma} = \left[\sigma_x, \sigma_y, \sigma_z, \tau_{xy}, \tau_{yz}, \tau_{xz}\right]^T$ is the vectorial form of the effective stress tensor;
- $\alpha = 1 - \frac{Cr}{Cb}$ is Biot's coefficient, where C_r is the volumetric compressibility of grains and C_b is the bulk modulus;
- p is the pore fluid pressure;
- $\boldsymbol{i} = [1,1,1,0,0,0]^T$ is the vectorial form of the Kronecker delta.

Moreover:

- σ are the normal stresses, with the index indicating the direction along which they develop;

- τ are the shear stresses, with the first index indicating the direction normal to the plane containing them and the second one indicating the direction along which they develop.

The goal of the analysis is to determine the changes in the medium in terms of displacements, strains and stresses. This corresponds to identify the components of the displacement vector $\boldsymbol{u}$ and the two tensors of strain $\boldsymbol{\varepsilon}$ and stress $\boldsymbol{\sigma}$:

$$\boldsymbol{u} = \begin{bmatrix} u \\ v \\ w \end{bmatrix} \qquad \boldsymbol{\varepsilon} = \frac{1}{2}\left(\nabla \boldsymbol{u} + \nabla \boldsymbol{u}^T\right) = \begin{bmatrix} \varepsilon_x & \gamma_{yx} & \gamma_{zx} \\ \gamma_{xy} & \varepsilon_y & \gamma_{zy} \\ \gamma_{xz} & \gamma_{yz} & \varepsilon_z \end{bmatrix} \qquad \boldsymbol{\sigma} = \begin{bmatrix} \sigma_x & \tau_{yx} & \tau_{zx} \\ \tau_{xy} & \sigma_y & \tau_{zy} \\ \tau_{xz} & \tau_{yx} & \sigma_z \end{bmatrix}$$

(5. 2)

We highlight that only 6 components of the stress tensor have to be considered, since the conservation of angular momentum gives us:

$$\tau_{xy} = \tau_{yx} \qquad \tau_{xz} = \tau_{zx} \qquad \tau_{yz} = \tau_{zy}$$

(5. 3)

This is also true for the strain tensor, which can be written as:

$$\boldsymbol{\varepsilon} = \left[\varepsilon_x, \varepsilon_y, \varepsilon_z, \gamma_{xy}, \gamma_{xz}, \gamma_{yz}\right]^T$$

(5. 4)

Poroelasticity theory uses a mathematical approach to describe the soil behaviour. However, it needs some assumptions to reach a simplified but appropriate solution. The hypothesis are:

- the soil has a linear elastic behaviour, described through Hooke's law;
- only small displacements and small strains can occur;
- the strain develops in the porous matrix and the single grains are considered incompressible;
- the deformation of the porous matrix depends only on the variations of the effective intergranular stress, as stated by Terzaghi's principle.

For an elastic material the stress is a function of the strain only.
Moreover:

- the displacements and strains are independent of the history of loading;
- when the applied loads are removed, the body returns to the original relaxed state.

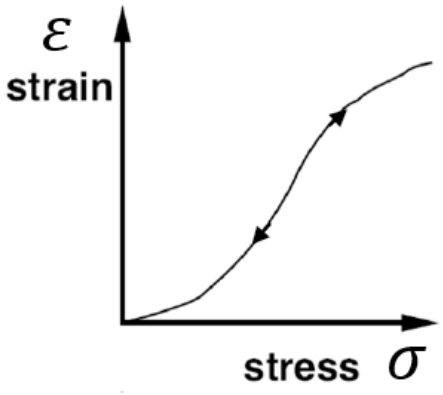

Figure 5.1 Stress-strain relation for an elastic medium

For an elastic medium the tensors of stress and strain can be studied through Hooke's law, which reads:

$$\boldsymbol{\sigma} = H\,\boldsymbol{\varepsilon} \tag{5. 5}$$

Where H is the constitutive matrix, with 21 independent constants (Carpinteri, 1995).
By assuming an isotropic behaviour of the soil (the mechanical properties are orientation-independent) it is possible to describe the previous relationship with just two independent constants. Hence, Equation (5.5) can be replaced by:

$$\boldsymbol{\sigma} = D\,\boldsymbol{\varepsilon} \tag{5. 6}$$

where D is the constitutive matrix for an isotropic elastic medium, and corresponds to:

$$D = \frac{E\,(1+\nu)}{(1+\nu)(1-2\nu)}\begin{bmatrix} 1 & \frac{\nu}{1-\nu} & \frac{\nu}{1-\nu} & 0 & 0 & 0 \\ \frac{\nu}{1-\nu} & 1 & \frac{\nu}{1-\nu} & 0 & 0 & 0 \\ \frac{\nu}{1-\nu} & \frac{\nu}{1-\nu} & 1 & 0 & 0 & 0 \\ 0 & 0 & 0 & \frac{1-2\nu}{2(1-\nu)} & 0 & 0 \\ 0 & 0 & 0 & 0 & \frac{1-2\nu}{2(1-\nu)} & 0 \\ 0 & 0 & 0 & 0 & 0 & \frac{1-2\nu}{2(1-\nu)} \end{bmatrix}$$

(5. 7)

in which, the 2 independent constants are the Young modulus E and the Poisson coefficient ν which will be introduced in chapter 6.1.2.

If we consider the relative changes to an initial undisturbed state of equilibrium, the Cauchy equations of equilibrium are cast in terms of incremental total stress and read:

$$\begin{aligned} \frac{\partial \sigma'_x}{\partial x} + \frac{\partial \tau'_{xy}}{\partial y} + \frac{\partial \tau'_{xz}}{\partial z} &= 0 \\ \frac{\partial \tau'_{yx}}{\partial x} + \frac{\partial \sigma'_y}{\partial y} + \frac{\partial \tau'_{zy}}{\partial z} &= 0 \\ \frac{\partial \tau'_{zx}}{\partial x} + \frac{\partial \tau'_{zy}}{\partial y} + \frac{\partial \sigma'_z}{\partial z} &= 0 \end{aligned}$$

(5. 8)

By inserting in Equation (5.8) Terzaghi's principle (5.1), a new set of equations, expressed in terms of effective stresses and pressure, is obtained:

$$\begin{aligned} \frac{\partial \sigma_x}{\partial x} + \frac{\partial \tau_{xy}}{\partial y} + \frac{\partial \tau_{xz}}{\partial z} &= \frac{\partial p}{\partial x} \\ \frac{\partial \tau_{yx}}{\partial x} + \frac{\partial \sigma_y}{\partial y} + \frac{\partial \tau_{yz}}{\partial z} &= \frac{\partial p}{\partial y} \\ \frac{\partial \tau_{zx}}{\partial x} + \frac{\partial \tau_{zy}}{\partial y} + \frac{\partial \sigma_z}{\partial z} &= \frac{\partial p}{\partial z} \end{aligned}$$

(5. 9)

The strain tensor $\boldsymbol{\varepsilon}$ can be expressed as:

$$\boldsymbol{\varepsilon} = L\boldsymbol{u} \tag{5.10}$$

where L is the first order differential operator collecting the compatibility conditions. Finally, we can write the incremental form of the constitutive law, linking effective stress $\boldsymbol{\sigma}$ and strain:

$$d\boldsymbol{\sigma} = D_t d\boldsymbol{\varepsilon} \tag{5.11}$$

in which D_t is the tangent constitutive matrix.

In order to solve the problem, proper boundary conditions are required.

In general, two types of boundary conditions are used:

- Dirichlet conditions: defined on the unknown function u;
- Neumann conditions: defined on the derivative of the unknown function $\frac{\partial u}{\partial n}$, with n the normal direction to the boundary;

In this thesis, only Dirichlet and Neumann conditions are considered. In particular Dirichlet conditions represent imposed displacements while Neumann conditions represent applied forces.

5.2 Weak formulation

The solution of a partial derivative equation of order k is called strong solution if it is a differentiable function up to the k-th order and all derivatives exist and are continuous. If a non-differentiable function is admitted as a solution to a well-posed problem, is known as weak solution, also known as a "generalised solution". The main problem of finding the displacements $\boldsymbol{u}$ which are in equilibrium with a given set of external forces can be solved using the virtual work principle:

$$\delta W_i - \delta W_e = 0 \tag{5. 12}$$

where δW_i and δW_e are the internal and external virtual works, respectively.

The principle of virtual work is the fundamental identity in the field of mechanics of deformable bodies. It states the equality between external virtual work and internal virtual work (Carpinteri,

1995) and is valid in systems of forces that satisfy the Cauchy Equations (5.8). Therefore, by taking into consideration a 3-dimensional body Ω having an external boundary $\partial\Omega$ and subject to a set of body forces $\boldsymbol{b}$ and surface traction $\boldsymbol{t}$, is possible to write δW_i as:

$$\delta W_i = \int_{\Omega} \delta \boldsymbol{\varepsilon}^T \boldsymbol{\sigma}' \, dV \tag{5. 13}$$

where $\boldsymbol{\varepsilon}$ is the strain vector presented in Equation (5.4) and $\boldsymbol{\sigma}'$ is the total stress vector of Equation (5.1). The result of using Terzaghi's principle in Equation (5.13) is:

$$\delta W_i = \int_{\Omega} \delta \boldsymbol{\varepsilon}^T \boldsymbol{\sigma} \, dV - \int_{\Omega} \delta \boldsymbol{\varepsilon}^T \boldsymbol{i} \alpha p \, dV \tag{5. 14}$$

Moreover, δW_e can be written as:

$$\delta W_e = \int_{\Omega} \delta \boldsymbol{u}^T \boldsymbol{b} \, dV + \int_{\partial\Omega} \delta \boldsymbol{u}^T \boldsymbol{t} \, dS \tag{5. 15}$$

Hence, the final expression of Equation (5.12) result as follows:

$$\int_{\Omega} \delta \boldsymbol{\varepsilon}^T \boldsymbol{\sigma} \, dV = \int_{\Omega} \delta \boldsymbol{\varepsilon}^T \boldsymbol{i} \alpha p \, dV + \int_{\Omega} \delta \boldsymbol{u}^T \boldsymbol{b} \, dV + \int_{\partial\Omega} \delta \boldsymbol{u}^T \boldsymbol{t} \, dS \tag{5. 16}$$

Numerical simulations can be studied through a coupled or uncoupled approach. In this thesis we elected to use the uncoupled approach, named one-way coupling, and it is applied following these steps:

1. The pressure field is calculated through the flow model. The flow simulator solves the mass balance equation:

$$\frac{\partial}{\partial x}\left(K_x \frac{\partial p}{\partial x}\right) + \frac{\partial}{\partial y}\left(K_y \frac{\partial p}{\partial y}\right) + \frac{\partial}{\partial z}\left(K_z \frac{\partial p}{\partial z}\right) = S_s \frac{\partial p}{\partial t}$$

(5. 17)

where S_s is the specific elastic storage;

2. The flow model output is used as input for the geomechanical model;
3. Computation of the displacement fields (and, among them, land subsidence and horizontal displacement) through the geomechanical model. It solves this non-linear system of equations:

$$\begin{cases} \nabla \boldsymbol{\sigma} + \boldsymbol{f} = 0 \\ d\boldsymbol{\sigma} = D_t d\boldsymbol{\varepsilon} \\ \boldsymbol{\varepsilon} = L\boldsymbol{u} \end{cases}$$

(5.18)

5.3 The Finite Element method

On of the available numerical tools to approximatively solve a partial differential equation is the finite element method. Among others, we remind the finite difference method, the finite volume method and so on. Numerical approximations are required since analytical solutions is known only for extremely simple combinations of domain and boundary conditions and are useless in practical applications. In this thesis, we want to solve the linear momentum balance applying the finite element method. This is a numerical method that subdivides the domain into smaller and simpler sub-domains, called, indeed, finite elements. The response of each element is expressed in terms of a finite number of degrees of freedom characterizing an unknown function at a set of *N* nodal points (Fletcher, 2023). By doing so, we can move from the original unknowns, which are functions, to the model unknowns, which are nodal values, as the interpolation functions are a priori known (Franceschini, 2014).

Therefore, the problem can be expressed as a non-linear system of equations in the form of $\boldsymbol{r}(\boldsymbol{u}) = 0$, where $J = \partial \boldsymbol{r} / \partial \boldsymbol{u}$ is the Jacobian matrix, i.e., the discretized version of the differential operator, $\boldsymbol{u}$ is the vector of unknowns (nodal displacements).

In this case study, linear tetrahedral finite elements are adopted (Figure 5.3).

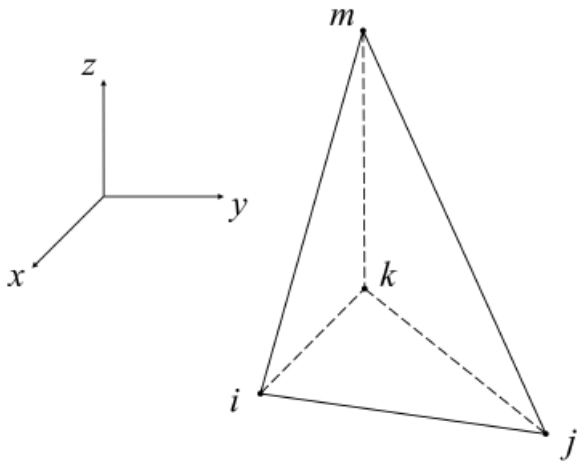

Figure 5.2 Tetrahedral finite element

ξ_i represent the shape function (Gambolati & Ferronato, 2015):

$$\xi_i = \frac{a_i + b_i x + c_i y + d_i z}{6V^e} \tag{5. 19}$$

in which the coefficients $a_i, b_i, c_i,$ and d_i are (Gambolati & Ferronato, 2015):

$$a_i = det\begin{bmatrix} x_j & y_j & z_j \\ x_k & y_k & x_k \\ x_m & y_m & z_m \end{bmatrix} \qquad b_i = -det\begin{bmatrix} 1 & y_j & z_j \\ 1 & y_k & x_k \\ 1 & y_m & z_m \end{bmatrix}$$

$$c_i = det\begin{bmatrix} 1 & x_j & z_j \\ 1 & x_k & z_k \\ 1 & x_m & z_m \end{bmatrix} \qquad d_i = -det\begin{bmatrix} 1 & x_j & y_j \\ 1 & x_k & y_k \\ 1 & x_m & y_m \end{bmatrix} \tag{5. 20}$$

The solution to the problem can be therefore expressed using the displacements as unknowns. Thanks to the introduction of the finite element basis function, the displacement can be expressed in as:

$$u = [N_1 \quad N_2 \quad N_3 \quad N_4]\begin{bmatrix} u_1 \\ u_2 \\ u_3 \\ u_4 \end{bmatrix} \tag{5. 21}$$

where N_i is equal to the shape function ξ_i multiplied by the identity matrix I, and the displacements u_i are vectors made of three components u_x, u_y, and u_z.

5.4 The Knothe-Budryk theory: an analytical modelling perspective

In this section, the Knothe-Budryk theory, one of the most frequently applied analytical models for prediction of ground deformation associated to mining, is presented. This model was developed in the '50s in Poland and was implemented into several applications for different types of mining activities, such as hard coal mining, copper ore mining, and salt mining (Malinowska et al., 2020). This method was successfully implemented in Europe (i.e., Germany, Czech Republic, and Spain), the United States, Australia and Asia (i.e., China, Vietnam, and Thailand) (Misa, 2023).

The Knothe-Budryk theory is based on the assumption of elementary influences. This means that removing an elementary element from the rock mass with a volume dV causes a proportional elementary increase in land subsidence dS_A at point A. The cause and effect of the process are linked by a relationship in which the proportionality coefficient is the influence function. This function is known as the surface of influence $f(x, y)$ and can be expressed using Equation (5.22):

$$dS_A = f(x, y) \cdot dV \tag{5.22}$$

where x and y are the Cartesian coordinates.

In the case of mining a deposit with a thickness T the elementary volume dV of a deposit is defined by Equation (5.23):

$$dV = dx \cdot dy \cdot dz = dx \cdot dy \cdot (a \cdot T) \tag{5.23}$$

where a is the parameter indicating the degree of filling of the post-mining void, ranging between 0 and 1 (in this case study is equal to 0.42), and z is the Cartesian coordinate.

Hence, Equation (5.22) can be written as:

$$dS_A = (a \cdot T) \cdot f(x, y) dx dy \tag{5.24}$$

To calculate the total impact of land deformation, every elementary influence must be summed up using linear superpositions (Equation 5.25).

$$S_A = (a \cdot T) \cdot \iint_P f(x,y)dxdy \tag{5.25}$$

According to the Knothe-Budryk model, Equation (5.25) is the most general formula for calculating land subsidence at any point on the terrain surface.

The influence function $f(x,y)$ in Equation (5.25) is generally substituted by a normal gaussian distribution:

$$f(x) = \frac{h}{\sqrt{\pi}} \exp(-h^2 \cdot x) \tag{5.26}$$

where h is the parameter of the normal Gaussian distribution function.

In the Knothe-Budryk theory, h is replaced by the radius of influence R, that corresponds to:

$$R = \frac{Z}{\tan \beta} \tag{5.27}$$

where Z is the depth of mining exploitation, and β is the rock mass parameter that depends on the structural and geomechanical conditions of the rock mass. The value of $\tan \beta$ ranges between 1 and 3 (Guzy & Witkowski, 2021).

The results of this analytical model are discussed in the following chapter.

5.5 Tools and software overview

The use of a three-dimensional geomechanical model for the simulation of a real case study involves a versatile approach that includes the collection, in-depth analysis, interpretation, and adaptation of all relevant acquired data. This process is facilitated by using specialised tools and software, which allow for accurate implementation of geological and mechanical parameters:

- QGIS (Quantum GIS), a free and open-source geographic information system software that allows users to view, edit, and analyse geospatial data by representing them on interactive maps. The software offers many resources and maps. Finally, there is a variety of plug-ins to accomplish specific tasks, and there are always new plug-ins being created (QGIS: An Introduction to an Open-Source Geographic Information System | Mississippi State University Extension Service);
- Surfer is a three-dimensional mapping software, developed by Golden Software, used to visualise scientific data as maps, graphs and three-dimensional models. This software allows to create maps to represent the spatial distribution of data on a plane, and it provides the user with mathematical tools for the analysis and manipulation of data;
- Gmsh is an open-source three-dimension finite element mesh generator with an integrated CAD engine and post-processor (Geuzaine & Remacle, 2009). This software allows to create two-dimensional and three-dimensional meshes, crucial parts for the aim of this research;
- VisIt is an open-source visualisation tool, dedicated to graphical analysis, offering a comprehensive platform for examining scientific data. This versatile tool can work with structured and unstructured two-dimensional or three-dimensional meshes. Its use has been fundamental for the visual analysis of the model outputs, as final step in this work.

All this software is used to develop the input files for GEPS3D (Geomechanical Elasto-Plastic Simulator 3D) and visualize the simulator outcomes. GEPS3D is a 3D visco-elasto-plastic geomechanical simulator developed by Dept. ICEA (Isotton et al., 2019; Spiezia et al., 2017) and used to simulate displacement and stress fields of the subsurface systems due to anthropogenic activities (Gambolati et al., 1986; Ochoa-González et al., 2018; Teatini et al., 2011; Ye et al., 2018; Zhu et al., 2020). Based on FEs and IEs, the code simulates the possible activation of pre-existing faults with a quasi-static approach. The discontinuity surfaces are modelled according to the principles of contact mechanics as inner boundaries embedded in the continuous body. The fault activation produces a relative displacement between opposite points whenever the stress state violates the Mohr-Coulomb failure criterion. An accurate, stable and efficient numerical algorithm to account for the fault activation is guaranteed by the approach developed by the proponent research team making use of Lagrange multipliers (Franceschini et al., 2020, 2022). The employment of an advanced solver library, fully developed and implemented by the Dept. ICEA, allows for an efficient GEPS3D use on parallel super-computers for the simulation of problems with tens of million unknowns.

Chapter 6

Modelling approach

6.1 Input data

6.1.1 Geological and geographic data

After the Second World War, the Polish Geological Institute-National Research Institute conducted several geological research in mining areas. During the ‘50s and the ‘60s (Guzy & Witkowski, 2021) hundreds of boreholes were drilled in the Siersza mine area to collect information about the geological structure. For this research, 163 boreholes have been analysed in the study area (Figure 6.1).

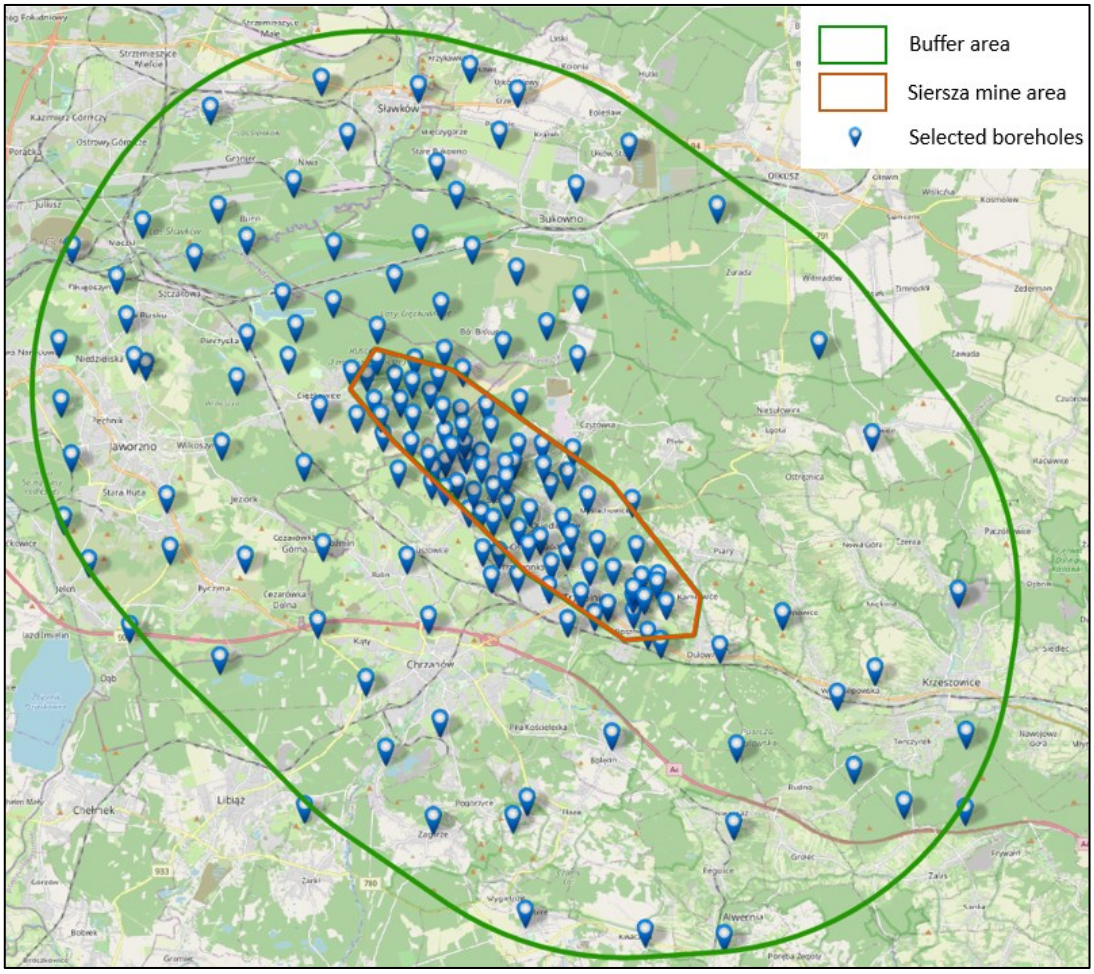

Figure 6.1 Selected boreholes in the study area.

The selection of borehole locations aims to obtain a complete view of the outer region, encompassing most of the Siersza region, with a specific focus on the area above the shallow mining exploitation.

The information on boreholes collected from the web portal of the Polish Geological Institute are name and identification number of the borehole, geographical coordinates according to the PL-1992 reference system, elevation of the land surface at the well location, depth and thickness of each geological layer crossed by the borehole. Different thicknesses of the overburden correspond to different depths of the wells. Approximately, 60 % of the wells is between 10 and 100 m deep, while the remaining 40 % extends to depths of thousands of meters, reaching the maximum value of 1,250 m.

Finally, the elevation of all boreholes has been compared with the one of the DTM (Digital Terrain Model), downloaded by the Polish Geological Institute website, to assess their accuracy. Some discrepancies, on the order of 20.00 m have been detected. However, such a difference is due to the presence of outliers. Without them, this discrepancy decreases to 1.8 meters.

The geological layers range from Quaternary to Permian deposits (Table 2).

6.1.2 Geomechanical data

Soil density plays a fundamental role in the geomechanical modelling since it is required to compute the geostatic stress acting at various depths. For this thesis, the bulk density values have been derived from the literature (Wilk et al., 2003)., The collected data are provided in Table 2.

Due to the quite small thickness of the main five macro-geological layers, we adopt the average value of the density to perform further computations. Regarding the carboniferous layer, which is the deepest of the considered stratigraphic layering, its densities are averaged since sandstone, siltstone, and conglomerate are well homogenized through. In the sub-layers in which mines are located, only the averaged density of the hard coal is assigned.

To characterize the density variability, also the standard deviation has been calculated for each averaged value.

Table 2 Densities of different geological layers in the study area. Source Wilk et al. (2003)

Geological layer	Rock types	Density [kg/m^3]	$\mu \pm \sigma$ [kg/m^3]
Quaternary	glacial deposits - glacial till	2000.00-2200.00	1775.00 ± 317.54
	glaciofluvial deposits - sands, gravels	1700.00-2100.00	
	fluvial deposits - sands, gravels	1500.00-2000.00	
	aeolian deposits - loess, sands	1200.00-1500.00	
Neogene	clays	1700.00-2600.00	1833.33 ± 301.39
	shale		
	sands	1400.00-1700.00	
	gravels	1600.00-2000.00	
Upper Jurassic	limestone slabs	2200.00-2600.00	2433.33 ± 57.73
	rocky limestones		
	marly limestones		
Middle Jurassic	marly limestones		
	sandstones	2200.00-2600.00	
Lower Jurassic (Lias)	kaolinitic clays	2300.00-2700.00	
Upper Triassic	series of clayey rocks with inserts of limestone and sandstone	1700.00-2600.00	2406.25 ± 304.06
Middle Triassic	dolomitic marls	2100.00-2500.00	
	marls		
	sandstone	2200.00-2600.00	
	diploporic dolomites	2800.00-2900.00	
	marly dolomites		
	crystalline limestones	2200.00-2600.00	
	wavy limestones		
Lower Triassic	dolomites	2800.00-2900.00	
	clayey marls	2100.00-2500.00	
	dolomitic marls		
	weakly consolidated sandstones, gravelstones, mudstone inserts, siltstones inserts	1800.00-2000.00	
Permian	limestone conglomerates	2200.00-2600.00	2487.50 ± 154.78
	porphyritic-limestone conglomerates	2300.00-2700.00	
	melaphyres, red porphyries	2400.00-3000.00	
	sandstone, clay	2200.00-2500.00	
Carboniferous	sandstone	2200.00-2600.00	2125.00 ± 526.78
	siltsone	2300.00-2700.00	
	conglomerate	2000.00-2500.00	
	hard coal	1200.00-1500.00	1350.00

The geomechanics parameters required to model the soil behavior are the Young modulus E and the Poisson ratio ν.

Finally, it can be observed that these parameters depend on temperature. However, this research deals with shallow depths where the temperature dependency can be safely neglected.

The geomechanical values implemented in this work are shown in Table 3.

Table 3 Geological parameters for the case study area. Source: Wilk et al. (2003)

Geological layer	**Rock types**	E **[GPa]**	**Average** E **[GPa]**	ν	**Average** ν
Quaternary	glacial deposits - glacial till	0.01	0.04	0.35	0.35
	glaciofluvial deposits - sands, gravels	0.05		0.35	
	fluvial deposits - sands, gravels	0.05		0.35	
	aeolian deposits - loess, sands	0.05		0.35	
Neogene	clays	3.30	1.75	0.20	0.20
	shale	2.90		0.20	
	sands	0.40		0.20	
	gravels	0.40		0.20	
Upper Jurassic	limestone slabs	-	4.74	0.20	0.20
	rocky limestones	4.88		0.20	
	marly limestones	-		0.20	
Middle Jurassic	marly limestones	-		0.20	
	sandstones	4.60		0.20	
Lower Jurassic (Lias)	kaolinitic clays	-		0.20	
Upper Triassic	series of clayey rocks with inserts of limestone and sandstone	-	4.84	0.20	0.20
Middle Triassic	dolomitic marls	4.40		0.20	
	marls	-		0.20	
	sandstone	5.28		0.20	
	diploporic dolomites	5.25		0.20	
	marly dolomites	5.23		0.20	
	crystalline limestones	-		0.20	
	wavy limestones	-		0.20	
Lower Triassic	dolomites	5.25		0.20	
	clayey marls	-		0.20	
	dolomitic marls	-		0.20	

	weakly consolidated sandstones, gravelstones, mudstone inserts, siltstones inserts	3.60		0.20	
Permian	limestone conglomerates	-	1.60	0.25	0.25
	porphyritic-limestone conglomerates	-		0.25	
	melaphyres, red porphyries	-		0.25	
	sandstone, clay	1.60		0.25	
Carboniferous	sandstone	3.80	2.70	0.25	0.25
	siltsone	1.60		0.25	
	conglomerate	-		0.25	
	hard coal	10.00	10.00	0.25	0.25

The data in Table 3 come from drilling inspections in the study area, unfortunately not all data are available (blank cells). As for the density, only average values are taken into account.

6.2 Mesh definition

To perform a finite element analysis, the first step involves the discretization of the study area (Figure 6.2).

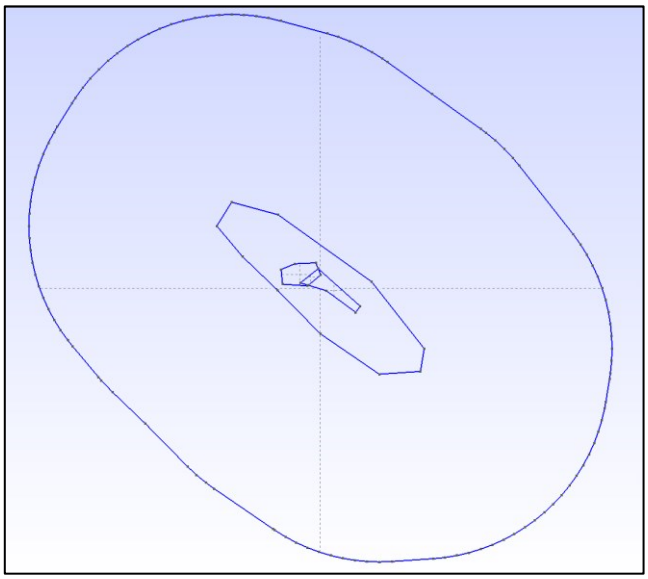

Figure 6.2 Geometry of study area in GMSH

Different mesh sizes were developed in order to reach a trade-off between the optimal mesh size, better accuracy on the shallow mining area, and the estimated computational cost. The final selection is characterized by elements with average dimension equal to 1,654 m, 80 m,

and 30 m along the outermost boundary, the Siersza mine boundary, and the shallow mining area boundary, respectively (Figure 6.3).

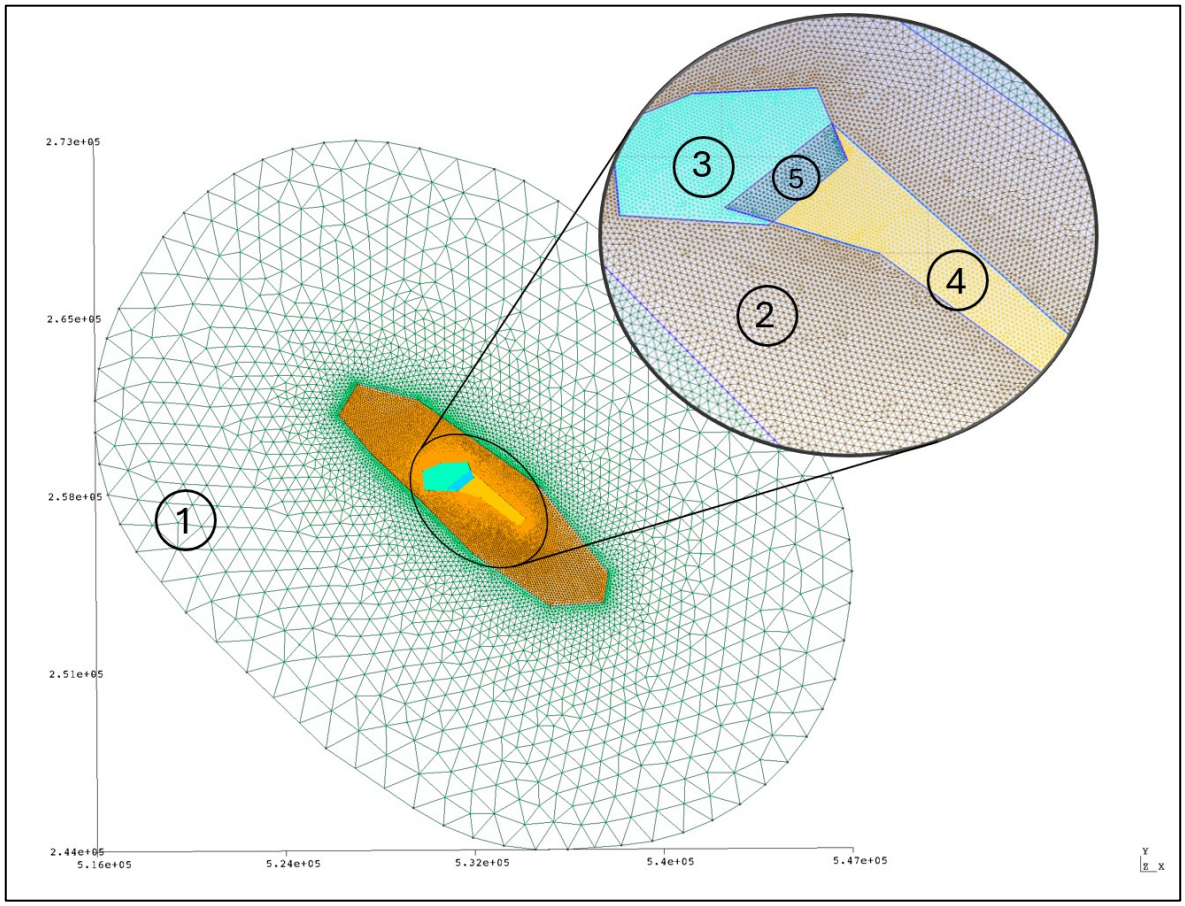

Figure 6.3 2D mesh developed to discretize the study area. The colors and numbering point out areas with different characteristics.

The 2D mesh has a total of 15,109 nodes and 30,150 triangular elements. It can be divided with five zones, highlighted by a number from 1 to 5 in Figure 6.3:

1. Siersza buffer area;
2. Siersza mining area;
3. area of shallow mining exploitation at 50 m below the terrain surface;
4. overlapping area of shallow mining exploitation;
5. area of shallow mining exploitation at 100 m below the terrain surface.

Along the vertical direction the model is characterized by the presence of 10 layers, the first five representing each of the geological layer (Quaternary, Neogene, Jurassic, Triassic, and Permian), the last five the carboniferous sub-layers:

1. layer between the bottom of Permian and the top of the mine located at 50 m below the terrain surface;
2. layer related to the thickness of the 50 m mining panel;
3. layer between the mine at 50 m and the one at 100 m below the terrain surface;
4. layer representing the 100 m-thick mining panel;
5. layer representing the remaining thickness of the carboniferous layer.

The development of the first four layers and the bottom of the carboniferous layer has been carried out by interpolating the boreholes information, applying the Kriging method. Kriging is a statistical technique using a small set of sampled data points to predict the value of a variable in a continuous spatial field. The process of Kriging involves two main steps: initially, the spatial covariance structure of the sampled points is determined by fitting a variogram; then, the weights derived from this covariance structure are applied to interpolate the values of the unsampled points throughout the spatial field. Figure 6.4 provide a visual representation of the experimental covariance computed from each pair of points in the sampled data. For each pair, the semivariogram is plotted against the distance.

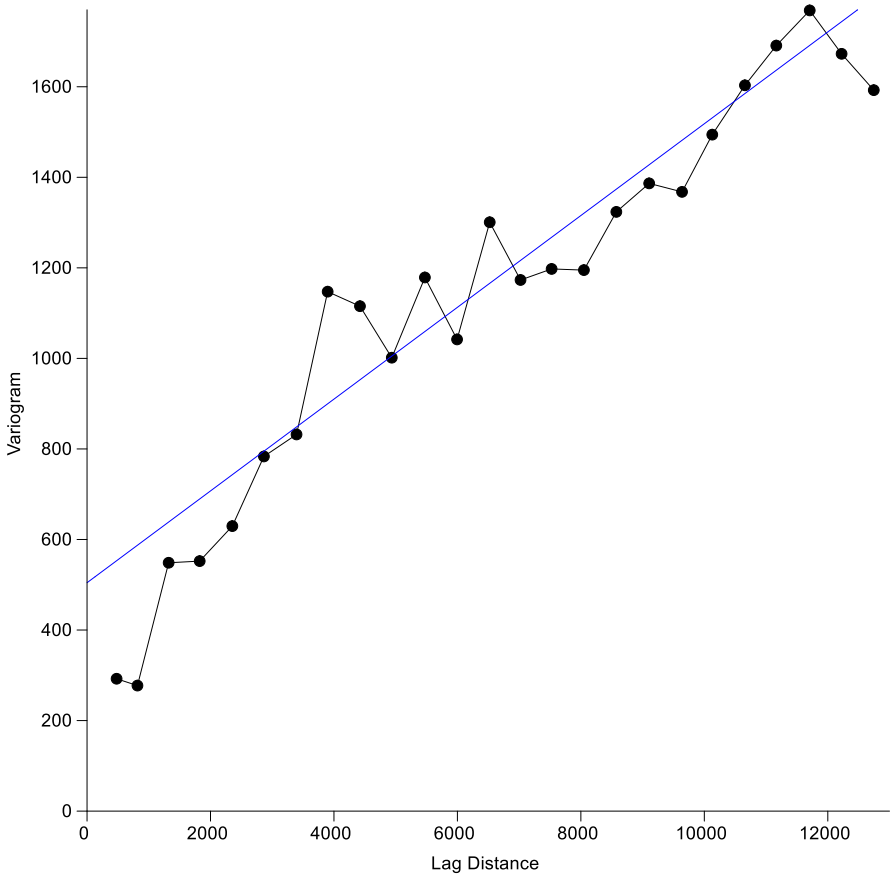

Figure 6.4 Variogram used to interpolate the Quaternary layer. Black dots refer to the experimental variogram, the blue line to the model variogram used for data interpolation.

The layering of the entire area and of the shallow mines are shown in Figure 6.5 and Figure 6.6, respectively. The trace of the sections is provided in Figure 4.2.

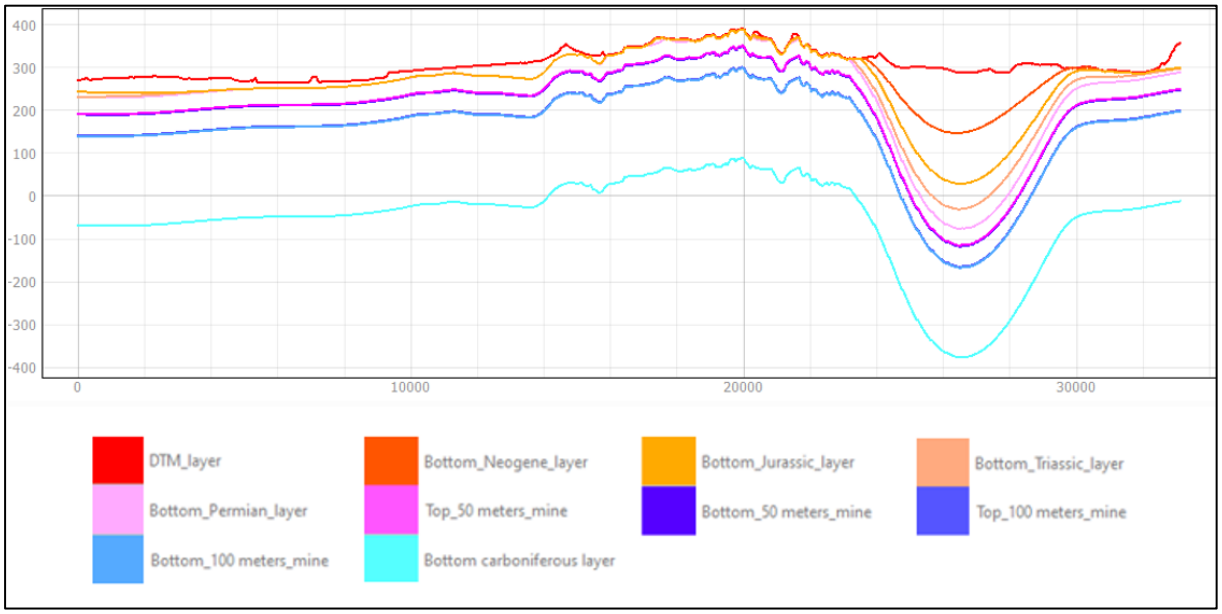

Figure 6.5 Layering of the entire study area along section A-A'

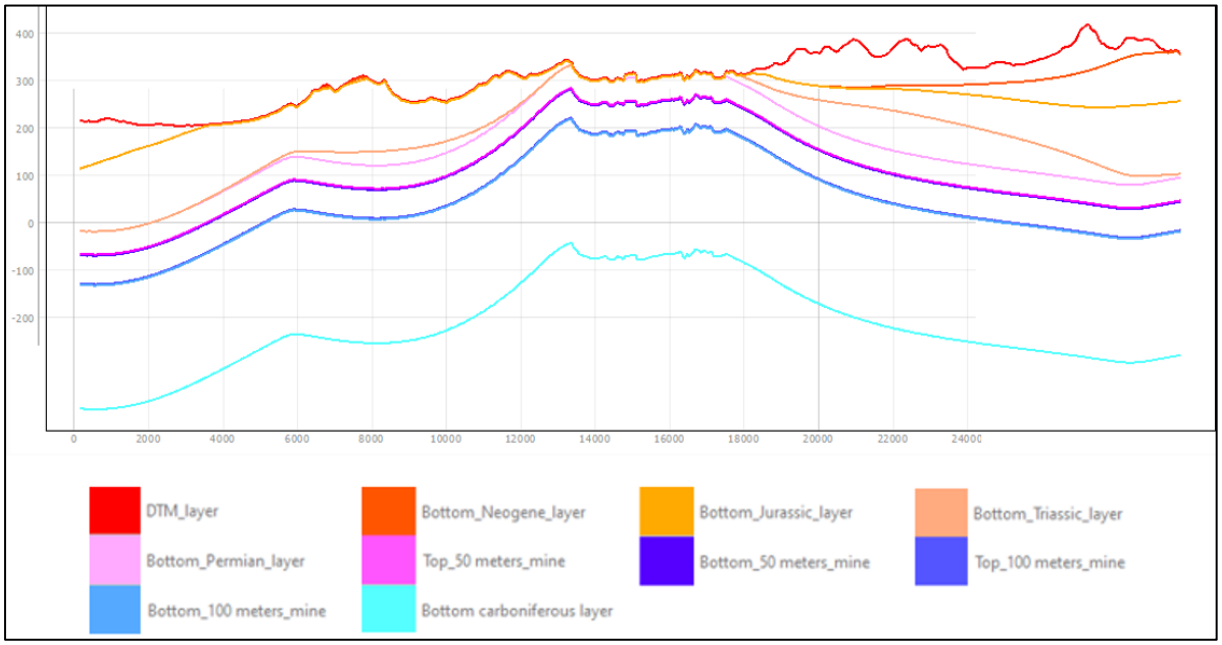

Figure 6.6 Layering of the entire study area along section B-B'

In order to build a useful model, a trade-off between computational time and model reliability is needed. The assumptions are about the presence of faults in the case study area (Figure 4.3) and the mine layers geometry. In this first evaluation, faults are not explicitly implemented in the model but, instead, they are incorporated in the carboniferous layer. In such a way, the steps

due to the faults are still present in the model, but there is no need to deal with the discontinuous mechanics., saving computational time.

The second assumption regards the elevation of the roof and the bottom of the mines corresponding to layer seven and nine. In this analysis they are represent as horizontal planes (Figure 6.7a). A specific procedure has been implemented to reproduce this set-up and, at the same time, be sure that there are no intersections between layers. Figure 6.7a shows an example of the horizontal trend of mining panels (top and bottom of 50 m mine, and 100 m mine, according to the legend).

Finally, the elevations of the mining panels are 279.72, 275.72, 254.141, and 250.141 m.a.s.l, for the top and the bottom of the shallower mine, and for the top and the bottom of the deeper mine, respectively.

The 3D mesh (Figure 6.7b) has a total of 257,033 nodes and 1,448,060 tetrahedral elements.

Moreover, a 3-dimensional detail of the zones already shown in Figure 6.3, is provided in Figure 6.8.

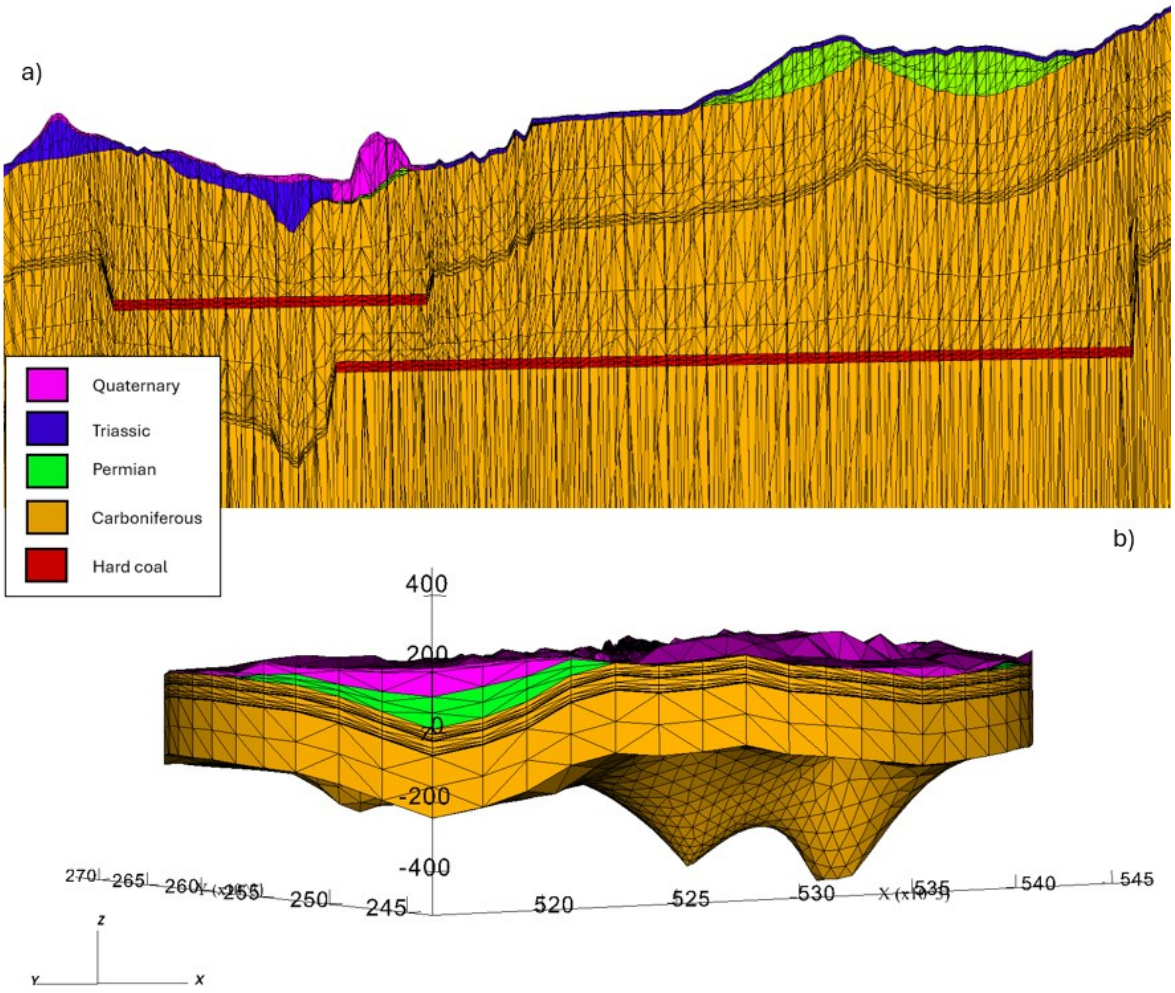

Figure 6.7 a) Section of the model in which the horizontal trend of both mines is highlighted, b) Lateral view of the 3D mesh. For visualization purposes the z axis has been scaled by 10 times.

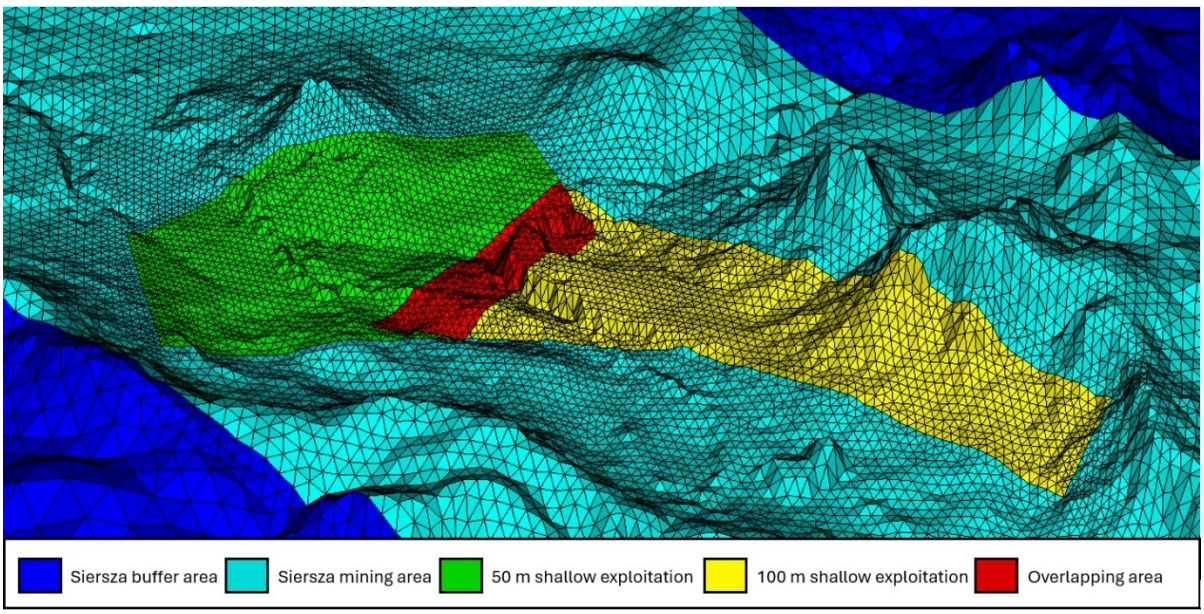

Figure 6.8 Particular of the 3D mesh of shallow mining areas

6.3 Geomechanical model

Land subsidence is caused by the geostatic stresses f that act on the roof and on the bottom of both mines no more counterbalanced by the mine soil which is removed. This stress is calculated using the following formula:

$$f = \sum f_i = \sum (\rho_i \cdot h_i \cdot g) \tag{6.5}$$

where ρ_i, and h_i are the density and the thickness of every layer above the mine, respectively, and g is the gravitational acceleration.

By considering Equation (6.5) it is easy to understand that larger depths correspond to larger geological stresses.

The forces that act on the nodes are calculated as:

$$F = f' \cdot A \tag{6.6}$$

in which F represents the nodal force, f is the geological stress, and A corresponds to the area adjacent to the node. This latter parameter is computed as a third of the sum of all the triangular areas that surround the analyzed node. An example is provided in Figure 6.9.

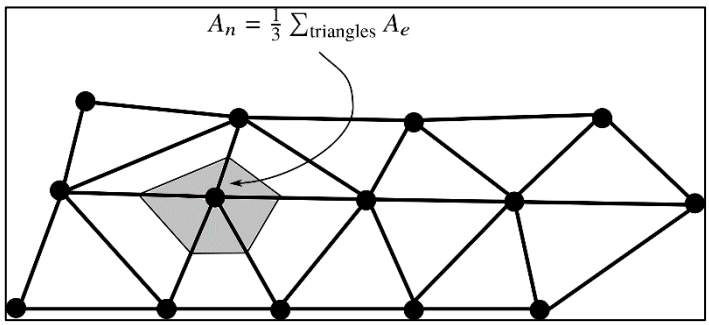

Figure 6.9 Schematization of the adjacent area of a node.

The geomechanical model is applied to simulate land displacements associated to the hard coal removal from the mining panel. The model application requires specifying appropriate boundary conditions. In this research, Dirichlet conditions are imposed on the lateral and bottom surfaces of the domain, thus considering no displacements along the three directions.

6.4 Modelling scenarios

The key parameter governing the model response is soil stiffness. Four sets of simulations have been carried out to test the model response and obtain a reliable solution, i.e. a computed displacement pattern that agree with estimate of land subsidence.

The first run is characterized by a homogeneous distribution of the geomechanical parameters, with the same Young modulus $E = 0.978\,GPa$, assigned to every layer. Then, the heterogeneous distribution of E summarized in Table 4 has been used in agreement with the available data reported in Table 3.

Finally, two final sets of scenarios was carried out by reducing the E value of the "mine material" in order to represent the extraction of hard coal from the mining panel, thus making it weaker (or less stiff). This strategy has been used as it is much simpler than removing the FEs corresponding to the excavated hard coal panels from the 3D FE mesh.

Table 4 Young modulus E assigned to each geological layer.

Geological layer	Young modulus E [GPa]
Quaternary	0.04
Neogene	1.75
Jurassic	4.74
Triassic	4.84
Permian	1.60
Carboniferous	2.70
Hard coal	10.00

In these final runs, E has been decreased from 1 to 3 orders of magnitude.

The outcomes of each of these runs are discussed in chapter 7.

6.5 Analytical results: the Knothe-Budryk model as a comparison tool

In this particular case study, the Knothe-Budryk theory has been adopted by the Faculty of Geo-Data Science, Geodesy and Environmental Engineering of AGH University of Science and Technology of Cracow, Poland, to calculate the predicted land subsidence. The results correspond to 1.68m above both mines and 3.36m above the overlapping area, as depicted in Figure 6.10. These outcomes represent a useful term for comparison for the results of GEPS3D, which will be discussed later.

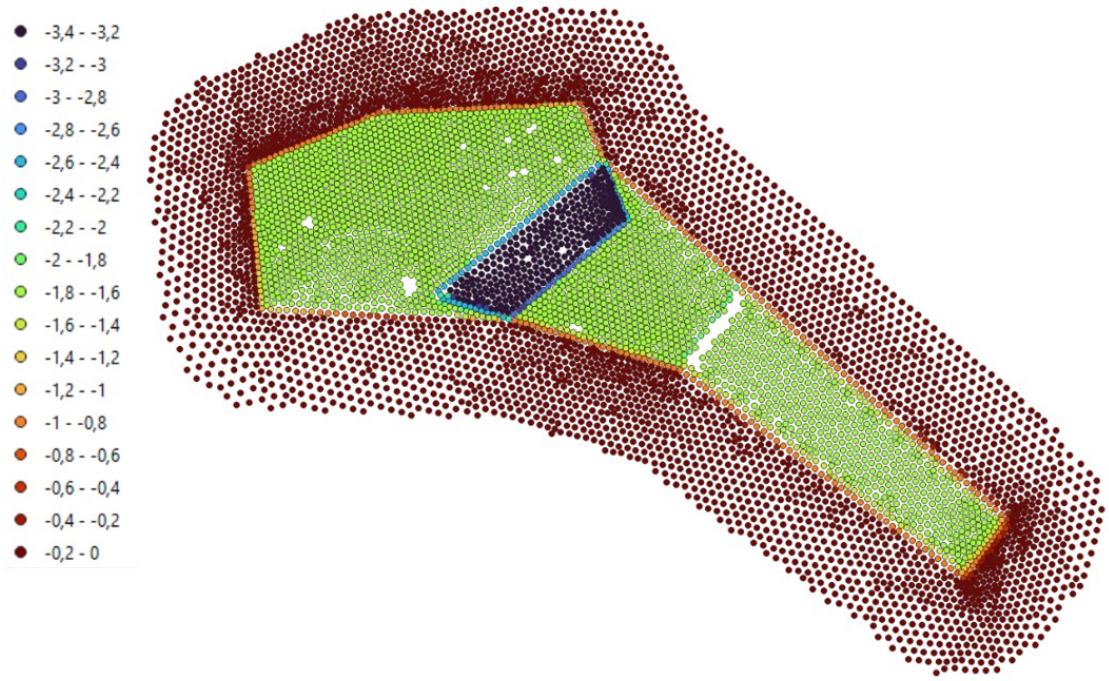

Figure 6.10 Visual representation of Knothe-Budryk analytical model results for the study area.

6.6 Land subsidence due to dewatering of an aquifer system

The Knothe-Budryk method computes the land subsidence that is mainly due to the extraction of material from the mining deposit. However, in order to get a full comprehension of the soil dynamics in the “Siersza” area, it is mandatory to take into account the land subsidence caused by the lowering of the water table before the starting of the mining activities.

Depth to the water table time series was recorded in piezometer P1 located in the central part of the mine (Figure 6.11). Initial head in this piezometer prior to the exploitation was estimated at 332.70 m.a.s.l., whereas groundwater head recorded after the mine closure in January 2001 was 135.30 m.a.s.l. Therefore, the head drop was 197.40 m. This can be kept as the maximum value of head decline during the exploitation. An evident groundwater rebound was recorded after the mine closure in 2001.

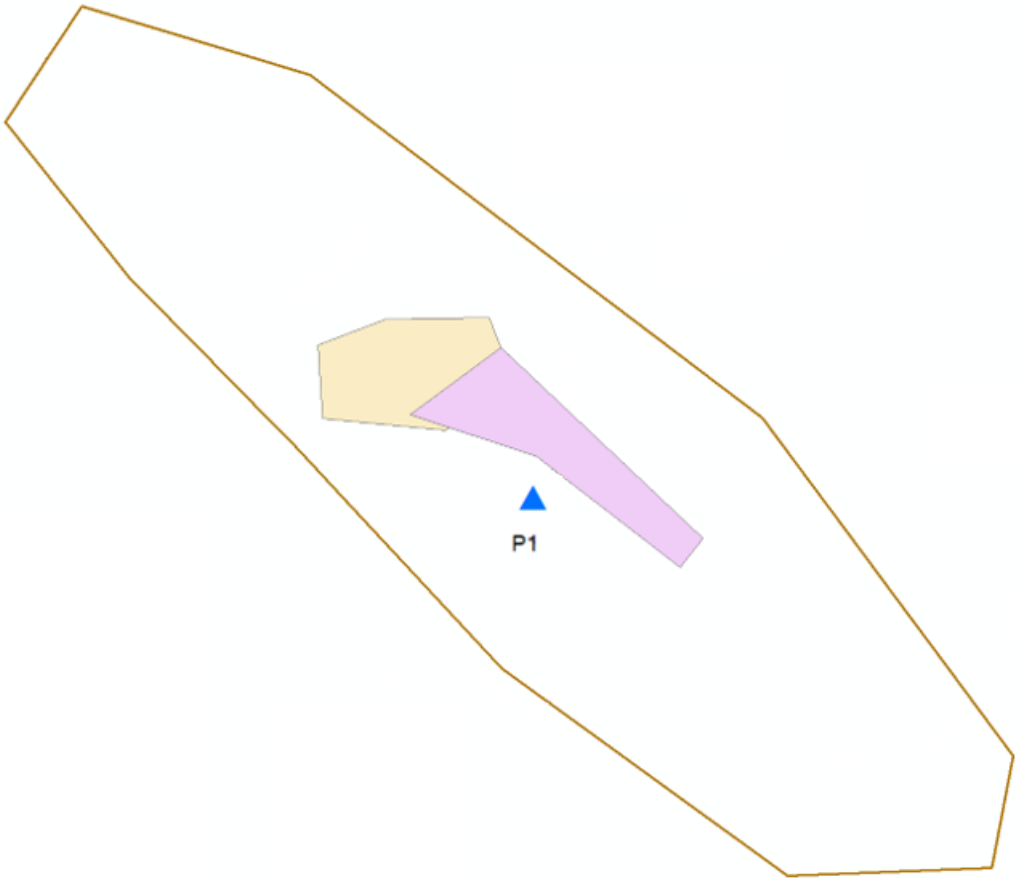

Figure 6.11 Location of piezometer P1 with respect to the Siersza mine.

Since the lack of hydrogeological information about the aquifers in the case study area, the layers are treated as phreatic aquifers. Therefore, the total land subsidence due to groundwater extraction is computed as the sum of the compaction of the different layers. As reported by Gambolati & Teatini (2021), the compaction of each layer of a phreatic aquifer system can be computed by Equation (6.7).

$$\eta = (s_0)\frac{(1\ +\ \nu)(1-2\nu)}{E\ (1\ -\ \nu)}\Delta\sigma_z \tag{6.7}$$

$$\Delta\sigma_z\ =\ \gamma_w\,\Delta_z\,(1\ -\ \phi\ +\ \theta_w) \tag{6.8}$$

in which E represents the Young modulus, ν is the Poisson coefficient, $\Delta\sigma_z$ indicates the change in the effective intergranular stress, s_0 is the layer thickness, and Δ_z is the difference between the natural piezometric level and the elevation of the average depth of each layer. Moreover, ϕ represents the porosity, it has been assumed equal to 0.15 (Wilk et al., 2003), θ_w is the irreducible water content, set as 0.1, and γ_w is the density of water. Young modulus and Poisson coefficients are taken from table 3. The outcomes of this calculation are provided in Table 5.
According to this, the sum of the compaction of each single layer is 11.63 m.
This value is to be considered as the maximum value of land vertical deformation that affects the study area. However, this quantity seems an overestimation of the actual values but, unfortunately, no direct records are available.

Table 5 Calculation for subsidence due to dewatering of the aquifer system

	Permian	Mine 50 m deep	Carboniferous between two mines	Mine 100 m deep	Carboniferous below the 100 m mine
$\Delta_z\ [m]$	7.6562	28.5597	54.5596	80.5595	185.6561
$\Delta\sigma_z$ [bar]	0.7133	2.6601	5.0830	7.5052	17.2964
$s_0\ [m]$	37.8070	4.0000	47.9997	4.0000	206.1932
$\eta\ [m]$	0.1404	0.0089	0.7530	0.0250	10.6992

Chapter 7

Results

In this section the vertical and horizontal displacements as computed by GEPS3D above the mine with the various scenarios are presented. The outcomes highlight the crucial role exerted by the stiffness of the exploited hard coal layer in the amount of land subsidence. The outcomes are depicted in the following figures and summarised in Table 6.

Table 6 Vertical and horizontal displacements as obtained by GEPS3D for the various scenarios investigated in this thesis work

		$DZ\ [m]$		$DX\ [m]$		$DY\ [m]$	
Scenario	E	Max	Min	Max	Min	Max	Min
1	Homogeneous	+0.006	-0.031	+0.010	-0.008	+0.010	-0.011
2	Heterogeneous	+0.0008	-0.0044	+0.003	-0.003	+0.004	-0.004
3	Heterogeneous with E divided by 10 for the coal mines	+0.008	-0.039	+0.007	-0.010	+0.008	-0.010
4	Heterogeneous with E divided by 1000 for the coal mines	+0.208	-3.432	+0.432	-0.737	+0.608	-0.821

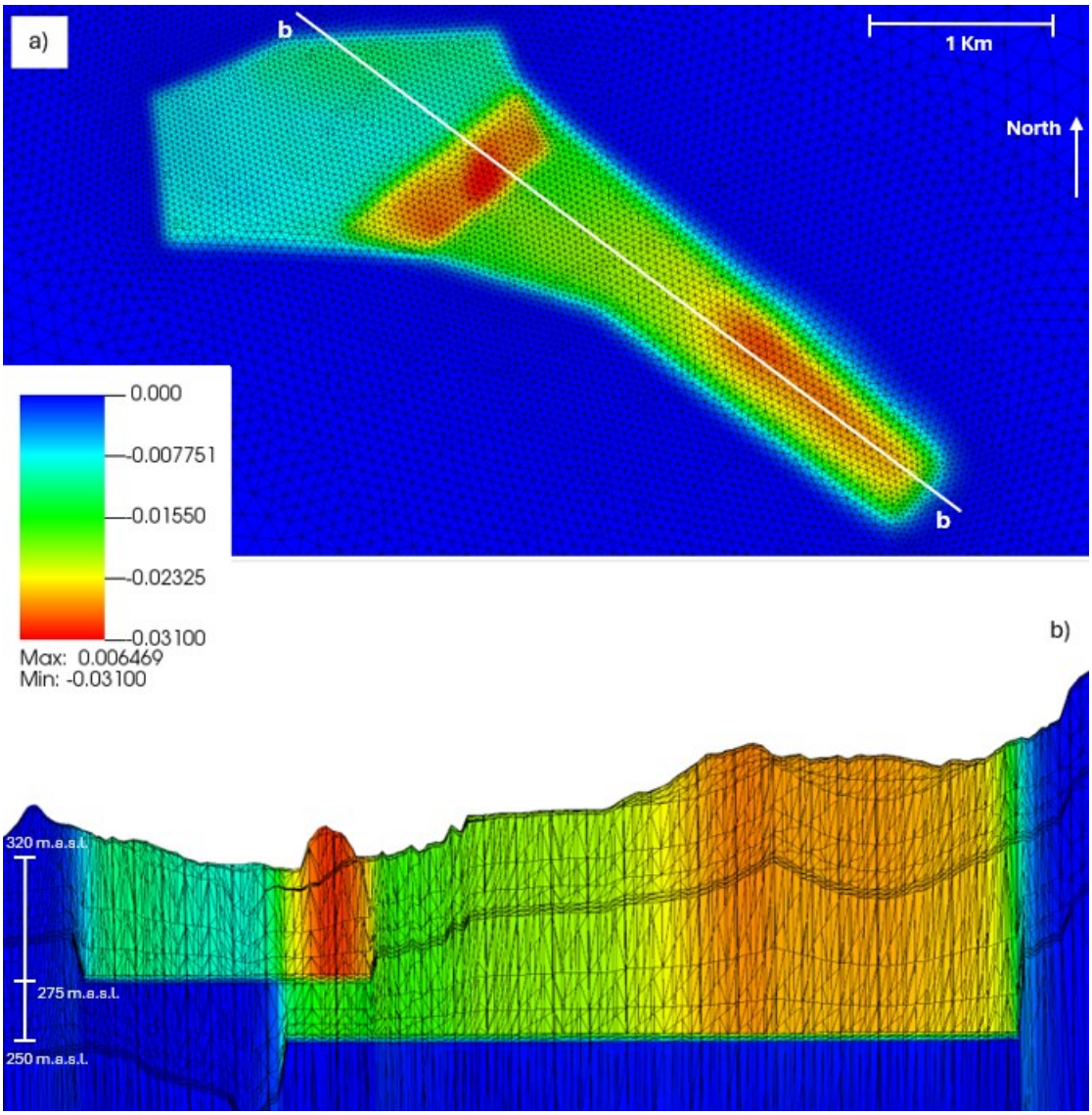

Figure 7.1 Scenario 1: vertical land displacements [m] on the land surface (a), and along a vertical NW-SE section crossing the mines (b).

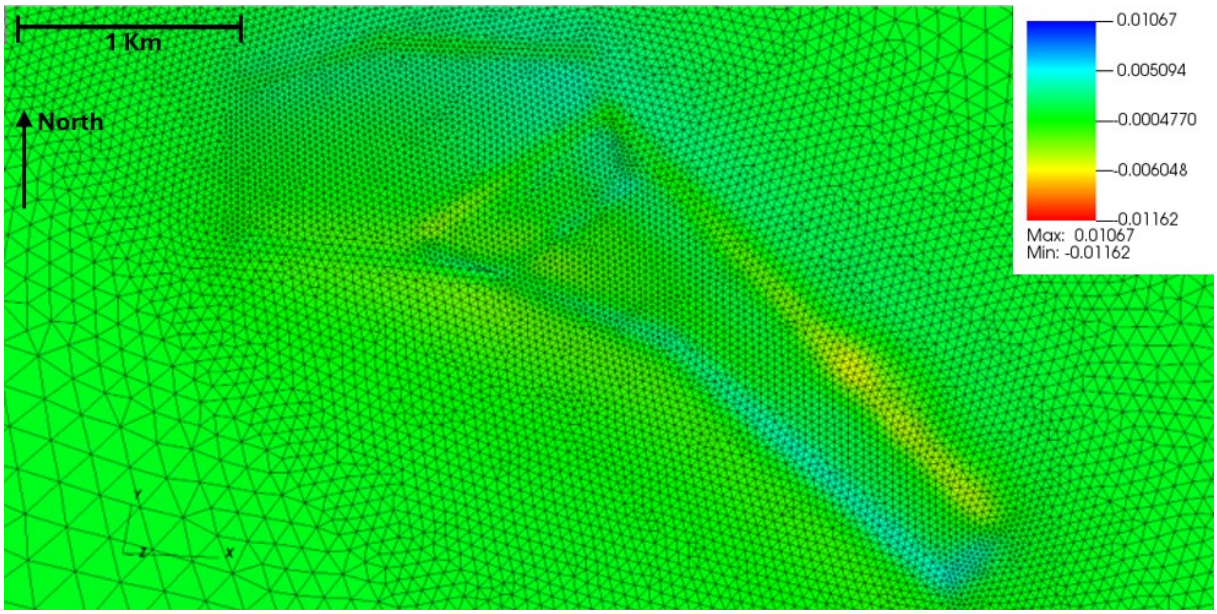

Figure 7.2 Scenario 1: horizontal component of the land displacements [m] along SN direction.

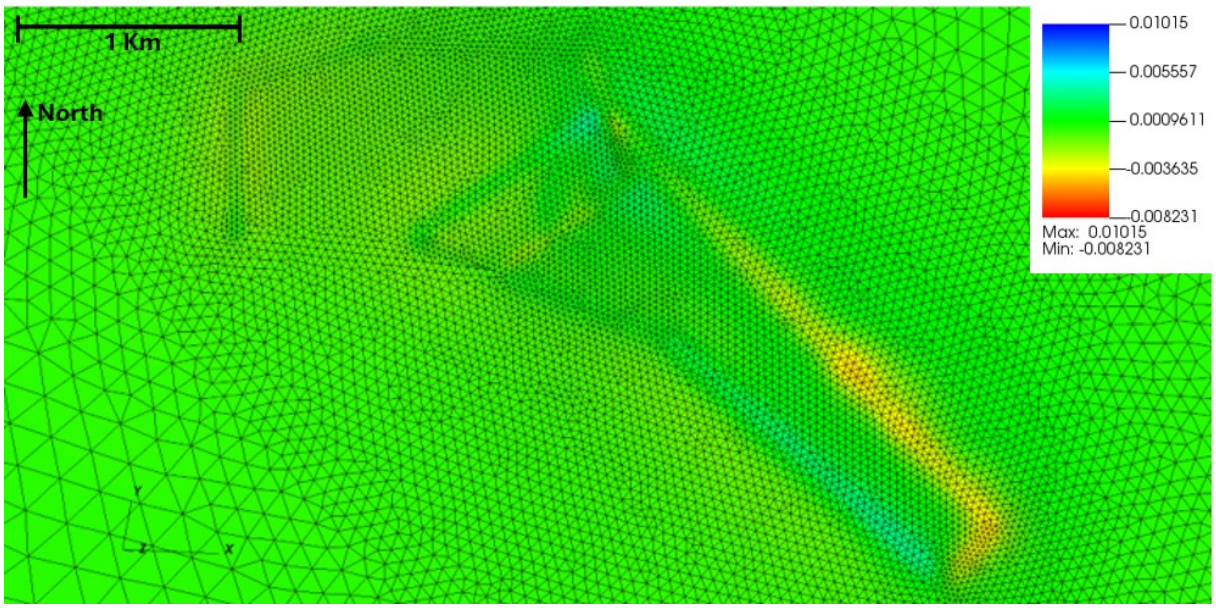

Figure 7.3 Scenario 1: horizontal component of the land displacements [m] along WE direction.

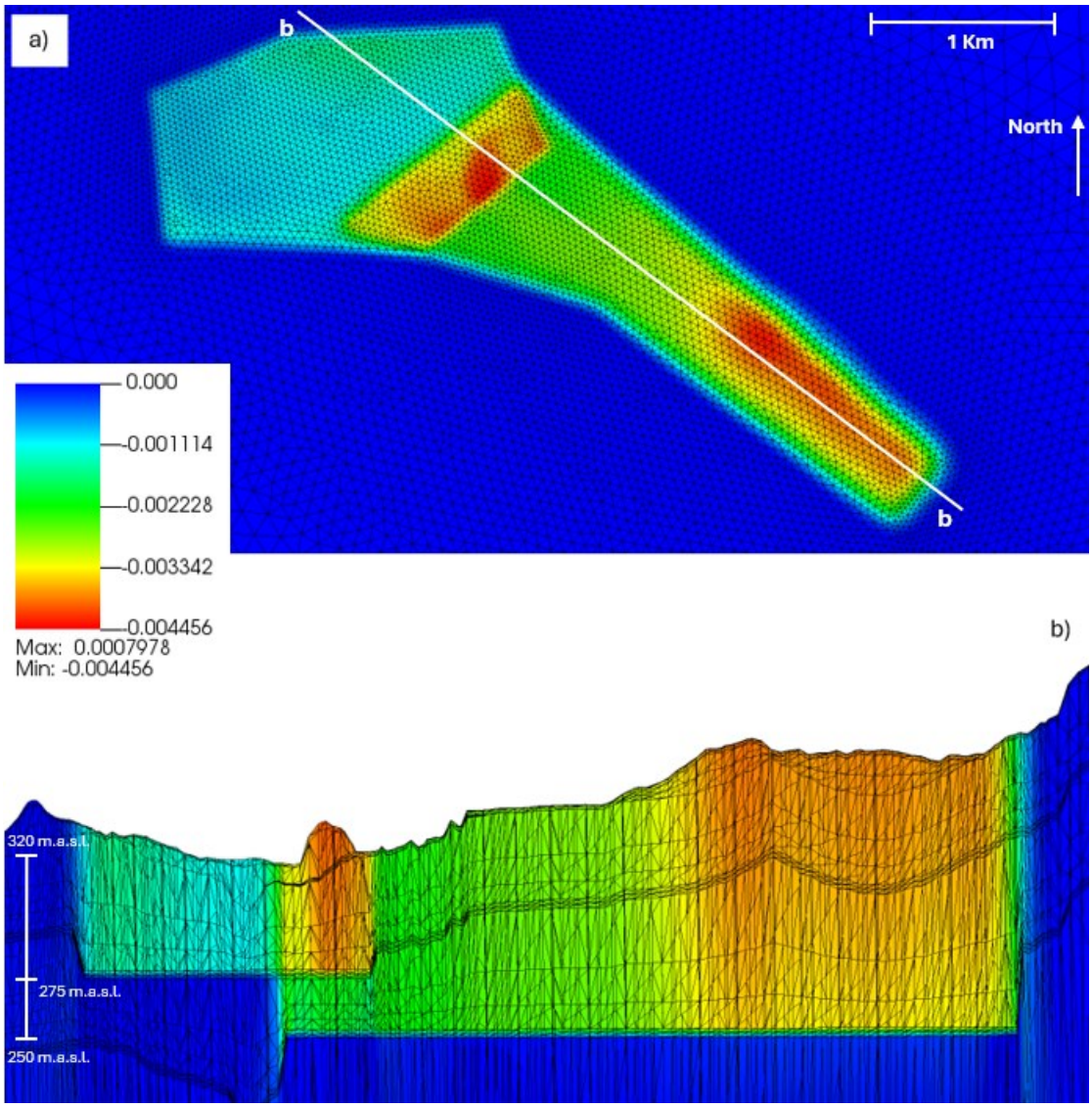

Figure 7.4 Scenario 2: vertical land displacements [m] on the land surface (a), and along a vertical NW-SE section crossing the mines (b).

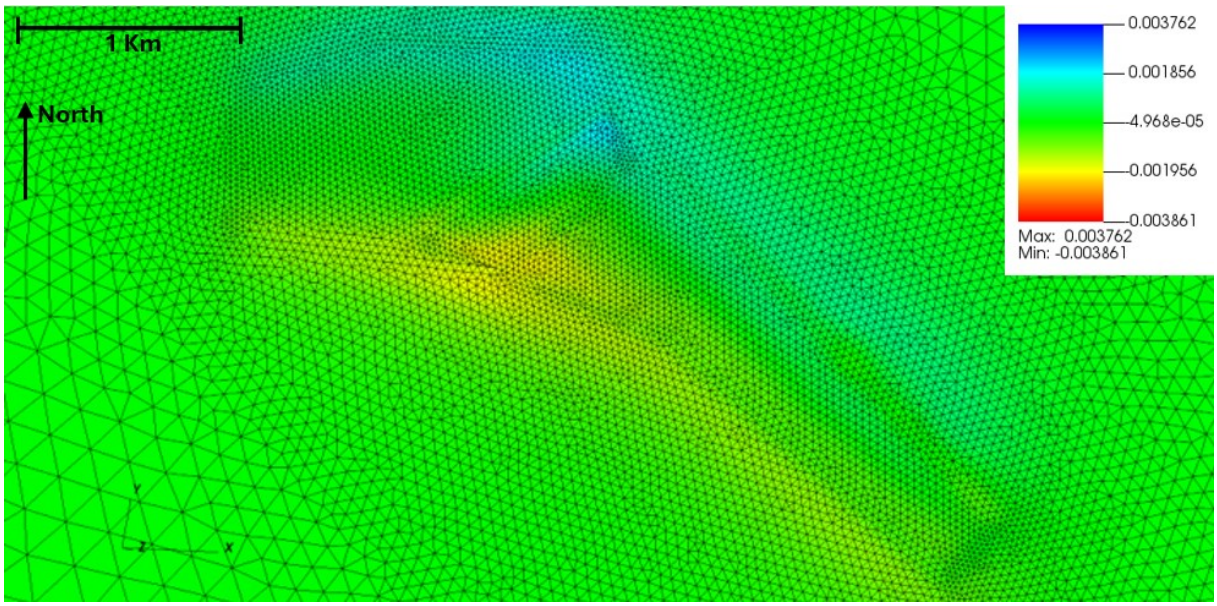

Figure 7.5 Scenario 2: horizontal component of the land displacements [m] along SN direction.

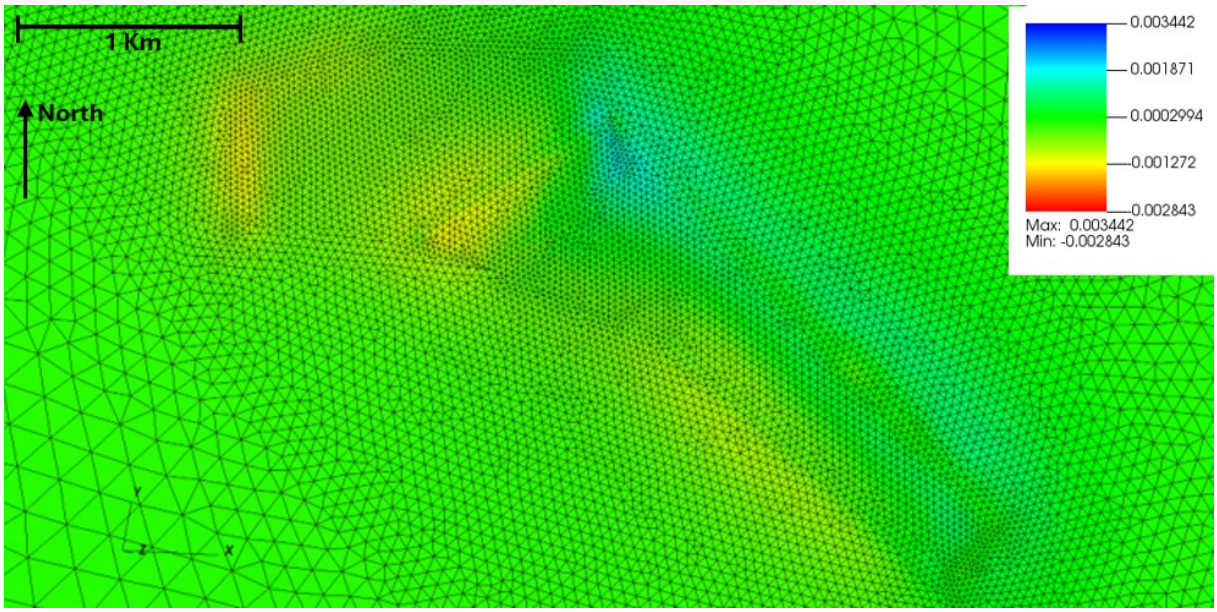

Figure 7.6 Scenario 2: horizontal component of the land displacements [m] along WE direction.

As expected, if the stiffness of the hard coal increases, moving from 0.987 GPa to 10.0 GPa, a less vertical land subsidence is obtained. The same mechanism is valid for the horizontal displacements.

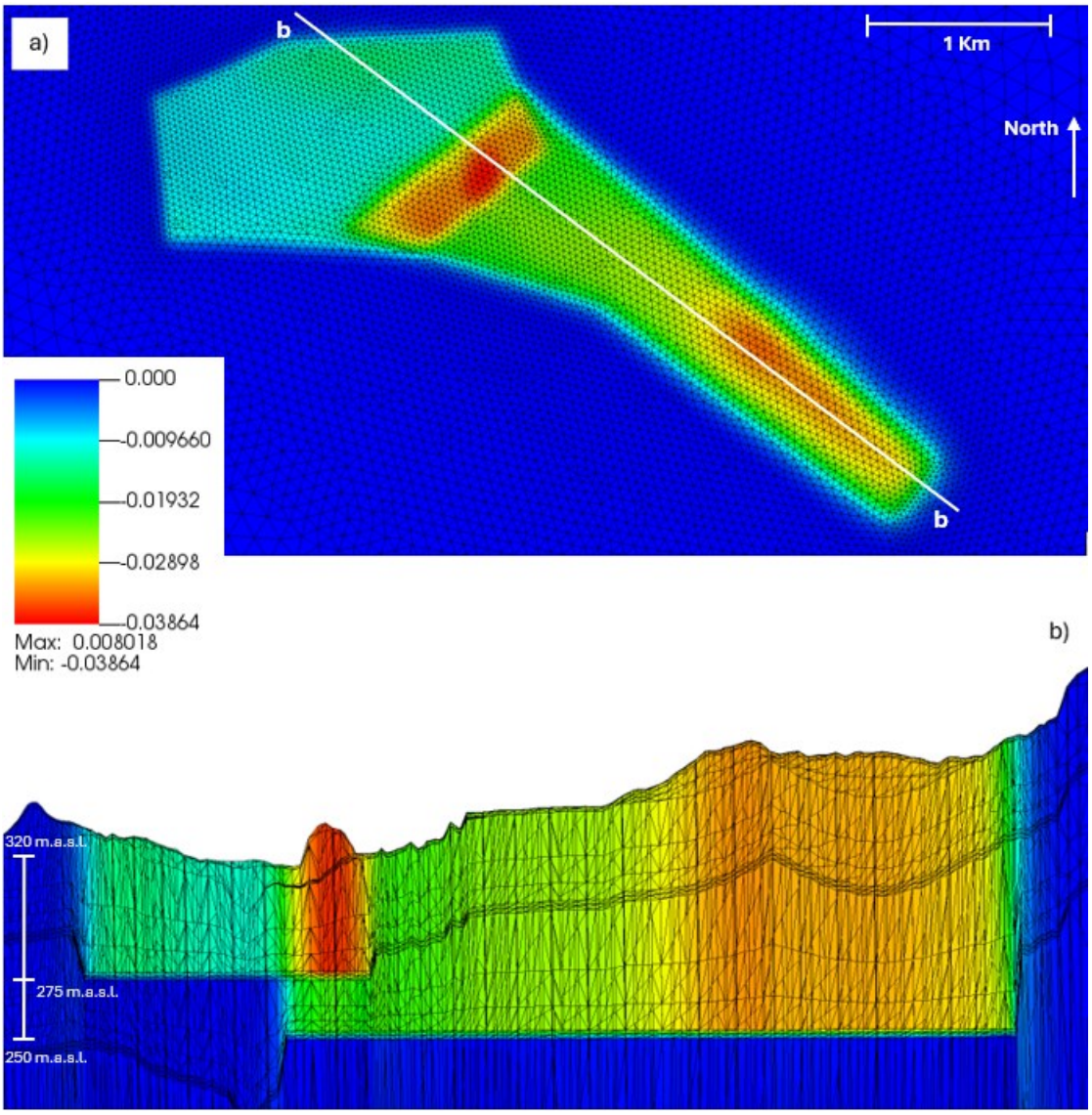

Figure 7.7 Scenario 3: vertical land displacements [m] on the land surface (a), and along a vertical NW-SE section crossing the mines (b).

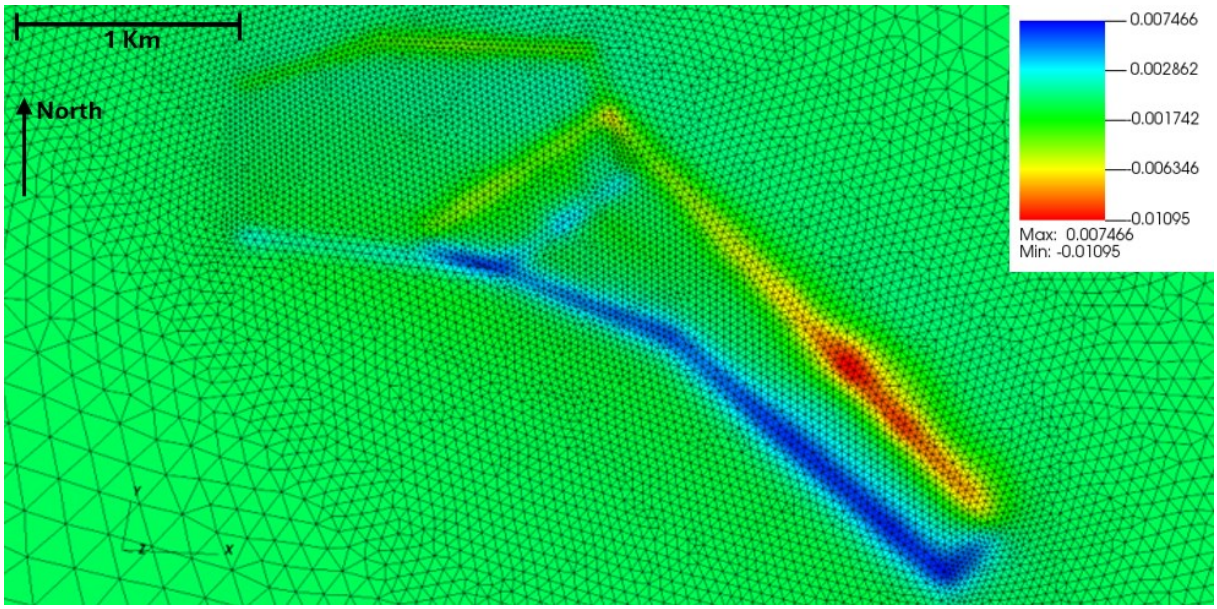

Figure 7.8 Scenario 3: horizontal component of the land displacements [m] along SN direction.

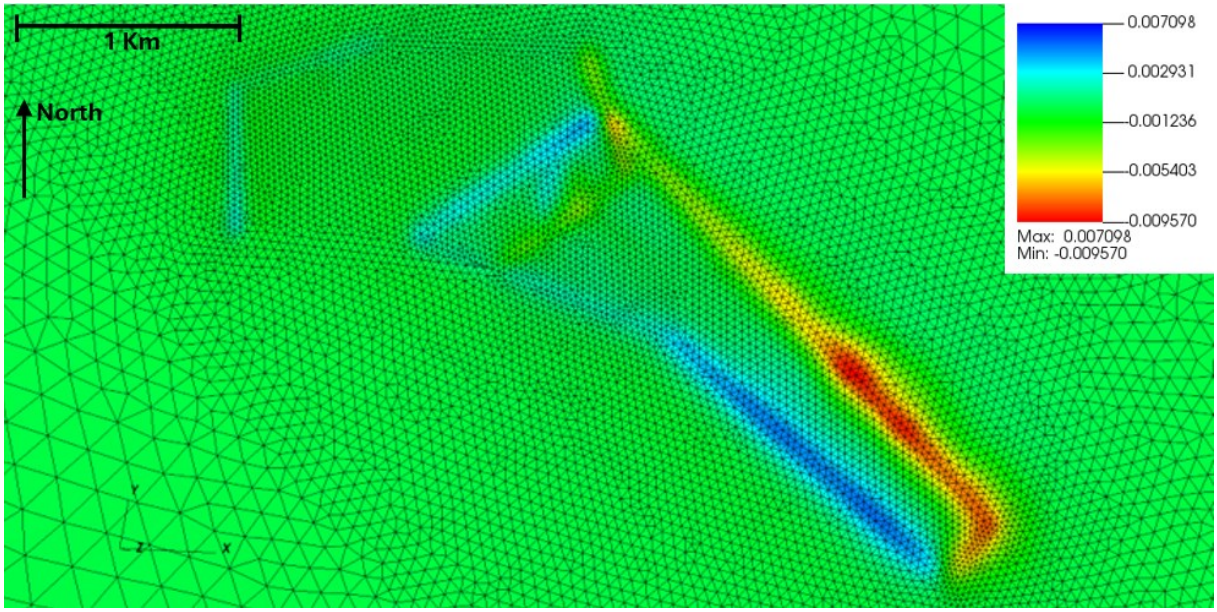

Figure 7.9 Scenario 3: horizontal component of the land displacements [m] along WE direction.

In Scenario 3 the hard coal stiffness has been decreased by ten times, reaching a value of 1.0 GPa. Consequently, the land subsidence increased by almost ten times, highlighting the reverse correspondence on the Young modulus. The horizontal displacements increase too, but they didn't follow the same numerical correspondence.

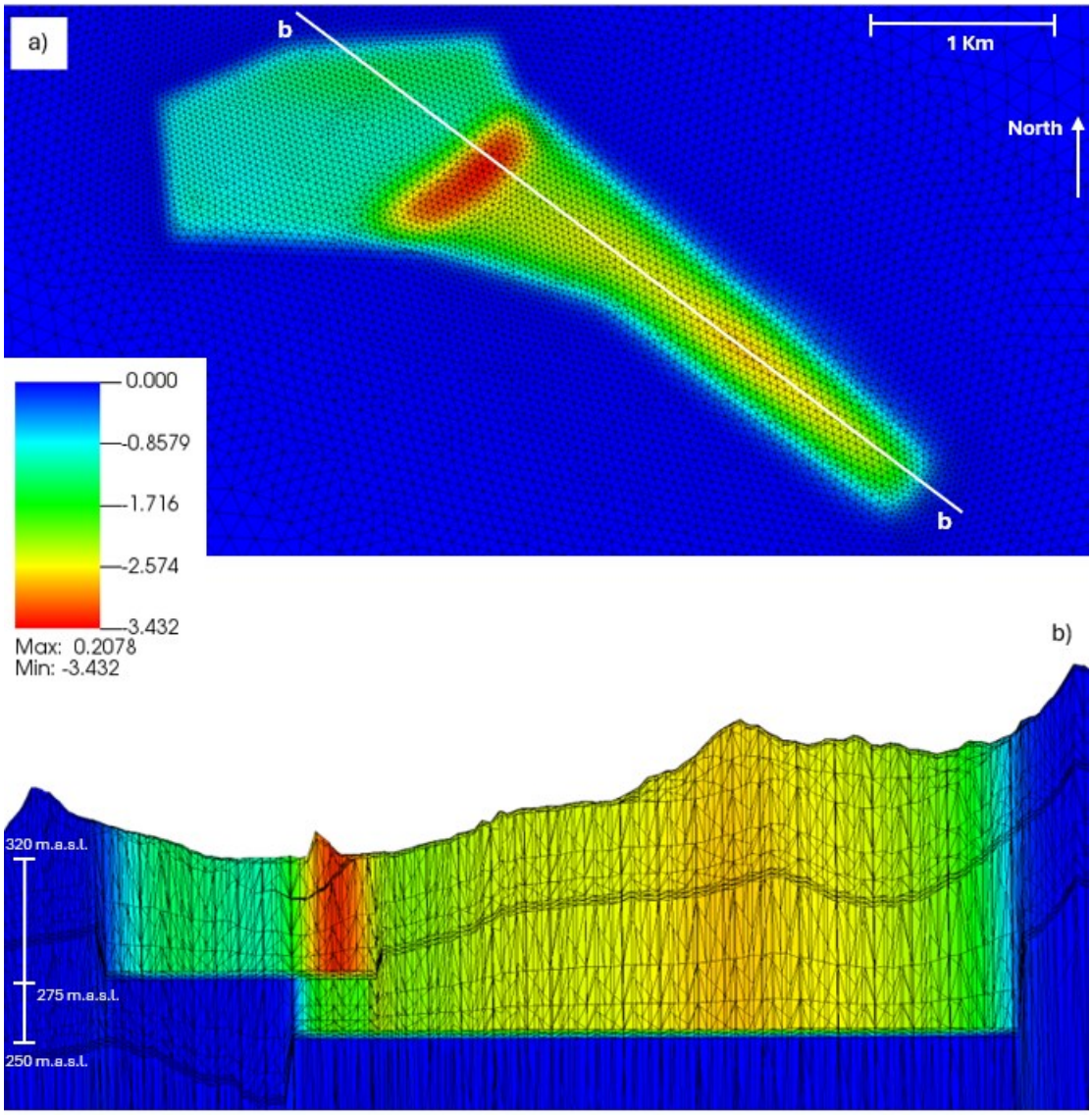

Figure 7.10 Scenario 4: vertical land displacements [m] on the land surface (a), and along a vertical NW-SE section crossing the mines (b).

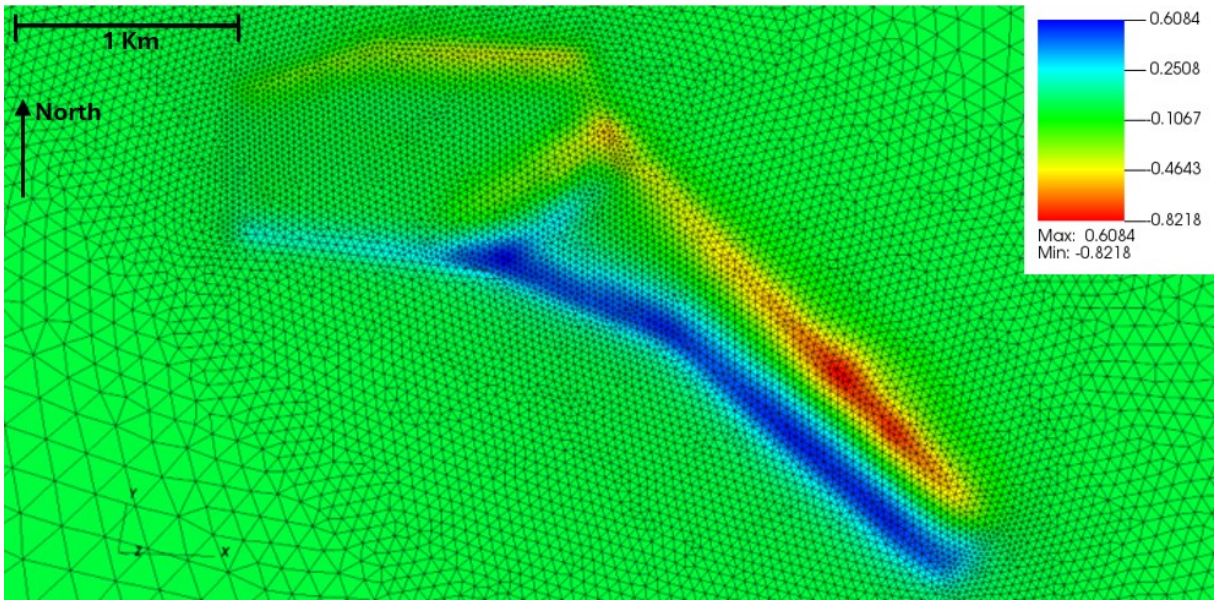

Figure 7.11 Scenario 4: horizontal component of the land displacements [m] along SN direction.

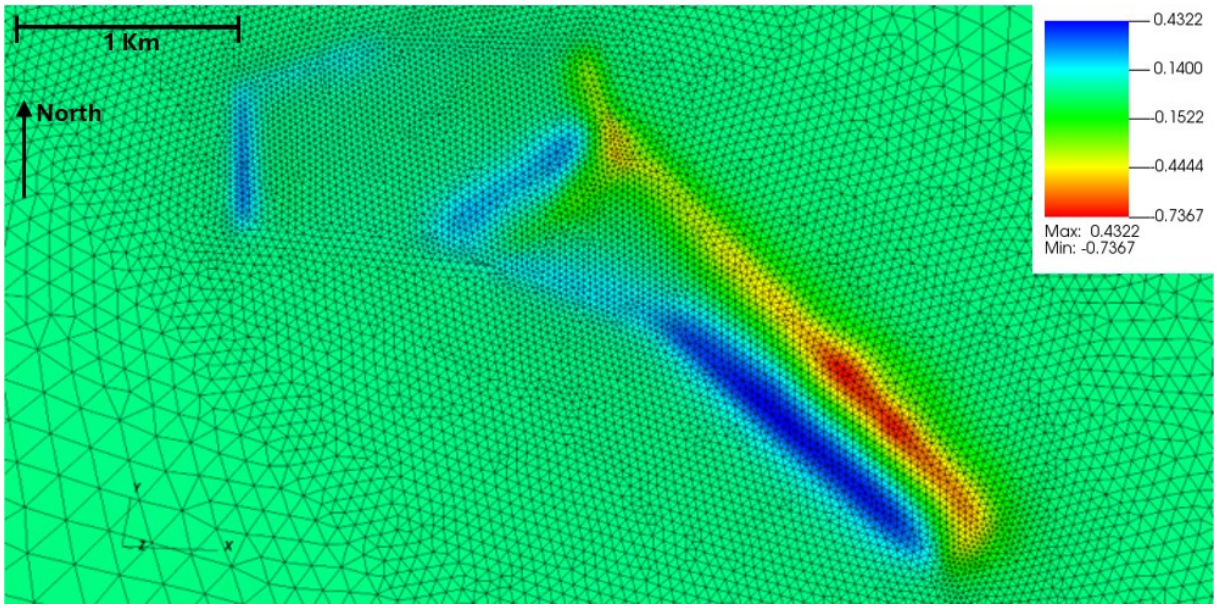

Figure 7.12 Scenario 4: horizontal component of the land displacements [m] along WE direction.

In these last results, the stiffness has been decreased by 1000 times. Even though this value has no proper physical meaning, it has been important to investigate this option too. The consequence of this is that the values of the computed land subsidence are similar to those obtained with the Knothe-Budryk method (sub-chapter 6.5).

Chapter 8

Conclusions

In this thesis, the geomechanical effects associated with the development of the “Siersza” mine have been quantified for the first time by using a three-dimensional numerical simulator. The modelling analysis is based on a huge hydrogeological and geomechanical dataset made available by the Polish Geological Institute, through the investigation of several boreholes. The data have allowed to properly characterize the stratigraphic setting of the area, the geometry of the hard coal mine panels, which are 50 and 100 m deep and 4 m thick, together with the distribution of the geomechanical properties, specifically the Young modulus and Poisson ratio. Data processing has allowed to build a two-dimensional FE mesh representing the horizontal view of the mine panels and, lately, the three-dimensional mesh of the mine panel geometry embedded in the three-dimensional geologic setting.

The forces causing soil displacements have been quantified starting from the geostatic load acting on the top and bottom of the hard coal mine panels no more counterbalanced when the coal is removed.

A number of scenarios have been simulated with different distribution of the Young modulus. This set of simulations has allowed to increase the familiarity with the model behaviour, testing parameter distribution even more close to reality. The sensitivity analysis, for example, has allowed to very how the model response is largely dependent on the stiffness assigned to the hard coal mine units.

The availability of a land subsidence estimate computed using the Knothe-Budryk analytical model, which is traditionally used to estimate the process, has allowed to verify how the scenario providing the outcome closer to this analytical function is characterized by a heterogeneous distribution of the soil stiffness, in agreement with the lithological information, and the excavated coal mine panels 1000 weaker than the surrounding carboniferous rock. This configuration is equivalent to removing the finite elements corresponding to excavations from the three-dimensional mesh. The maximum subsidence amount to about 3.4 m. A simplified 1D characterization of the land subsidence possibly caused by the lowering of the water table (up to almost 200 m) carried out before the start of the mining activities has allowed to estimate this contribution in more than 10 m. This value seems an over-estimation, but no records are available.

It is worth noting that this research represents an initial effort of a long process aimed to improve our knowledge about the three-dimensional deformation and stress fields resulting from shallow mining activities. This is fundamental to start understanding the factors contributing to sinkhole occurrences in these areas after the mine abandonment. Pressure changes calculations due to groundwater withdrawal, the progressive weakening of the soil following rewetting, the implementation of the proper backfilling method, and the use of InSAR measurements to calibrate the geomechanical parameters will be implemented in future phases.

References

Arctic Sinkholes I Full Documentary I NOVA I PBS - YouTube. (n.d.). https://www.youtube.com/watch?v=HvKpnaXYUPU

Atkinson, T. C. (1977). Diffuse flow and conduit flow in limestone terrain in the Mendip Hills, Somerset (Great Britain). *Journal of Hydrology*, *35*(1–2), 93–110. https://doi.org/10.1016/0022-1694(77)90079-8

Banks, D., Frolik, A., Gzyl, G., & Rogoż, M. (2010). Modeling and monitoring of mine water rebound in an abandoned coal mine complex: Siersza Mine, Upper Silesian Coal Basin, Poland. *Hydrogeology Journal*, *18*(2). https://doi.org/10.1007/s10040-009-0534-z

Bates, R. L., & Jackson, J. A. (1987). Glossary of Geology. Third edition. *Glossary of Geology. Third Edition*.

Biot, M. A. (1941). General Theory of Three-Dimensional Consolidation. *Journal of Applied Physics*, *12*(2), 155–164. https://doi.org/10.1063/1.1712886

Blachowski, J., Kopec, A., Milczarek, W., & Owczarz, K. (2019). Evolution of secondary deformations captured by satellite radar interferometry: Case study of an abandoned coal basin in SW Poland. *Sustainability (Switzerland)*, *11*(3). https://doi.org/10.3390/su11030884

Bonì, R., Meisina, C., Teatini, P., Zucca, F., Zoccarato, C., Franceschini, A., Ezquerro, P., Béjar-Pizarro, M., Antonio Fernández-Merodo, J., Guardiola-Albert, C., Luis Pastor, J., Tomás, R., & Herrera, G. (2020). 3D groundwater flow and deformation modelling of Madrid aquifer. *Journal of Hydrology*, *585*. https://doi.org/10.1016/j.jhydrol.2020.124773

Brinkmann, R., Parise, M., & Dye, D. (2008). Sinkhole distribution in a rapidly developing urban environment: Hillsborough County, Tampa Bay area, Florida. *Engineering Geology*, *99*(3–4). https://doi.org/10.1016/j.enggeo.2007.11.020

Buttrick, D., & Van Schalkwyk, A. (1998). Hazard and risk assessment of sinkhole formation on dolomite land in South Africa. *Environmental Geology*, *36*(1–2). https://doi.org/10.1007/s002540050333

Cai, Y., Li, X., Xiao, W., & Zhang, W. (2020). Simulation of mining-induced ground damage using orthogonal experiments to determine key parameters of super-large coalface: A case study in Shendong Coalfield in China. *Applied Sciences (Switzerland)*, *10*(7). https://doi.org/10.3390/app10072258

Carpinteri, A. (1995). *Scienza Delle Costruzioni Vol.1*. https://it.scribd.com/doc/146299724/Scienza-delle-Costruzioni-vol-1-A-Carpinteri-pdf

Delle Rose, M. (2022). Sinkhole Flooding and Aquifer Recharge in Arid to Dry Sub-Humid Regions: A Systematic Review in the Perspective of Climate Change. *Hydrology 2022, Vol. 9, Page 25*, *9*(2), 25. https://doi.org/10.3390/HYDROLOGY9020025

Devin, G. L., David, J. R., & Steven, I. E. (1999). (PDF) Land Subsidence in the United States. In *US Geological Survey Circular 1182*. https://www.researchgate.net/publication/256087212_Land_Subsidence_in_the_United_States

Energy Policy of Poland until 2040 (EPP2040) - Ministry of Climate and Environment. https://www.gov.pl/web/climate/energy-policy-of-poland-until-2040-epp2040

Esaki, T., Kimura, T., & Shikata, K. (1989). Subsidence and environmental impacts in Japanese coal mining. *30th U.S. Symposium on Rock Mechanics, USRMS 1989*. https://doi.org/10.1016/0148-9062(90)94846-l

Ferentinou, M., Witkowski, W., Hejmanowski, R., Grobler, H., & Malinowska, A. (2020). Detection of sinkhole occurrence, experiences from South Africa. *Proceedings of the International Association of Hydrological Sciences*, *382*. https://doi.org/10.5194/piahs-382-77-2020

Field Guide to Guatemalan Geology: Stanford Alpine Project : 2004-2005 - Google Libri. (n.d.). https://books.google.pl/books/about/Field_Guide_to_Guatemalan_Geology.html?id=mppOAQAAIAAJ&redir_esc=y

Fletcher, S. J. (2023). Introduction to Finite Element Modeling. In *Data Assimilation for the Geosciences*. https://doi.org/10.1016/b978-0-32-391720-9.00015-2

Florida's most famous sinkhole | Sinkholes | The Guardian. (n.d.). https://www.theguardian.com/world/2013/aug/14/florida-most-famous-sinkhole

Franceschini, A. (2014). *Formulazione lagrangiana del problema del contatto applicato a faglie geologiche*. https://thesis.unipd.it/handle/20.500.12608/18785

Franceschini, A., Castelletto, N., White, J. A., & Tchelepi, H. A. (2020). Algebraically stabilized Lagrange multiplier method for frictional contact mechanics with hydraulically active fractures. *Computer Methods in Applied Mechanics and Engineering*, *368*. https://doi.org/10.1016/j.cma.2020.113161

Franceschini, A., Castelletto, N., White, J. A., & Tchelepi, H. A. (2022). Scalable preconditioning for the stabilized contact mechanics problem. *Journal of Computational Physics*, *459*. https://doi.org/10.1016/j.jcp.2022.111150

Freedman, A., & Khurshudyan, I. (2020). Siberia's persistent temperature spike propels globe to break records - The Washington Post. In *Siberia's persistent, freakishly mild weather is reverberating around the world*. https://www.washingtonpost.com/weather/2020/06/15/siberia-record-warmth/

Gambolati, G., & Ferronato, M. (2015). *Lezioni di metodi numerici per l'ingegneria*. https://www.ibs.it/lezioni-di-metodi-numerici-per-libro-giuseppe-gambolati-massimiliano-ferronato/e/9788896477656

Gambolati, G., Gatto, P., & Ricceri, G. (1986). Land subsidence due to gas-oil removal in layered anisotropic soils by a finite element model. *Land Subsidence. Proc. 3rd Symposium, Venice, 1984*. https://doi.org/10.1016/0148-9062(87)90988-0

Gambolati, G., & Teatini, P. (2021). Land Subsidence and its Mitigation. In *Land Subsidence and its Mitigation*. https://doi.org/10.21083/978-1-77470-001-3

Geuzaine, C., & Remacle, J. F. (2009). Gmsh: A 3-D finite element mesh generator with built-in pre- and post-processing facilities. *International Journal for Numerical Methods in Engineering*, *79*(11). https://doi.org/10.1002/nme.2579

Gongyu, L., & Wanfang, Z. (1999). Sinkholes in karst mining areas in China and some methods of prevention. *Engineering Geology*, *52*(1–2). https://doi.org/10.1016/S0013-7952(98)00053-2

Guatemala City hit by second sinkhole | New Civil Engineer. (n.d.). https://www.newcivilengineer.com/archive/guatemala-city-hit-by-second-sinkhole-09-06-2010/

Gutiérrez, F., Benito-Calvo, A., Carbonel, D., Desir, G., Sevil, J., Guerrero, J., Martínez-Fernández, A., Karamplaglidis, T., García-Arnay, Á., & Fabregat, I. (2019). Review on sinkhole monitoring and performance of remediation measures by high-precision leveling and terrestrial laser scanner in the salt karst of the Ebro Valley, Spain. In *Engineering Geology* (Vol. 248, pp. 283–308). Elsevier B.V. https://doi.org/10.1016/j.enggeo.2018.12.004

Guzy, A., & Witkowski, W. T. (2021). Land subsidence estimation for aquifer drainage induced by underground mining. *Energies*, *14*(15). https://doi.org/10.3390/en14154658

He, M. C. (2006). *ROCK MECHANICS AND HAZARD CONTROL IN DEEP MINING ENGINEERING IN CHINA*. https://doi.org/10.1142/9789812772411_0003

Hermosilla, R. G. (2012). The Guatemala City sinkhole collapses. *Carbonates and Evaporites*, *27*(2). https://doi.org/10.1007/s13146-011-0074-1

Intrieri, E., Gigli, G., Nocentini, M., Lombardi, L., Mugnai, F., Fidolini, F., & Casagli, N. (2015). Sinkhole monitoring and early warning: An experimental and successful GB-InSAR application. *Geomorphology*, *241*. https://doi.org/10.1016/j.geomorph.2015.04.018

Isotton, G., Teatini, P., Ferronato, M., Janna, C., Spiezia, N., Mantica, S., & Volonte, G. (2019). Robust numerical implementation of a 3D rate-dependent model for reservoir geomechanical simulations. *International Journal for Numerical and Analytical Methods in Geomechanics*, *43*(18). https://doi.org/10.1002/nag.3000

Japan: Repaired Fukuoka sinkhole sinks again - BBC News. (n.d.). https://www.bbc.com/news/world-asia-38129691

Kaufmann, G., Gabrovšek, F., & Romanov, D. (2016). Dissolution and precipitation of fractures in soluble rock. *Hydrology and Earth System Sciences Discussions*, *August*. https://doi.org/10.5194/hess-2016-372

Kersten, T., Kobe, M., Gabriel, G., Timmen, L., Schön, S., & Vogel, D. (2017). Geodetic monitoring of subrosion-induced subsidence processes in urban areas: Concept and status report. *Journal of Applied Geodesy*, *11*(1). https://doi.org/10.1515/jag-2016-0029

Kim, T. T. H., Tran, H. H., Bui, K. L., & Lipecki, T. (2021). Mining-induced Land Subsidence Detected by Sentinel-1 SAR Images: An Example from the Historical Tadeusz Kościuszko Salt Mine at Wapno, Greater Poland Voivodeship, Poland. *Inzynieria Mineralna*, *1*(2). https://doi.org/10.29227/IM-2021-02-04

Kleinhans, I., & Van Rooy, J. L. (2016). Guidelines for sinkhole and subsidence rehabilitation based on generic geological models of a dolomite environment on the East Rand, South Africa. *Journal of African Earth Sciences*, *117*. https://doi.org/10.1016/j.jafrearsci.2016.01.001

Linares, R., Roqué, C., Gutiérrez, F., Zarroca, M., Carbonel, D., Bach, J., & Fabregat, I. (2017). The impact of droughts and climate change on sinkhole occurrence. A case study from the evaporite karst of the Fluvia Valley, NE Spain. *Science of The Total Environment*, *579*, 345–358. https://doi.org/10.1016/J.SCITOTENV.2016.11.091

Malinowska, A. A., Witkowski, W. T., Hejmanowski, R., Chang, L., van Leijen, F. J., & Hanssen, R. F. (2019). Sinkhole occurrence monitoring over shallow abandoned coal mines with satellite-based persistent scatterer interferometry. *Engineering Geology*, *262*. https://doi.org/10.1016/j.enggeo.2019.105336

Malinowska, A., Hejmanowski, R., & Dai, H. (2020). Ground movements modeling applying adjusted influence function. *International Journal of Mining Science and Technology*, *30*(2), 243–249. https://doi.org/10.1016/J.IJMST.2020.01.007

Milczarek, W., Kopeć, A., Głabicki, D., & Bugajska, N. (2021). Induced seismic events—distribution of ground surface displacements based on insar methods and mogi and yang models. *Remote Sensing*, *13*(8). https://doi.org/10.3390/rs13081451

Mir, R. A., Ahmed, R., Hussain, M., Bukhari, S. K., Ahmed, P., Dar, R. A., Ahmad, S. T., Wani, G. F., Ahad, A. I., Rather, A. F., Bhat, I. A., Mifta-ul-Shafiq, & Bhat, W. A. (2023). Causes, concerns and hazards of sinkhole formation in Brengi stream catchment of Upper Jhelum basin, Kashmir Himalaya. *Environment, Development and Sustainability*. https://doi.org/10.1007/s10668-023-03204-1

Misa, R. (2023). Knothe's theory parameters – computational models and examples of practical applications. *Gospodarka Surowcami Mineralnymi – Mineral Resources Management*, *39*(4), 157–180. https://doi.org/10.24425/GSM.2023.148164

Nof, R. N., Baer, G., Ziv, A., Raz, E., Atzori, S., & Salvi, S. (2013). Sinkhole precursors along the Dead Sea, Israel, revealed by SAR interferometry. *Geology*, *41*(9). https://doi.org/10.1130/G34505.1

Ochoa-González, G. H., Carreón-Freyre, D., Franceschini, A., Cerca, M., & Teatini, P. (2018). Overexploitation of groundwater resources in the faulted basin of Querétaro, Mexico: A 3D deformation and stress analysis. *Engineering Geology*, *245*. https://doi.org/10.1016/j.enggeo.2018.08.014

Oosthuizen, T., & Heath, G. (2008). (PDF) A preliminary overview of the sinkhole record of South Africa. *Problem Soils Seminar*. https://www.researchgate.net/publication/289532686_A_preliminary_overview_of_the_sinkhole_record_of_South_Africa

Osterkamp, T. E., & Burn, C. R. (2003). PERMAFROST. *Encyclopedia of Atmospheric Sciences*, 1717–1729. https://doi.org/10.1016/B0-12-227090-8/00311-0

Oštir, K., & Komac, M. (2007). PSInSAR and DInSAR methodology comparison and their applicability in the field of surface deformations–A case of NW Slovenia. *Geologija*, *50*(1). https://doi.org/10.5474/geologija.2007.007

Panno, S. V, Curry, B. B., Wang, H., Hackley, K. C., Zhang, Z., & Lundstrom, C. C. (2012). The effects of climate change on speleogenesis and karstification since the penultimate glaciation in southwestern Illinois' sinkhole plain. *Carbonates and Evaporites*, *27*(1), 87–94. https://doi.org/10.1007/S13146-012-0086-5/TABLES/1

Pigorini, A., Ricci, M., Sciotti, A., Giannico, C., & Tamburini, A. (2010). Satellite remote-sensing PSInSAR technique applied to design and construction of railway infrastructures. *Ingegneria Ferroviaria*, *2*.

Przyłucka, M., Kowalski, Z., & Perski, Z. (2022). Twenty years of coal mining-induced subsidence in the Upper Silesia in Poland identified using InSAR. *International Journal of Coal Science and Technology*, *9*(1), 1–11. https://doi.org/10.1007/S40789-022-00541-W/FIGURES/5

QGIS: An Introduction to an Open-Source Geographic Information System | Mississippi State University Extension Service. (n.d.). https://extension.msstate.edu/publications/qgis-introduction-open-source-geographic-information-system

Report on analytical work on terrain deformations in Trzebinia. (2023). https://www.pgi.gov.pl/aktualnosci/display/14601-raport-z-prac-analitycznych-o-deformacjach-terenu-w-trzebini.html

Residents Assured of State Support as Sinkhole Threat Looms in Trzebinia - PolandDaily24.com. (n.d.). https://polanddaily24.com/residents-assured-of-state-support-as-sinkhole-threat-looms-in-trzebinia/politics/23783

Ribeiro e Sousa, L., Vargas Jr, E., Fernandes, M. M., & Azevedo, R. (2012). Innovative Numerical Modelling in Geomechanics. In *Innovative Numerical Modelling in Geomechanics*. https://doi.org/10.1201/b12130

Rome: sinkhole opens up in front of Pantheon - Wanted in Rome. (n.d.). https://www.wantedinrome.com/news/rome-sinkhole-opens-in-front-of-pantheon.html

Rucker, M. L., Panda, B. B., Meyers, R. A., & Lommler, J. C. (2013). Using InSAR to detect subsidence at brine wells, sinkhole sites, and mines. *Carbonates and Evaporites*, *28*(1–2). https://doi.org/10.1007/s13146-013-0134-9

Scientists climb to bottom of Siberian sinkhole - in pictures | World news | The Guardian. (n.d.). https://www.theguardian.com/world/gallery/2014/nov/13/scientists-climb-to-bottom-of-siberian-sinkhole-in-pictures

Scopus. (n.d.). https://www.scopus.com/term/analyzer.uri?sort=plf-f&src=s&sid=5d49ad9e178dcfde9cb5731e68b72c5e&sot=a&sdt=a&sl=23&s=TITLE-ABS-KEY%28sinkhole%29&origin=resultslist&count=10&analyzeResults=Analyze+results

Singh, K. B., & Dhar, B. B. (1997). Sinkhole subsidence due to mining. *Geotechnical and Geological Engineering*, *15*(4). https://doi.org/10.1007/bf00880712

Sinkholes | U.S. Geological Survey. (n.d.). https://www.usgs.gov/special-topics/water-science-school/science/sinkholes#overview

Sinkholes in Trzebinia. There are test results of the SRK recovery plan and plan. (n.d.). https://tvs.pl/informacje/trzebinia-dziurawa-jak-ser-zapada-sie-cmentarz-sa-wyniki-badan/

Soldo, B., Sivand, S. M., Afrasiabian, A., & Đurin, B. (2020). Effect of sinkholes on groundwater resources in arid and semi-arid karst area in Abarkooh, Iran. *Environments - MDPI*, *7*(4). https://doi.org/10.3390/environments7040026

Spiezia, N., Ferronato, M., Janna, C., & Teatini, P. (2017). A two-invariant pseudoelastic model for reservoir compaction. *International Journal for Numerical and Analytical Methods in Geomechanics*, *41*(18). https://doi.org/10.1002/nag.2704

Szpor, A., & Ziółkowska, K. (2018). The Transformation of the Polish Coal Sector. *International Institute for Sustainable Development*, *January*.

Talib, O. C., Shimon, W., Sarah, K., & Tonian, R. (2022). Detection of sinkhole activity in West-Central Florida using InSAR time series observations. *Remote Sensing of Environment*, *269*. https://doi.org/10.1016/j.rse.2021.112793

Teatini, P., Castelletto, N., Ferronato, M., Gambolati, G., Janna, C., Cairo, E., Marzorati, D., Colombo, D., Ferretti, A., Bagliani, A., & Bottazzi, F. (2011). Geomechanical response to seasonal gas storage in depleted reservoirs: A case study in the Po River basin, Italy. *Journal of Geophysical Research: Earth Surface*, *116*(2). https://doi.org/10.1029/2010JF001793

The Paris Agreement | UNFCCC. (n.d.). https://unfccc.int/process-and-meetings/the-paris-agreement

Theron, A., Engelbrecht, J., Kemp, J., Kleynhans, W., & Turnbull, T. (2017). Detection of Sinkhole Precursors Through SAR Interferometry: Radar and Geological Considerations. *IEEE Geoscience and Remote Sensing Letters*, *14*(6). https://doi.org/10.1109/LGRS.2017.2684905

Tihansky, A. B. (1999). Sinkholes, West-Central Florida. *US Geological Survey Circular*, *1182*.

Vaccari, A., Stuecheli, M., Bruckno, B., Hoppe, E., & Acton, S. T. (2013). Detection of geophysical features in InSAR point cloud data sets using spatiotemporal models. *International Journal of Remote Sensing*, *34*(22), 8215–8234. https://doi.org/10.1080/01431161.2013.833357

Waltham, Tony., Bell, F. G. (Frederic G., & Culshaw, M. G. (2005). *Sinkholes and subsidence : karst and cavernous rocks in engineering and construction*. Springer.

What is a sinkhole? | U.S. Geological Survey. (n.d.). https://www.usgs.gov/faqs/what-a-sinkhole

What is Mine Subsidence? - About Mine Subsidence - Illinois Mine Subsidence Insurance Fund. (n.d.). https://www.imsif.com/about-mine-subsidence/what-is-mine-subsidence

What is the Kyoto Protocol? | UNFCCC. (n.d.). https://unfccc.int/kyoto_protocol

Wilk, Z., Posyłek, E., Rogoż, M., Ròżkowski, A., Czaja, P., Kohutek, Z., Wichur, A., & Staszewski, B. (2003). *Hydrogeology of Polish mineral deposits and water problems of mining Volume 1 | AGH Publishing House*. https://www.wydawnictwo.agh.edu.pl/produkt/188-hydrogeologia-polskich-zloz-kopalin-i-problemy-wodne-gornictwa-tom-2

Witkowski, W. T., Guzy, A., Lucka, M., & Kusztykiewicz, K. (2023). Study on Sinkhole Formation Mechanism in Abandoned Mines. *International Geoscience and Remote Sensing Symposium (IGARSS)*, *2023-July*, 2462–2465. https://doi.org/10.1109/IGARSS52108.2023.10282648

Witkowski, W. T., Łucka, M., Guzy, A., Sudhaus, H., Barańska, A., & Hejmanowski, R. (2024). Impact of mining-induced seismicity on land subsidence occurrence. *Remote Sensing of Environment*, *301*, 113934. https://doi.org/10.1016/J.RSE.2023.113934

Ye, S., Franceschini, A., Zhang, Y., Janna, C., Gong, X., Yu, J., & Teatini, P. (2018). A Novel Approach to Model Earth Fissure Caused by Extensive Aquifer Exploitation and its Application to the Wuxi Case, China. *Water Resources Research*, *54*(3). https://doi.org/10.1002/2017WR021872

Zhou, W., & Beck, B. F. (2008). Management and mitigation of sinkholes on karst lands: An overview of practical applications. *Environmental Geology*, *55*(4). https://doi.org/10.1007/s00254-007-1035-9

Zhu, L., Franceschini, A., Gong, H., Ferronato, M., Dai, Z., Ke, Y., Pan, Y., Li, X., Wang, R., & Teatini, P. (2020). The 3-D Facies and Geomechanical Modeling of Land Subsidence in the Chaobai Plain, Beijing. *Water Resources Research*, *56*(3). https://doi.org/10.1029/2019WR027026